7-1-2016

MOLECULAR STRUCTURE AND EXCITON DYNAMICS IN ORGANIC CONJUGATED POLYMERS

Alan Thomas

Recommended Citation

Thomas, Alan. "MOLECULAR STRUCTURE AND EXCITON DYNAMICS IN ORGANIC CONJUGATED POLYMERS." (2016). https://digitalrepository.unm.edu/chem_etds/50

Alan K. Thomas
Candidate

Chemistry and Chemical Biology
Department

This dissertation is approved, and it is acceptable in quality and form for publication:

Approved by the Dissertation Committee:

Dr. John K. Grey, Chairperson

Dr. Yang Qin

Dr. Terefe Habteyes

Dr. David Dunlap

MOLECULAR STRUCTURE AND EXCITON DYNAMICS IN ORGANIC CONJUGATED POLYMERS

by

ALAN K. THOMAS

B.A., Chemistry
University of New Mexico, 2009

DISSERTATION

Submitted in Partial Fulfillment of the
Requirements for the Degree of

Doctor of Philosophy
Chemistry

The University of New Mexico
Albuquerque, New Mexico

July 14, 2016

DEDICATION

This work is dedicated to the memory of my late father, Nils Keith Thomas, for providing the example I wanted to follow. His memory provided me with the inspiration and fortitude to persevere through the trials of graduate school.

This work is also dedicated to my wife, Elaine, for her love and support, as well as my daughters, my longtime friends, companions, lab partners, students, coworkers, advisors, instructors – Thank You! All of you have contributed in so many ways to making graduate school one of the most amazing, exciting, interesting, and enlightening periods in my life.

ACKNOWLEDGMENTS

I would like to thank Dr. John Grey for allowing a knuckleheaded miscreant into his clan, putting out with my outlandish ideas (and mercilessly crushing the worthless ones), and somehow managing to guide my understanding and skills of all things spectroscopic and organic photovoltaic to the point of fruitfulness. Thanks.

I would like to thank Dr. Yang Qin for his willingness to lend an ear to some of my wilder thoughts and offer sound advice in return. He has been a wonderful asset to an often bewildered graduate student and kind supporter of my efforts at education.

I would like to thank Dr. Terefe Habteyes for his help and guidance while I worked as his teaching assistant, and for his continued support of my education.

I would like to thank Dr. Dave Dunlap for his insightful talks and inspiring conversations.

I would like to thank Yongqian Gao for his help with Labview and imaging, Jian Gao for her help in the lab and her support, Ben Stein for his assistance with low temperature experiments, and Eric Martin for his help with taming wild IMPS. I would like to thank all of my students, especially Cody Aldaz, Jordan Ulibarri Sanchez, and Hunter Brown. I would like to thank John Weeks at Wavemetrics with his help and assistance with writing code, Gary Bush for his help with students and supplies, and Dr. Richard Holder for his support of my continued education.

Molecular Structure and Exciton Dynamics in Organic Polymers

by

Alan K. Thomas

B.A., Chemistry, University of New Mexico, 2009

Ph.D., Chemistry, University of New Mexico, 2016

ABSTRACT

Intermolecular electronic interactions, dipole coupling and orbital overlap, caused by π-π stacking in organic conjugated polymers lead to unique structures and properties that can be harnessed for optoelectronic applications. These interactions define structure-function relationships in amorphous and aggregated forms of polymers in the solid state and determine their efficiencies and functionality in electronic devices, from transistors to solar cells. Organic polymer electronic device performance depends critically upon electronic coupling between monomer units –mediated by conformation and packing characteristics – that dictates electronic properties like conductivity and capacitance as well as electronic processes, such as charge carrier generation and transport. This dissertation demonstrates how electronic processes in conjugated polymers are mediated by subtle inter- and intra-chain electronic interactions imparted by the conformational degrees of freedom within their solid state structure and how this effects device performance.

To initiate this investigation into structure-function relationships, an examination of nanoparticles representing two limiting aggregation states of the conjugated polymer

poly(3-hexylthiophene) (P3HT) was conducted. These aggregates are defined by their predominate form of electronic coupling, inter- or intrachain, called H- and J-aggregates respectively. H- or J-aggregates of P3HT were embedded in an insulating matrix and time-resolved fluorescence intensity modulation spectroscopy was utilized to uncover the existence of efficient singlet-triplet quenching in J-aggregates not present in H-aggregates.

These studies were extended by examining P3HT H-and J-aggregates under applied electric fields in capacitor type devices using multiple time-resolved and steady-state spectroscopic techniques. These experiments reveal electronic couplings in J-aggregates that shift excited state population towards a majority composed of long lived, quenchable, isolated singlet excitations. The structure of J-aggregates which leads to isolated excitations, and the role which inter-chain contact sites play in triplet formation from these singlet excitations is revealed.

New structure-function relationships were uncovered in poly (3-alkyl-thienylenevinylene) (P3ATV) derivatives using resonance Raman and photocurrent spectroscopies. Time-dependent spectroscopic theory was used to interpret experimental Raman and absorption spectra that revealed the presence of structural polymorphs. These polymorphs provide an explanation of the spectroscopic evidence without presumption of a deactivating dark state in this unusually non-fluorescence material.

Photovoltaic devices constructed from blends of poly (2,5-bis(3-tetradecylthiophen-2-yl)thieno[3,2-b]thiophene) (PBTTT) and PCBM blends were examined using Raman and photocurrent imaging techniques. These techniques were used to identify different packing states in blended thin films and correlate photocurrent production with local order. Intensity modulated spectroscopic techniques (IMPS) were then used to locate regions of non-geminate charge recombination at interfaces between amorphous and crystalline regions in working devices.

Next, P3HT/PCBM OPV devices were exposed to ionizing radiation in a vacuum chamber. These devices were characterized before and after exposure, using standardized solar cell tests, Raman imaging, wide-field IMPS, and IMVS spectroscopies. An analysis of the spectroscopic data determined that the donor polymer is highly resistant to radiation damage, and that the degradation of device performance is due to an effect (cross-linking or degradation) within aggregates of the acceptor.

This dissertation concludes with an interpretation of the significance of the findings contained herein to organic electronics, followed by a brief outlook for future work in these fields. Potential theories to describe and predict molecular interactions for organic polymers in the solid state based upon their structure are discussed here. This section also covers applications to device and material design features, from molecular considerations to engineered architectures.

DECLARATION

This dissertation is composed of eight chapters. Chapter 1 gives a general introduction to this work while Chapter 2 provides a detailed explanation of the experimental setups and sample preparation. The main body of this dissertation is written in a form of five papers, which have already been published or submitted, as listed below.

Chapter 3: *ACS Nano* **2014**, *8* (10), 10559–10568.

Chapter 4: In preparation

Chapter 5: *J. Phys. Chem. C* **2015**, *119* (16), 8980–8990.

Chapter 6: *Chem. Mater.* **2014**, *26*, 4395–4404.

Chapter 7: In preparation

My mentor and research advisor, Dr. John K. Grey, supervised the composition of these publications as the corresponding author. José Garcia-Galvez and Jordan Ulibarri-Sanchez assisted with the experimental measurements in Chapter 3 while Dr. Jian Gao assisted with sample preparation. José Garcia-Galvez and Hunter Alan Brown assisted with the experimental data acquisition and processing found in Chapter 4. Dr. Yang Qin, Jianzhang Yang, and Goushun Yang synthesized the materials used in Chapter 5 where Dr. Jian Gao and Cody Aldaz assisted with sample preparation and experimental data acquisition. Dr. Hua Guo and Dr. Ryan Johnson were involved in Chapter 6 for providing molecular DFT calculations and Dr. Jian Gao supervised sample preparation and device measurements. Camron Khoustani irradiated sample devices used in Chapter 7 at the AFRL laboratories and provided in-situ measurement and exposure data.

TABLE OF CONTENTS

2.2.1 Electronic spectroscopy

LIST OF FIGURES

LIST OF TABLES

LIST OF ABBREVIATIONS

A	Electron acceptor
AFM	Atomic force microscopy
AM	Air mass
APD	Avalanche photodiode
BHJ	Bulk heterojunction
CB	Chlorobenzene
CCD	Charge coupled detector/device
CELIV	Charge extraction by linearly increasing voltage
CT	Charge Transport
CTC	Charge Transfer Complex
CS	Charge Separation
D	Electron Donor
DDC	Dipole-Dipole Coupling
DFT	Density Functional Theory
DOS	Density Of electronic States
DSC	Dye Sensitized solar cell
ED	Electron Diffraction
EMCCD	Electron Multiplying CCD
EQE	External Quantum Efficiency
eT	Electron Transfer

FF	Fill Factor
FRET	Fluorescence Resonance Energy Transfer
GIXRD	Grazing-Incidence X-Ray Diffraction
HOMO	Highest Occupied Molecular Orbital
HTL	Hole Transport Layer
IMPS	Intensity Modulated Photocurrent Spectroscopy
IMVS	Intensity Modulated Photovoltage Spectroscopy
IPCE	Incident Photon to Current Efficiency
IQE	Internal Quantum Efficiency
IRF	Instrument Response Function
I_{SC}	Short Circuit current
ITO	Indium-Tin Oxide
J	Current density
LUMO	Lowest Unoccupied Molecular Orbital
MDMO-PPV	Poly[2-methoxy-5-(3,7-dimethyloctyloxy)-1,4-phenylene-vinylene]
NA	Numerical Aperture
NF	Nanofiber
NREL	National Renewable Energy Laboratory
ns	Nanosecond
o-DCB	ortho-dichlorobenzene

OLED	Organic Light-Emitting Diode
OPV	Organic Photovoltaic
PCE	Power Conversion Efficiency
PES	Potential Energy Surface
P3HT	Poly (3-hexylthiophene)
PBTTT	Poly-(2,5-bis(3- tetradecylthiophene-2-yl) thieno[3,2-b]thiophene)
PCBM	[6, 6]-phenyl-C61-butyric acid methyl ester
PDI	Polydispersity Index
PEDOT: PSS	Poly (3, 4-ethylenedioxythiophene) poly (styrenesulfonate)
P_{in}	Input power of photons
PL	Photoluminescence
P_{max}	Maximum output power
ps	Picosecond
PS	Polystyrene
PTV	Poly(thiophene vinylene)
PVA	Polyvinyl Alcohol
r-Ra	Regiorandom
r-Re	Regioregular
RRaman	Resonant Raman Spectroscopy
SCLC	Space Charge Limited Current
SMS	Single Molecule Spectroscopy

STEM	Scanning Transmission Electron Microscopy
TCSPC	Time-Correlated Single Photon Counting
TEM	Transmission Electron Microscopy
V_{max}	Maximum output voltage
V_{OC}	Open circuit voltage
WFO	Wavefunction Overlap
XRD	X-ray diffraction

Chapter I

Introduction

Intermolecular electronic orbital interactions caused by π-π stacking in organic conjugated polymers leads to emergent electronic properties which can be harnessed for optoelectronic applications. The structure-function relationship in amorphous and aggregate forms which give rise to these interactions in organic semiconductors determines their efficiency and effectiveness in electronic devices, from transistors to solar cells. In this dissertation spectroscopic data from conjugated polymers in both solutions and solid state are used to determine the relationship between intermolecular interactions and the structures from which they arise. Knowledge of this relationship will allow the emergent optoelectronic properties of these materials to be utilized more efficiently and effectively in organic electronic devices.

1.1 Overview and Motivation

The promise of inexpensive electronics such as computers and communications devices or even photovoltaic solar cells (OPVs) has brought an intense interest to the field of organic semiconducting materials over the last several decades[1–3]. The development of efficient, low-cost organic light-emitting diodes (OLEDs) has enabled a new generation of commercially available televisions and displays[4] while improvements in organic circuitry allow for the mass production[5] of flexible electronics[6]. Their photovoltaic counterparts have experienced low device efficiencies in spite of a vast effort mounted to improve organic solar cells. Now this once promising field is being surpassed by other technologies such as perovskites or dye-sensitized solar cells (DSCs) based on most recent (2015) information from the National Renewable Energy Laboratories (NREL) operated by the United States Department of Energy.[7] Based upon the material's properties alone, organic solar cells *should* work quite well in theory but they have not lived up to this potential in practice. The main thrust of this dissertation is the examination of the reason why these materials do not live up to their expectations, and how this situation can be ameliorated.

Whether or not humanity's energy demands upon the earth have brought us to a perilous state, sustaining our current level of technological comfort requires consuming vast amounts of resources on a daily basis[8]. Humanity's ability to sustain its comfort level with the current rate of resource consumption is questionable, and without the ability to efficiently harvest the sun's energy it could very well become unsustainable in the near future[9]. Every day, the sunlight reaching earth's surface is estimated to be 1250,000 —165,000 terawatts of power[10,11]. Only a small fraction of this power would supply all of humanities energy needs[8,11]. Among the many different ways of harnessing solar power, organic photovoltaics is one of the more promising routes. OPVs can be made lightweight, flexible, and inexpensively[11–13]. The main factor preventing the widespread use of OPVs is their efficiency at converting sunlight into electrical power[13–15].

The ability of organic materials to absorb light is not the limiting factor as the absorption cross-section of many polymers is better than silicon[14]. The ability to convert an incoming photon to free charge carriers (Internal Quantum Efficiency or IQE) has been estimated to be 100% in some of these materials[16], yet the ability to successfully extract a substantial fraction of these excitons as free carriers at the electrodes is still lacking. This disjunction has been explored by many researchers and the general relationship between material morphology and device performance is now well-established[17–19]. However, the exact relationship is not easily characterized in thin films of organic materials due to their disordered nature. Instead, general material properties and bulk processes have been used to guide device design. Extended polymer conjugation aids charge transport, annealing helps establish well-interconnected regions to aid charge transport[19,20], while a bulk hetero-junction (BHJ) active layer is used to minimize exciton diffusion lengths to interfacial regions[21,22]. Using these general guidelines, almost every trial and error method has been utilized to improve BHJ OPV device performance; different donors and/or acceptor materials[12,15,19], additional hole or electron transport layers[23,24], and even different electrode materials[25–27]. While none of these changes have led to a dramatic improvement in device performance they have led to a better understanding of the internal process occurring inside photovoltaic devices.

While general material properties are sufficient to help optimize device performance, they do not lead to new insight into molecular level structure-function relationships. Electronic interactions between molecules at the single-molecule level determine the ensemble or bulk behavior of photoactive materials. A solid understanding of the influence of morphology on electronic interactions is necessary to implement rational and intelligent device design beginning at the molecular level. Without an accurate fundamental understanding of the structure-function relationship in organic electronic materials at all size scales from the molecular to the macroscopic, research cannot guide industry in the development of more efficient photovoltaics, or other electronic devices.

Overall, this dissertation aims to improve the understanding of structure-function relationships in organic electronic materials obtained from spectroscopic studies performed on isolated aggregates of organic polymers. This understanding then expands our knowledge of how morphology impacts electronic interactions and processes in bulk films and can be used to help guide future device design. As well, this dissertation contains device level studies into structure-function relationships observed in thin films containing aggregates, including correlations between aggregation and radiation induced material damage. Information gleaned from these studies can be used by industry to help improve both material and device design.

In order to build up a description of molecular level interactions in organic materials, it is necessary to begin with the unique and interesting properties of conjugated molecules. The electronic interactions between conjugated molecules called "π-stacking", and how this leads to material aggregation will be covered next. A description of how π-stacking leads to aggregates with different properties and the role of aggregates in thin films follows. Next, the electronic processes in electronic devices, both productive and loss mechanisms, are discussed. Last, there is a brief overview of the remaining chapters of the work presented here.

1.2 Conjugated Polymers and Aggregation:

1.2.1 Electron orbital interactions in organic molecules: conjugation

A neutral carbon atom has one *s* and three *p* orbitals which have different energies. As well, the valence shell of the carbon atom is only half filled, needing four electrons to complete the octet. Hybridization of a carbon atom's electronic orbitals forms four equivalent *sp* hybrid orbitals which allow the carbon atom to form four equivalent bonds (see Fig 1.1).

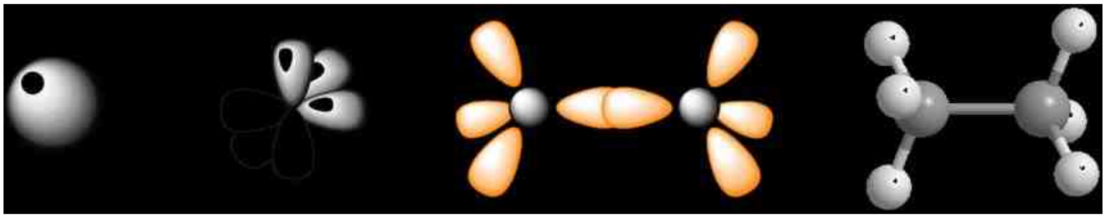

Figure 1.1 (a) Atomic s-orbital of carbon, (b) three p-orbitals of atomic carbon (c) model of ethane showing the three hybridized *sp*-orbitals of each carbon atom and the σ-bond formed by the interaction of the unhybridized s-orbitals of each carbon atom, (d) ball-and-stick model of ethane.

Hybridization of carbon atom electronic orbitals in organic molecules gives rise to unusual bonding interactions between these atoms (see Figure 1.2). When these bonds are not connected to other atoms they can form a second bond between carbon atoms. Because a single σ-bond occupies the area in between the two carbon atoms, the electrons in the second or third bond must adopt an out-of-plane interaction in between them, known as a π-bond. These bonds are made from *unhybridized* atomic *p*-orbitals, so the formation of a π-bond reduces the overall hybridization count of each carbon atom: the two ethane carbons are sp_3 hybridized but the two carbon atoms in ethylene are only sp_2 hybridized. The carbon atoms of acetylene, (not pictured) which has a triple bond between carbon atoms are *sp* hybridized. Because carbon atoms in conjugated polymers and aromatic molecules have more than one carbon-carbon bond, most carbon atoms in these molecules are *sp* hybridized.

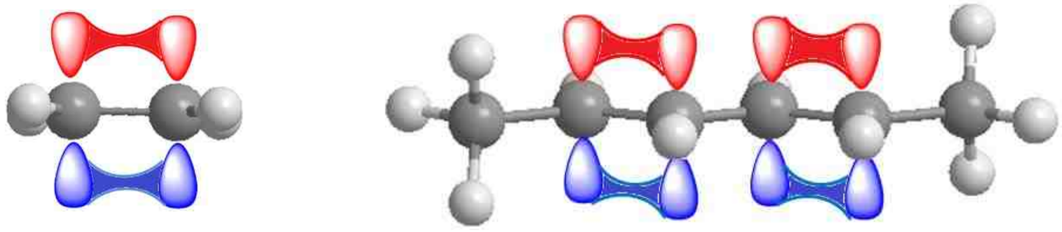

Figure 1.2 Model of ethene showing the π- bonds formed by the interaction of two unhybridized p-orbitals (left) and a model of 2,4 hexadiene showing the formation of two π-bonds (right).

The creation of double and triple bonds between carbon atoms adds an unusual dimension to their structural and electronic configurations, which in turns impacts their reactivity and molecular interactions. Alternating single and double bonds along the carbon backbone of a molecule, called conjugation, leads to an interesting condition called resonance (see Figure 1.3). The two configurations of the 1,3 pentadiene molecule shown below are equivalent and indistinguishable.

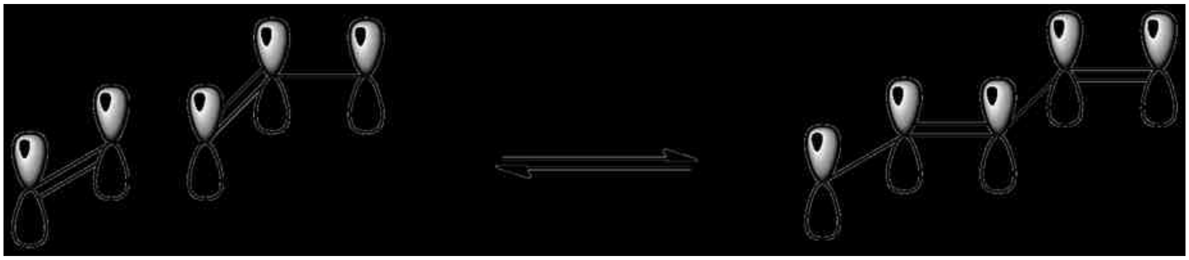

Figure 1.3 2,4-pentadiene model showing resonance structures. Actual bonding structure of molecule is intermediate between the resonance structures shown.

Because of the different bond energies single and double bonds between carbon atoms possess, these bonds should, and do, have different measured lengths. However, when conjugation occurs in these molecules, the difference in length between single and double bonds becomes smaller as conjugation length increases, until an ideal situation is achieved where there is no difference at all. Benzene, a cyclic aromatic compound which is fully conjugated has been shown by x-ray crystallography to have 6 identical bond lengths instead of alternating single and double bonds[28].

One of the most important physical properties of conjugated molecules is their ability to absorb light in the visible spectrum. The importance of this fact cannot be overstated; Rhodopsin is a biological molecule with an extended system of conjugation and is the component responsible for light-detecting in the cells of the human eye via its absorption. Relating conjugation length in a molecule to its light absorbing ability can be accomplished using two different applications of quantum mechanics, the “particle-in-a-box” approximation and Hückel molecular orbital theory.

The first theory models the particle wave-functions using a particle whose motion is restricted to a one-dimensional “box” whose walls represent infinite potential energy barriers. This can be applied to an electron in a conjugated molecule, both small molecules and polymers, where the length of the box is equal to the length of conjugation in the molecule. By restricting the motion of the electron to this “box”, it is possible to determine the allowed energy states by solving the time-independent Schrödinger equation. The different energies of the vibrational and electronic levels of the molecule are then calculated using this approximation as well as the energy of electronic or vibrational transitions. Theoretical electronic and vibrational spectra can be derived from these calculations. While this theory works well for small molecules with limited conjugation lengths, one of the major drawbacks to the particle-in-a-box approximation is that it predicts electronic band-gaps become vanishingly small as conjugation length increases – something not observed experimentally. However, it is equally possible that this is a reflection of the actual molecular structure and not a fault of the theory.

While it is possible to manufacture polymers with very long conjugation lengths, spectroscopy of these polymers shows that there is a saturation point at which the onset of absorption, a reflection of the electronic bandgap, no longer shows a decrease in energy. Based upon studies where polymer length was incrementally increased one monomer unit at a time and absorption spectra taken for all lengths of the polymer, it has been shown that the bandgap reaches a minimum value somewhere between 10 – 15 monomer units and that increasing polymer length does not result in any further decrease in the bandgap energy[29]. It has been theorized that this represents a functional limit to conjugation length, and that structural distortions of the conjugated polymer limit effective conjugation length. Based on these studies, it has been surmised that while a long polymer chain may have extensive conjugation, absorption and emission occur from distinct and limited regions of a polymer, called chromophores. A single polymer strand may then contain many such units, each of which is capable of acting like a distinct absorber and emitter. As well, these chromophores are capable of interacting with one another via energy or electron transfer mechanisms.

Hückel molecular orbital theory is a partial quantum mechanical treatment of electronic interactions between atoms in conjugated molecules. The electrons in the σ, or backbone bonds, are neglected and only electrons occupying π-bonds are used in these calculations. Matrices are constructed that model the site (atom) energies and their resonance (interaction) energies for electrons in these bonds using the time-independent Schrodinger equation. Solutions to these matrices yield the interaction energies for conjugated and aromatic molecules. It was Hückel theory which first accurately described the additional lowering of molecular orbital energy for aromatic molecules, a fact that the particle-in-a-box" theory does not account for. The lowering of orbital energy for aromatic (cyclic conjugation) molecules occurs because of an additional resonance term in the matrix which represents the interaction of the ring bonds.

1.2.2 Π-π stacking in organic molecules:

When molecules with conjugation are in close physical proximity to one another, the molecular orbitals on these molecules may begin to overlap with each other (see Figure 1.4). Wavefunction overlap (WFO) between molecules can be calculated. Molecules with overlapping wave functions can share electrons. This may apply to both the ground and excited states, or only one, depending upon the type of orbitals involved. In the case of conjugated molecules, occupied excited state electronic orbitals overlap with unoccupied excited state orbitals on neighboring molecules, causing a sharing of electron density between the molecules.

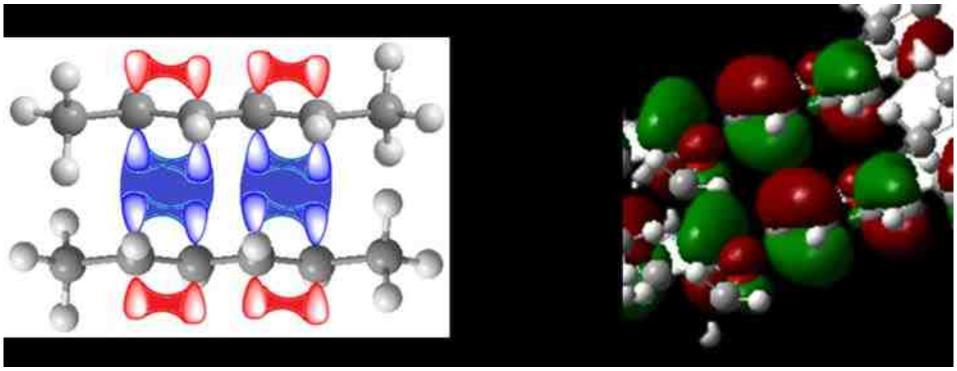

Figure 1.4 Models showing π-π intermolecular interactions. Two molecules of 2,4-hexadiene (left) showing the interaction between molecular orbitals on two separate molecules and calculated orbitals of two polymer molecules (right) showing proximity of orbitals on two molecules with each other.

This is not the only type of electronic interaction that can exist between molecules in the solid state. Dipole-dipole coupling (DDC), an intermolecular Coulombic interaction between the donor emission dipole moment and the acceptor absorption dipole moment, can allow for the radiationless exchange of energy between molecules. This type of coupling between two dipoles can result in energy transfer up to 10 nm in organic materials[30]. This can be significant in ordered pi-stacks of conjugated polymers where interstem spacing is on the order of 0.38 nm. This type of energy transfer is called Förster Resonant Energy Transfer (FRET) after the author in Ref. 29.

1.2.3 Exciton coupling in aggregates: H- and J-type interactions

"Exciton" is the name given to an electron-hole pair that is bound together via Coulombic or electrostatic force. In many inorganic materials which absorb light, the binding energy between the photoexcited electron and hole is so small that the electron is essentially a free charge carrier from the moment it becomes excited. However, in organic materials the exciton binding energy can be much larger, between 0.3 and 1 eV[31–33]. This creates a situation where, in order to separate the electron from its hole, some energetic offset must be provided which makes this process favorable. Thus, the term exciton is generally (but not always) applied to organic systems where the photoexcited charge pair is bound by a sufficient amount of energy that scission is unfavorable without the influence of an external factor such as a charge transfer state induced by proximity to an electron accepting molecule. While it is possible to construct OPVs from just polymers alone[34], their efficiencies are low due to this binding energy. It was the blending of organic polymers donors with small molecule acceptors which led to the development of the first solar cells, first in bi-layer devices and then later in bulk hetero-junction devices[35,36].

Concentrated solutions of small, conjugated, organic dye molecules can exhibit signs of intermolecular excitonic interactions. Although this behavior had not been seen previously, in 1936, Jelley conducted spectroscopic studies of small organic dye molecules and was the first to provide spectroscopic evidence for these interactions.[37] He also noted that the dye could self-assemble into phases with different spectroscopic properties, depending on the exact experimental conditions[38]. Because the two distinct types of aggregates displayed a hypsochromic or bathochromic spectral shift in absorption spectra, the names “H” for hypsochromic and “J” for Jelley were applied respectively to the aggregates depending on their spectral shift. This nomenclature was not adopted immediately because of a conflict with publications by another researcher, but took hold over time. The first actual mention of “H and J-aggregates” in literature appears in an article from 1950 regarding the aggregation states of silver halide photographic emulsions[39].

In 1938, Frank and Teller were the first to apply the newly put forth exciton theory to aggregates of these dye molecules[40], but it would wait until 1963 for Kasha to propose a more complete version[41]. The basic tenets of Kasha’s molecular exciton theory are shown in Figure 1.5. This theory describes the sharing of electrons between small molecules are based on dipole – dipole coupling (DDC) between molecules[41]. While this theory does a wonderful job of describing the coupling in between dimers of dye molecules, and it accurately predicts the spectra for H and J-aggregates of small molecules, it is less proficient at capturing the behavior of covalently linked polymers.

Figure 1.5 Model of dipole coupling in dimers of small molecules. Light blue arrows show orientation of transition dipoles. Solid arrows show allowed transitions, dashed arrows show forbidden transitions. Figure adapted from ref. 42.

In the late 1990's, Spano and co-workers set about applying the small molecule H and J-aggregate model to polymer systems in theoretical calculations.[42,43] The first iterations of this model used dipole-dipole coupling, but attempted to refine the exciton model by accounting for the role of molecular vibrations as well. Later work by Spano and others demonstrated that for highly planar, well conjugated polymers DDC becomes vanishingly small[44–46]. Upon the realization that DDC is minimal in systems of extended conjugation, this model was then expanded to include WFO. Quantum mechanical calculations were executed which showed that the H and J-like behavior could be reproduced using this type of coupling alone[47]. This was extended to combining the knowledge of both types of coupling in polymer aggregates, providing a better understanding of the eventual outcome of photoexcitations within these aggregates.

In the work presented in this dissertation, intermolecular exciton interaction models are used to interpret experimental data obtained from two limiting structural forms of nanoaggregates of the P3HT polymer. They are also utilized to aid in understanding the role of aggregates in thin films. Because the help establish a direct like between spectroscopic data and molecular structure theory, they can be used to help understand the nature of both the electronic interactions and electronic processes present in polymer aggregates.

1.3 Thin Films and Aggregates

1.3.1 Polymers and blended thin films

Solid state structure in conjugated polymers is directly related to how they entered into the solid state. The first organic semiconducting polymers were insoluble and had to be carefully evaporated onto substrates in order to make electronic devices[48]. This intractability led to the addition of alkyl side chains to conjugated polymers thus making them solution processable in a variety of organic solvents. Solution processing opens up the possibility of screen printing, ink-jet printing, and spin-coating[49] as practical and industrially relevant techniques; however, none of these techniques currently allow for conformational control of the polymer during drying. While conjugated polymers without side chains are highly crystalline in the solid state, polymers with them are not. Polymers in solution have access to a much larger conformational space and are more disordered. When using solution deposition techniques, such as spin-coating, the resulting solid state of the polymer is highly disordered and resembles a tangled weave of interpenetrating polymer chains. When conjugated polymers are blended together with small molecule acceptors in well-mixed solutions and then deposited using solution spin-coating techniques, the resulting as-cast films are also well mixed and amorphous.

Electronic devices made from films deposited onto substrates using solvent based techniques without further processing have a highly amorphous structure with good mixing of the donor and acceptor molecules (see Fig 1.6a). OPV devices made in this manner have low power conversion efficiencies (PCEs), ~ 1 %. It was theorized that a recovery or even partial recovery of the crystalline state of the polymer could lead to more enhanced charge movement in these devices, so a range of annealing techniques were then utilized to alter the solid state structure of films made from conjugated polymers.

1.3.2 Aggregate formation in thin films.

Annealing experiments demonstrated that structural reorganization of the polymer donor and small molecule acceptors occurred under proper conditions, and that aggregated crystalline regions developed within D/A thin films (see Fig 1.6b). Simultaneously, there was a dramatic increase in the power conversion efficiency of these solar cells when these aggregates formed[19]. Photocurrent imaging of annealed thin films of P3HT/PCBM revealed that the majority of the photocurrent in these films was being created on or near these aggregates, and that the bulk, amorphous portions of the films contributed little to device performance.

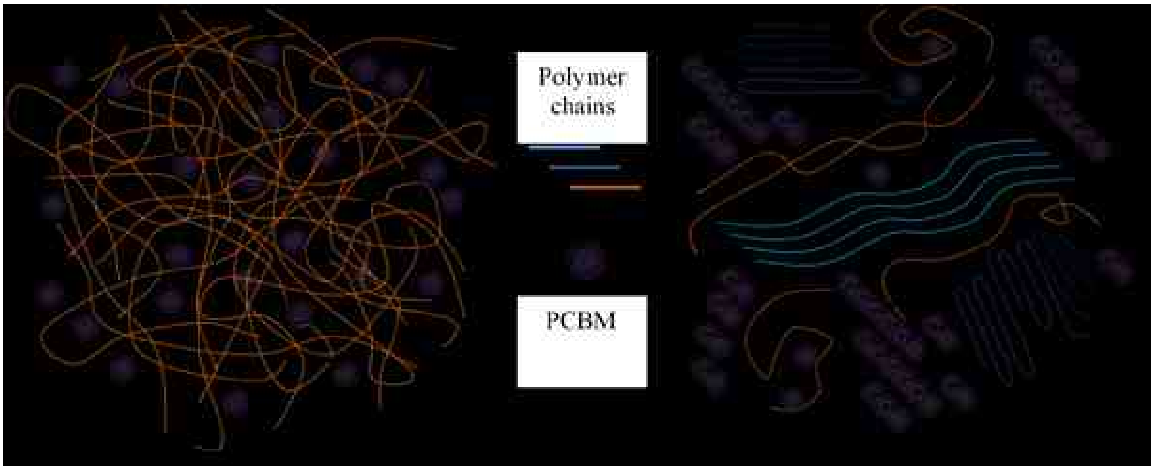

Figure 1.6 (a) Amorphous film structure and (b) annealed film structure.

This, in turn, has led to many studies concerning the exact nature of the composition and electronic interactions within aggregates of pristine and blended polymers and the exact nature of their structure-function relationship. While the deconvolution of individual contributions is difficult to obtain from disordered thin films, aggregates observed in isolation can yield valuable information about their contributions to thin film performance. The purpose of creating isolated aggregates of the pristine material is to determine the role of electronic interactions within them and the formation of electronic states: singlet and triplet excited states as well as uncorrelated charges.

1.3.3 Nanofiber aggregates

Polymer aggregates can self-assemble in solvent solutions under a variety of conditions, depending on the nature of the solvent-solute interactions and the solute-solute interactions. In solutions of marginal solvent, under heating and subsequent recrystallization, P3HT has been shown to form two distinct types of structural aggregates which have very different spectroscopic and electronic conformations[50]. Spectroscopic signatures of both types of electronic couplings, H- and J-type, are seen in both types of these structurally different aggregates, but in varying degrees[50]. Assignment of the names given to these two types of aggregates reflects the predominant, but not exclusive, form of electronic coupling found in their spectroscopic footprint.

H-aggregate P3HT particles are made using the whisker method, using anisole as the solvent and the cooling process is rapid and uncontrolled. Resulting nanoparticles truly resemble “fibers” of cotton or linen. They have widths which vary between 10 – 15 nm[51,52], heights of 2 – 6 nm[53,54] and can be 10s of micrometers long[55].

J-aggregate P3HT “nanofibers’ have widths of 20 – 40 nm[51,52,56] (estimated from TEM images), heights of 2 – 6 nm[53,54] (from AFM data), and are much shorter than their counterparts, usually less than a single micrometer long[51,57]. J-aggregate nanofibers appear blocky in TEM images[52] and less fiber-like than H-aggregates.

1.4 Electronic devices and loss mechanisms

In OLEDs, uncorrelated charges are injected into a device by an applied external electrical potential. These charges must localize and correlate with one another before emission can occur. Spin statistics dictate that the probability of an electron correlating with a hole in a singlet state vs the three degenerate triplet states (see Fig.1.7) is roughly 25%. Therefore, triplet states were recognized as a source of inefficiency in in OLEDs from the very start.

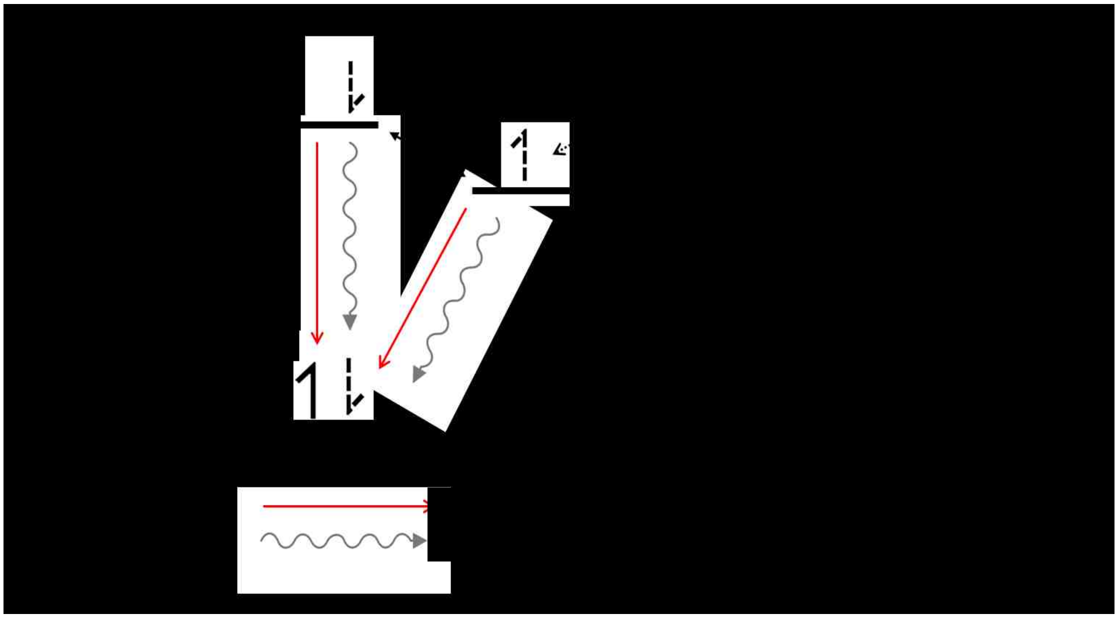

Figure 1.7 Simplified model of injected charges recombining in an OLED. Electrons and holes have a 1:3 probability of correlating as singlets or triplets. Combinations of spin multiplicity are shown in the box on the right. In conventional OLEDs only the recombination of singlets will emit light.

While various methods have been employed to maximize singlet states, or pump triplets to the singlet state through annihilation[58], or thermal activation[59], the most successful method to date populates the triplet state efficiently using energy transfer mechanisms and phosphorescence becomes the source of the emission[60]. While this scheme can potentially allow for a 100% efficiency of injected charges to emitted light, these materials often experience bottlenecks at high injection currents due to the longer lifetime of the triplet state.[60]. While fluorescent polymers led a brief surge in interest for applications in OLEDs[61], and they are still being used for research today[62], industry began with[63] and still utilizes primarily small molecules for OLEDs.[64]

In stark contrast to OLEDs, triplets still represent a loss mechanism in OPVs[65–67]. The absorption of a photon to create an excited state in matter has specific selection rules that are covered more thoroughly in the section on spectroscopy. For now, it will suffice to say that direct population of the triplet state from the ground state is a “spin-forbidden” transition, and that this transition will only manifest itself weakly in an absorption spectrum of the material if at all. For molecules with C_{2h} symmetry, (common amongst organic polymers), the only fully allowed (spin and orbital symmetry) transition is from the totally symmetric ground state ^1A_g to the anti-symmetric excited state ^1B_u. The ^3B_u triplet state is directly inaccessible from the ground state.

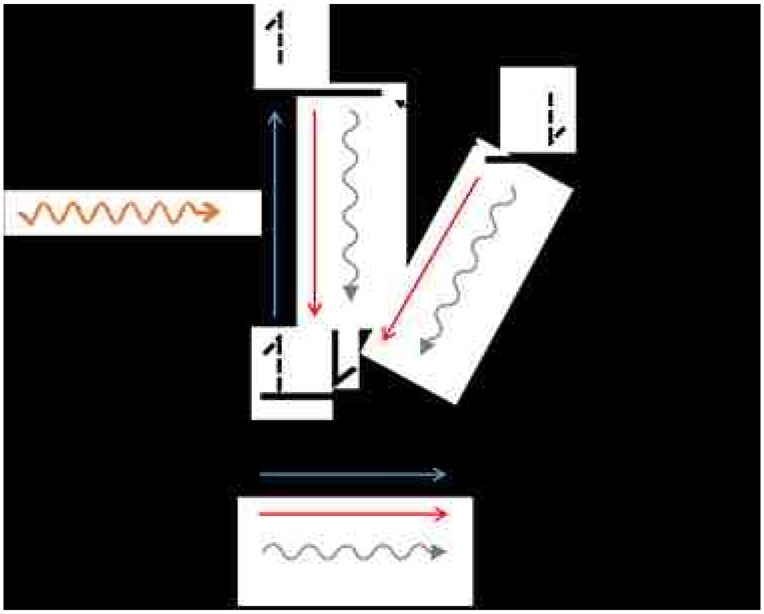

Figure 1.8 Simplified model of energy levels and electronic process found in representative conjugated polymers.

Because the decay of an triplet excited state to the ground state is also spin-forbidden, these non-radiative states[68] are long-lived (up to minutes). Essentially, triplet states are chromophore deactivating, heat producing energy loss pathways in OPV devices. Because of the complexity of the electronic process which *may* occur in a Donor/Acceptor (D/A) bulk hetero-junction (BHJ) style thin film OPV solar cell (see Fig.1.9), pin-pointing the structures which lead electronic excitations to the triplet state are difficult.

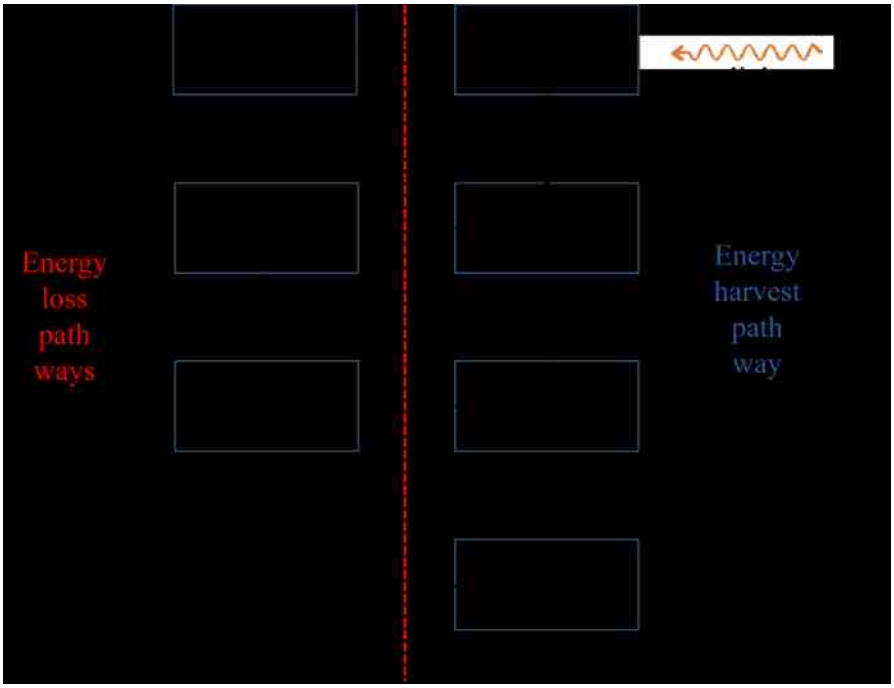

Figure 1.9 Diagram of internal electronic processes in an OPV. Recombination or energy loss processes are on the left and photocurrent producing processes are on the right.

While some studies have shown that there exists a strong possibility for electron back-transfer from acceptor to donor following initial charge separation[20,69] which can lead to triplet formation, other researchers have noted that thin film OLEDs of pristine polymer also form triplet states[70]. Whether it is in the pristine material or in blended composites, the formation of triplet states has a large impact on OPV device performance. Knowing exactly what type of structure, within a single polymer chain, an aggregate of chains, or a mixed aggregate of polymer chains and acceptor molecules, leads to the formation of triplet excited states is crucial to improving device performance.

1.5 OPV Device structure and processes

1.5.1 Device structure

The basic structural components of a research OPV solar cell are shown in Figure 1.10. For the overwhelming majority of the experimental samples used in this thesis, the relative thicknesses of the different layers for OPVs and other devices remain fairly constant and exceptions will be noted when they occur. Briefly, a transparent conductive surface composed of indium-tin oxide (ITO) of variable stoichiometry is deposited onto the transparent glass substrate to act as the hole collection electrode. A hole-transport layer (HTL) of PEDOT-PSS is then spin coated on top of the conductive layer and thermally annealed to remove residual moisture. The active layer of the device (P3HT/PCBM is used as an example) is then spin coated on top of this layer using an orthogonal solvent. While many research groups add an additional electron-transport layer on top of the active layer in devices, none of the devices analyzed here made use of such a layer. Instead, the aluminum is evaporated directly on top of the active layer to create the top electrode. This is done at slow rates and low temperatures to help prevent damaging the active layer.

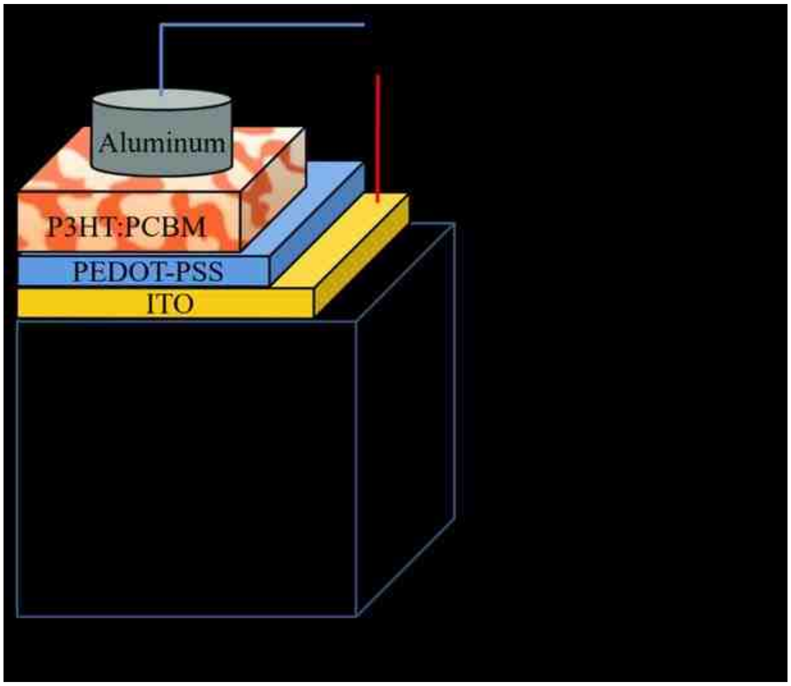

Figure 1.10 Simplified cut-away view of an OPV showing representative layer thicknesses and composition.

1.5.2 Electronic processes

The electronic processes which occur within an OPV are outlined from point where an incident photon enters the device all the way to the extraction of an excited electron at one of the device electrodes are shown in Figure 1.11. The absorbed incident photon creates an exciton (a), a bound electron-hole pair with the associated structural distortions of the molecule which are associated with it. These structural distortions follow the exciton as it migrates from one chromophore to another (b) until it reaches a D/A interface (c). Upon reaching the interface, the electron may transfer over to the acceptor molecule which can either create a bound charge-transfer (CT) state (d) , or undergo complete scission to create free carriers (e). The free carriers must still migrate to an electrode (g) while avoiding low-energy "traps" (f) in the potential energy landscape.

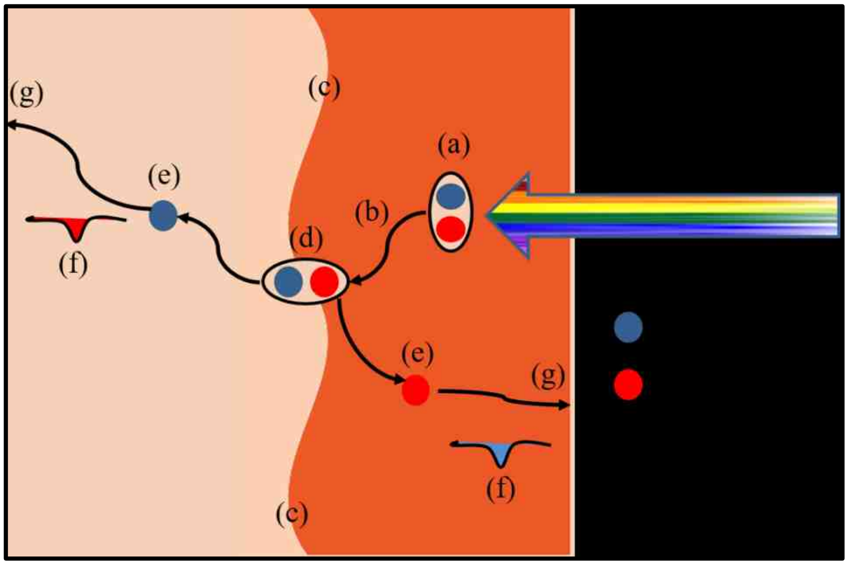

Figure 1.11 Diagram of exciton and free-carrier migration within the active layer of an OPV.

The D/A interface is one of the key factors to the success of OPVs as a whole. Because the primary photoexcitations, excitons, in organic molecules tend to distort the molecular framework they reside on, this creates the binding force between the electron and hole which was discussed earlier. In order to overcome this binding force, there exist an engineered energetic offset between the occupied excited state of the donor and the unoccupied excited state of the acceptor (see Fig 1.12). This offset provides a driving force for scission of the exciton[71,72]. However, if the offset is insufficient to overcome the exciton binding energy the charges can become trapped at the interface, forming an intermolecular CT state.

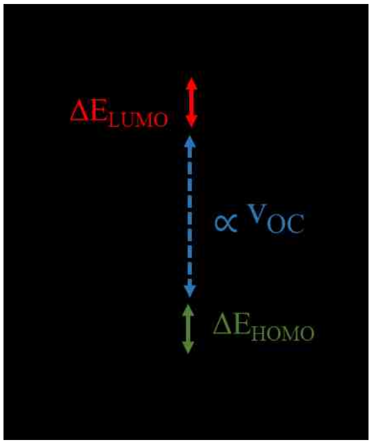

Figure 1.12 Diagram of energy level offsets between donor and acceptors which provides a driving force for exciton scission/ charge separation.

This thesis presents the techniques and methods used to manufacture various aggregate states of the materials in isolation or in thin films, as well as their spectroscopic interrogation of their exciton dynamics. It also includes experimental data from functioning solar cells examined for an in situ look at correlations between aggregation states and device performance. In addition, there is an experimental look at the effects of ionizing radiation of the performance of solar cells and aggregates within them.

Chapter 2 will be an overview of the materials, samples, and equipment used to conduct all of the experiments contained in this document. Chapter 3 will begin the examination of H/J mixed aggregates using time-resolved single particle (fiber) intensity modulated fluorescence spectroscopy to reveal the presence of substantial singlet-triplet quenching in J-aggregate fibers. Chapter 4 continues this exploration by using electric-field dependent time-correlated single photon counting (single fiber fluorescence decays) on both H and J-aggregates to determine the location of the initial triplet formation at interchain contact sites as well as the electronic factors which lead to triplet formation at these sites. Chapter 5 carries the aggregation theme to the poly-thienophenevinylene (PTV) polymer in solid state and in functioning solar cells to correlate photocurrent production to aggregation state using photocurrent and Raman imaging spectroscopies. Chapter 6 extends the aggregation theory to the well-intercalated PBTTT: PCBM donor-acceptor system in devices using the same techniques as the PTV work. Chapter 7 looks at the effects of ionizing radiation on the structure and function of P3HT/ PCBM solar cells. We find that although device performance is degraded by exposure to radiation, Raman imaging and analysis show no reduction in the number of carbon-carbon double bonds or the aggregation state in the donor polymer. Chapter 8 looks at the overall conclusion which can be drawn from the body of work presented here.

Chapter II

Experimental

2.1 Materials

This section begins with an overview of the structure and composition of the materials used throughout the experiments contained in this dissertation. These materials fall into four categories: electron donating materials (n-type materials), electron accepting materials (p-type materials), inert or insulating materials (non-conductive), and substrates. While the polymer semiconductors used in these experiments were not doped, and had no intrinsic excess of electrons or holes, donating materials are considered n-type and acceptor materials are considered p-type semiconductors for purposes of comparison with inorganic doped semiconductors. A brief description of each material follows in reverse order that they were previously listed. The second part of this section describes the types of spectroscopy used in the experiments, the spectroscopic equipment, and configuration of the experimental set-ups used to conduct the various experiments contain herein.

2.1.1 Substrates

For the purposes of high-resolution confocal microscopy, all material samples and photovoltaic devices were manufactured using 1” square glass covers slips (VWR) with a nominal thickness of 160 – 190 micrometers. These are much thinner than the substrates used by most other researchers in the photovoltaics field, but were necessary for work with a high numerical aperture objective because of the short working distance of this type of microscope objective.

Substrates fell into one of three categories: plain glass, conductive substrates coated with ITO, and capacitive substrates which have a layer of conductive material (ITO) capped with an insulating layer of SiO_2 (see Figure 2.1). ITO layers have a nominal thickness of 100 nm, while subsequent layers of glass were either 30 or 50 nm depending on the specific batch that was ordered.

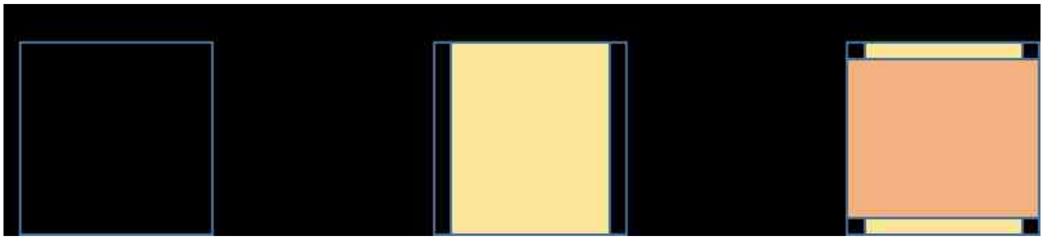

Figure 2.1 Plain glass substrate (left) with 1 inch dimensions (shown by arrow), ITO coated substrate (center) with ITO layer shown in yellow, ITO and glass substrate (right) with insulating glass overlayer shown in rose.

2.1.2 Insulating materials

The insulating material used to isolate individual small molecules and nanofibers from each other for single molecule or single aggregate spectroscopy was polystyrene (GPC analytical standard, 70 KDa, Sigma –Aldrich) (see Fig. 2.3). The only other insulator used was glass (amorphous SiO_2), deposited as a thin layer over ITO to help prevent charge injection from the hole collecting electrode.

2.1.3 Electron donating materials

Three different types of material were used in these experiments as the electron donor: poly(3-hexylthiophene) (P3HT) (Sigma-Aldrich, 99.9% regio-regular, 54 – 75 KDa M_{n},), poly(3-octyl-thienylenevinylene) (PTV) (M_n = 32.8 kDa, M_w = 65.6 kDa, PDI = 1.9) which was custom made by collaborators, and Poly[2,5-bis(3-tetradecylthiophen-2-yl)thieno[3,2-b]thiophene (PBTTT) (Sigma-Aldrich, M_W=49 kDa, PDI = 2.3). As a side note, the PBTTT polymer is no longer available for sale in the continental U.S. It can still be obtained from overseas vendors however. The chemical structure and composition of all of these polymers is shown in Figure 2.1.

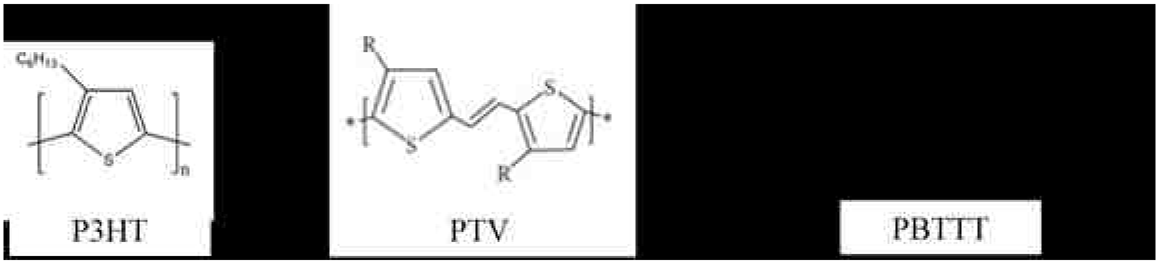

Figure 2.2 Structural drawings of P3HT (left), PTV (center), and PBTTT (right)

2.1.4 Electron accepting material:

Phenyl-C_{61}-butyric acid methyl ester (PCBM) (>99.5% pure, Sigma-Aldrich) was used exclusively as the electron acceptor in all photovoltaic devices (see Figure 2.2 for molecule structure and composition). While there are a number of compositional analogs of PCBM commercially available, and a number of alternate acceptor molecules which are also available, PCBM was chosen as the acceptor of choice because it has been the most widely used acceptor in OPV literature. This allows for the direct comparison of performance characteristics between devices constructed by other researchers with those presented here.

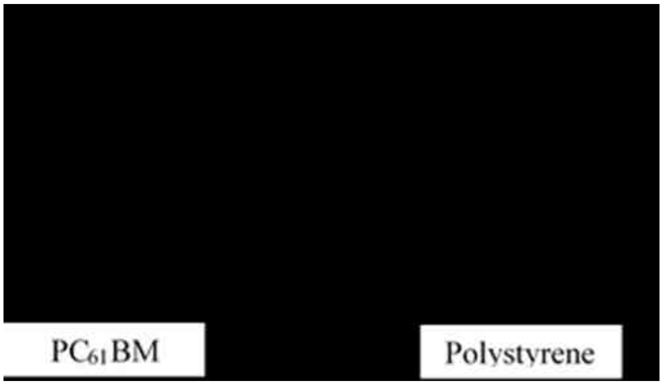

Figure 2.3 Structural drawings of PCBM (left) and polystyrene (right)

2.1.5 Types of samples

There were three types of samples used in all of these experiments: Samples prepared on plain glass, working solar cells, and capacitor style devices with an insulating layer containing dispersed material in between conducting electrodes. The architecture of working solar cells as well as approximate layer thicknesses was given in the Introduction. Plain glass samples lack the conductive ITO layer and were made with and without an aluminum overcoating. Dummy devices (capacitors) have the same architecture as working solar cells but the active layer is replaced with an inactive (insulating) layer containing a very low concentration dispersion of the material of interest.

2.2 Spectroscopy, Equipment and Experimental Set-ups

2.2.1 Electronic spectroscopy:

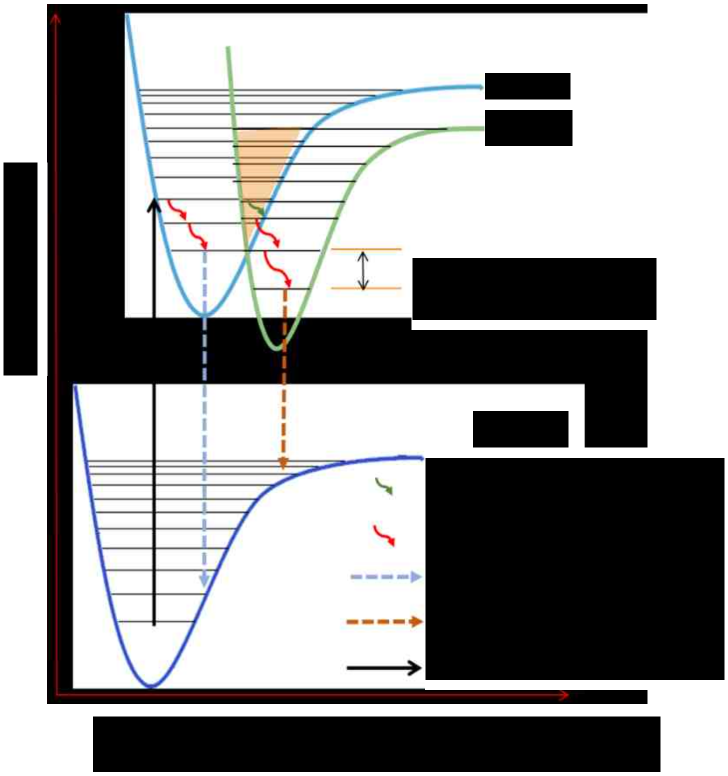

Figure 2.4 Model of electron donor potential energy surfaces and internal electronic processes.

Electronic spectroscopies involve the transition of an electron from one atomic or molecular orbital to another electronic orbital (see Figure 2.4). Absorption spectroscopy involves atomic or molecular absorption of a photon which promotes an electron from the ground state to an excited state, or from an excited state to a higher energy excited state. Emission spectroscopy involves the radiative decay of an electron in an excited atomic or molecular state to a lower energy state or the ground state. This radiative decay can be fluorescence, decay from the singlet excited state to the singlet ground state, or phosphorescence, decay from a triplet excited state to a singlet ground state. Because the decay from a triplet excited state to a singlet ground state transition is spin-forbidden, phosphorescence generally occurs on much longer times scales than fluorescence.

2.2.1.1 Absorption

Absorption of solutions and thin films was conducted on either a Shimadzu UV 2540, 2550 or a Hitachi UV 4100 instrument. Standard path length (1 cm) quartz cuvettes or quartz micro cuvettes with a path length of 0.1 mm were used for all measurements. Thin film measurements were taken with glass substrates in single beam mode. Low temperature experiments were performed using a liquid nitrogen cryostat inserted into the Hitachi instrument and measurements were also taken in single beam mode.

2.2.1.2 Emission

All photoluminescence (PL) measurements were taken using a Varian Cary Eclipse spectrofluorimeter or with our custom microscopy equipment using an Andor Newton Shamrock 303i spectrograph with an electron multiplying charge capture device (EMCCD) detector. Bulk, thin film, and solution spectra were collected using the Eclipse, while single molecule/aggregate PL spectra were taken using the confocal microscopy set-up with the Andor spectrograph and detector. Photoluminescence imaging data was collected using both slow (Perkins-Elmer SPCM-AQR-15) and fast (ID QuantiqueID100) avalanche photodiode modules (APDs).

2.2.1.2.1 Intensity Modulation Experiments

Output laser light (568 nm) from a krypton gas laser (Melles-Griot) was routed through an acoustical-optical modulator (AOM) (402-AF1, IntraAction Corp.) driven by the output of a function generator (Fluke 271 10 MHz). Fluorescence was collected with the microscope objective (backscatter configuration) and routed to a slow APD. The APD output was connected to a multichannel analyzer (MCA) (FastComtec MCA-3) board installed in a desktop computer (see Figure 2.5). Synchronization of the MCA collection with the excitation cycle was performed by slaving the function generator supplying signal to the AOM to the generator providing collection timing signals to the MCA board. Electric field bias was applied using a function generator connected to a high voltage power supply (Trek model PZD240).

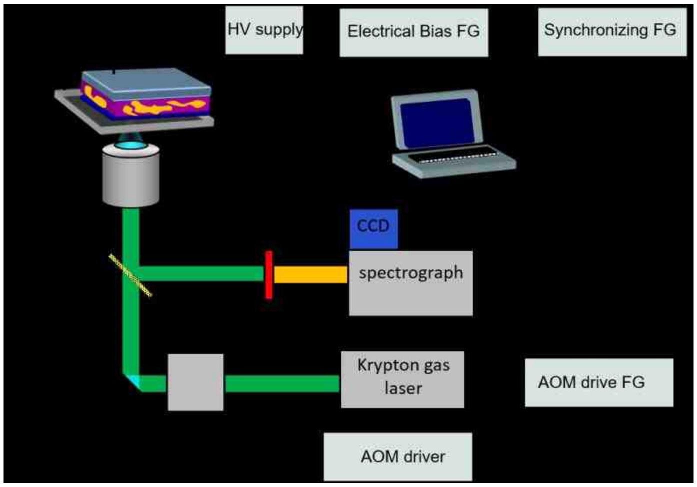

Figure 2.5 Experimental set up for excitation intensity modulation experiments.

2.2.1.2.2 Time correlated fluorescence spectroscopy

Time correlated single-photon counting (TCSPC) is a very fast form of emission spectroscopy. Using 100 femtosecond optical pump pulses to excite emissive molecules, it is possible to analyze their emission on nanosecond time scales. Titanium:sapphire oscillators which are seeded using CW lasers generate temporally narrow pulses of light (10 – 100 fs) at specific, tunable wavelengths and high repetition rates are used to optically excite a sample. The photoluminescence emission of the sample is detected using avalanche photodiodes (APDs) with very fast response speeds in between excitation pulses (see Fig 2.6). After the sample has been excited, the detector waits for a photon to arrive. When the detector detects a photon it sends a signal to a computerized counting board which registers the count and then waits for a synchronizing pulse to arrive from the laser. An internal time-to-amplitude converter then converts the time between detection and synchronization to an amplitude and stores this data in a bin.

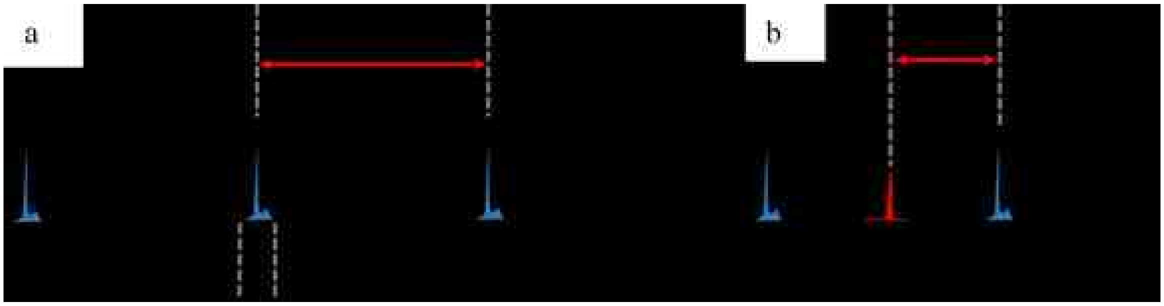

Figure 2.6 (a) Diagram showing the excitation pulses used in TCSPC spectroscopy (blue filled curves), excitation pulses width (black arrows), and spacing between excitation pulses (red arrow). (b) Single photon detection (red filled curve) and time between photon detection and the next excitation pulse (red arrow).

This type of experiment requires careful timing alignment between the detector and exciting laser; that is, data from the detector must arrive at the counting board in the time interval between pulses or it will not be properly binned. Finally, the acquired and binned data is displayed as a histogram of the entire experimental time, generating a PL decay curve (see Fig 2.7).

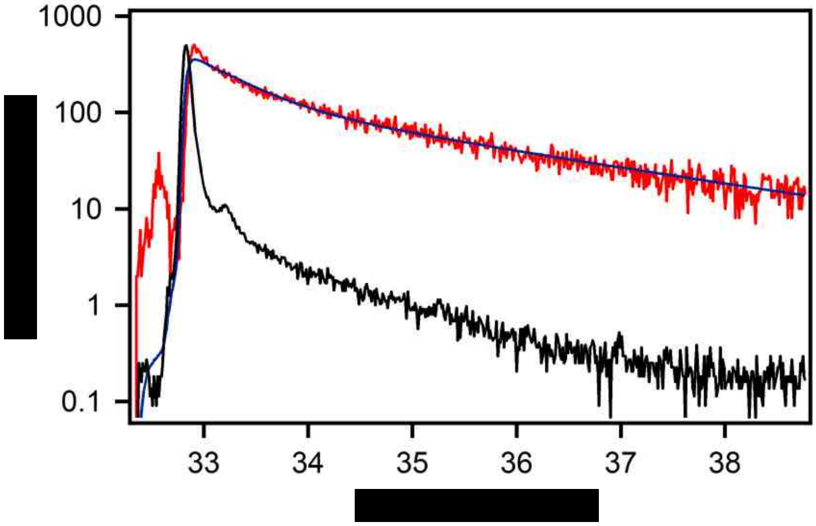

Figure 2.7 TCSPC experimental data showing IRF (black trace), acquired data (red trace) and fit to experimental data (blue trace).

This decay curve represents the time that it takes for radiative excited state deactivation to occur in the sample. Raw decay data is convoluted with the instrument response. The instrument response function (IRF) is the total effect of every optical component on the excitation pulse convoluted with the detector response. Instrument response is measured separately on a non-fluorescent region of the sample, but in the exact same configuration as is used to collect data. To determine the number and lifetime of emissive states represented by the sample under analysis, the instrument response function is convoluted with a fit equation and matched to the raw decay data using a least-squares-fitting routine. However, if the number of emissive states is not known *a priori*, then different fitting routines must be tried to determine which actually fits the data best.

The high repetition rate of the laser pulse train (76 MHz) allows for multiple excitation and detection cycles per second, but the overall detection rate is determined by the “dead time” from the counting board used to collect the data from the APD. This dead time represents the time it takes internal buffers in the counting board to be cleared and reset to collect data. While this limits the total number of analysis windows per second, the high laser pulse repetition rate still allows for the possibility of millions of collection cycles per second.

Fast fluorescence decay experiments were performed using a Ti:sapphire oscillator (Coherent Mira 900) pumped with a 10W 532 nm diode laser (Coherent Verdi G). 800 nm output from the oscillator was directed to a white light continuum generator (Thorlabs Femtowhite). Excitation wavelengths were selected using multiple bandpass filters in series to reject other wavelengths and residual pump output. Data was collected using a fast APD (ID-Quantique ID100). Signals from both the excitation source and the APD were collected and synchronized using a Becker & Hinkle single photon counting board installed in a desktop computer (see Figure 2.8). Fluorescence decay data was deconvoluted and fit using commercial software.

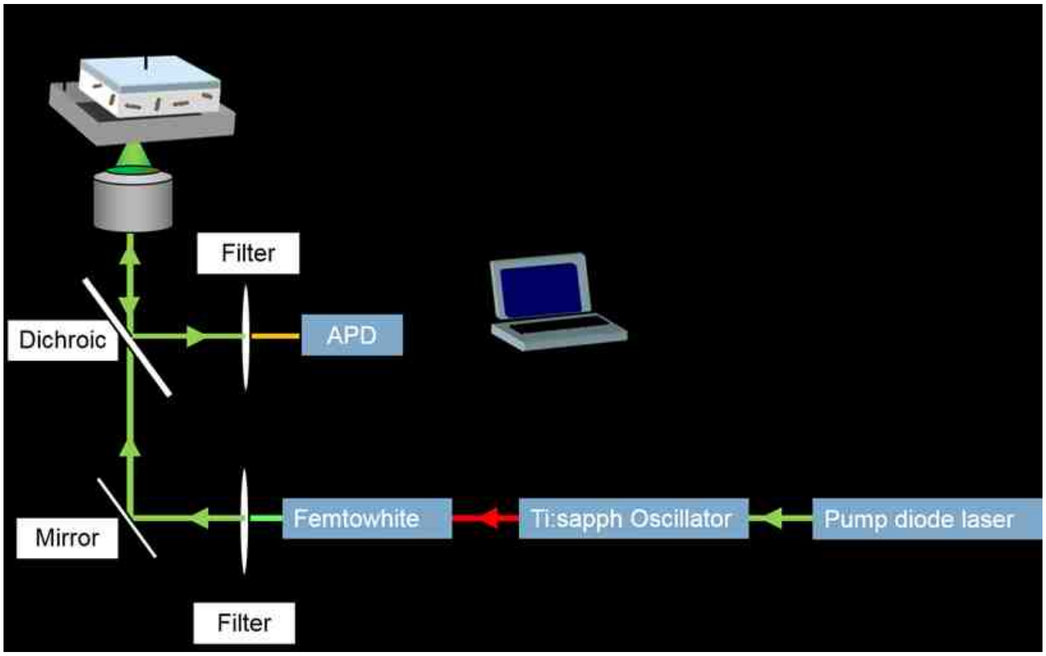

Figure 2.8 Experimental set-up for TCSPC experiments.

2.3 Vibrational spectroscopy:

Infrared absorption and Raman scattering by molecules are both examples of vibrational spectroscopy. While the mechanisms behind them and their selection rules are different, they both arise from the interaction of light with the chemical bonds within molecules. In specific, they both deal with the vibrational sub-levels of quantum mechanical electronic potential energy surfaces which are used to describe these chemical bonds. Vibrational spectroscopy, in contrast to electronic spectroscopy, deals with electronic excitations between vibrational sublevels of a single potential energy surface (PES). This is normally restricted to the ground state PES, but newer techniques such as stimulated Raman allow analysis of vibrational sublevels in excited electronic states.

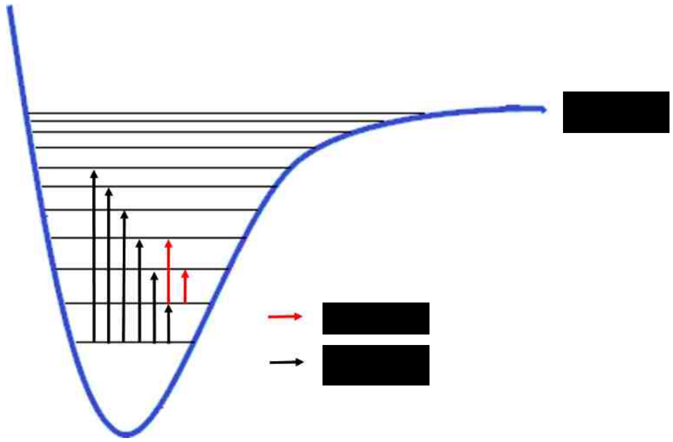

Figure 2.9 Ground state potential energy surface showing vibrational sub-levels and transitions between them.

2.3.1 Infrared spectroscopy

Infrared spectroscopy (IR) is based on electronic absorption of photons which correspond to the energy spacing between vibrational sublevels of a PES. For most materials at room temperature, the probability of states higher than the ground vibrational state being populated are low, therefore most IR spectroscopy deals with the vibrational sub-levels in the ground electronic state (see Fig 2.9). As well, the absorption frequencies tend to be in the infrared region of the spectrum as the changes in bond energy due to vibrational excitation are small. Not all chemical bonds can be vibrational excited through absorption. The primary rule of IR spectroscopy is that such an allowed transition must involve a change in the permanent dipole moment of the molecule in order to be allowed.

2.3.2 Raman

Raman spectroscopy is based on the light-matter interaction called Raman scattering. First proposed by Smekal in 1923[73], but verified experimentally by C.V.Raman in 1928[74], this scattering of photons by matter is inelastic, meaning that the emitted photon is of a different energy than the incident photon. A photon whose electric dipole is oriented parallel with the electric dipole of an electron in a molecular bond as it passes by can temporarily or “virtually” excite the electron to an excited state, and the instantaneous relaxation of the electron from this virtual state emits a photon of a different wavelength (see Fig. 2.10). The difference in energy between the absorbed and emitted photon is exactly equal to the energy difference in the vibrational sub-levels of the molecular bond’s ground state potential energy surface. Because the probability of the necessary and requisite conditions occurring in even solid state materials is very small, even with intense illumination, the Raman scattering cross-section for all materials is generally very small. The primary rule of Raman spectroscopy is that for such a scattering process to be allowed there must be a net change in the polarizability of the molecule during the temporary or virtual excitation.

If the excitation light is equal to or above the energy of an electronic transition (absorption) within the material then the electron excited by the Raman scattering process exhibits an enhancement to the scattering cross-sections, as great as five or six orders of magnitude. This is called “resonance”, because the incident light is resonant with an electronic transition. Raman spectroscopy where the excitation light is resonant with an electronic transition is called resonant Raman (RRaman) spectroscopy. Not all molecular vibrations are enhanced equally by the resonance condition. Those molecular vibrations which are associated with the electronic transitions (the modes whose structure changes the most by nuclear rearrangement during excitation) and those modes which preserve the symmetry of the ground state are the modes which are enhanced by the resonance condition. Modes which are not enhanced by resonance become virtually invisible (their signal is on the order of the background noise) in RRaman spectroscopy

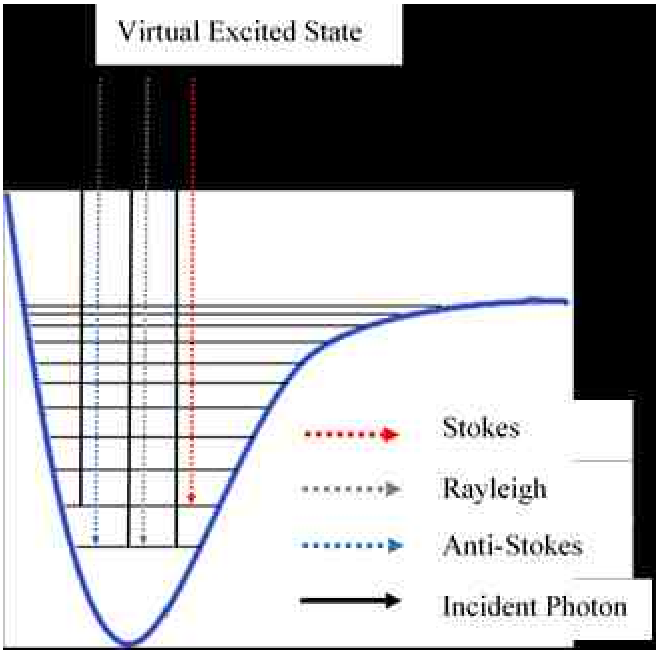

Figure 2.10 Ground state potential energy surface showing Raman scattering processes. Incident photons are shown by black arrows, grey arrow shows inelastic scattering (Rayleigh), blue arrow shows anti-Stokes scattering, and red arrow shows Stokes scattering.

The resonance condition has an important impact on the time scale of analysis during Raman spectroscopy. Normal Raman scattering which comes from a virtual state is instantaneous and reflects the vibrational structure of the molecule at ultra-short time scales (<1 ps). RRaman scattering comes for an excited electronic state, and the scattering process is not instantaneous. The excited electron can exist in the excited state for a longer time, (>1 ns). This allows for a unique, time-dependent, interpretation of RRaman spectra. The time-dependent theory of RRaman spectroscopy, developed by Heller[75,76], interprets the behavior of the excited state by the projection of a ground state wave packet to the excited state where the wave packet is allowed to change dynamically as a function of time (see Fig 2.11). The movement of the excited state wave packet in the excited state potential energy surface generates wavefunction overlap between the excited and ground state wave functions. If the wave packet is reflected at the edge of the PES, it may oscillate back in forth in the excited state multiple times before it decays. This wave packet oscillation, as well as a de-phasing or spreading out of the wave packet, can generate strong intensities in RRaman overtones

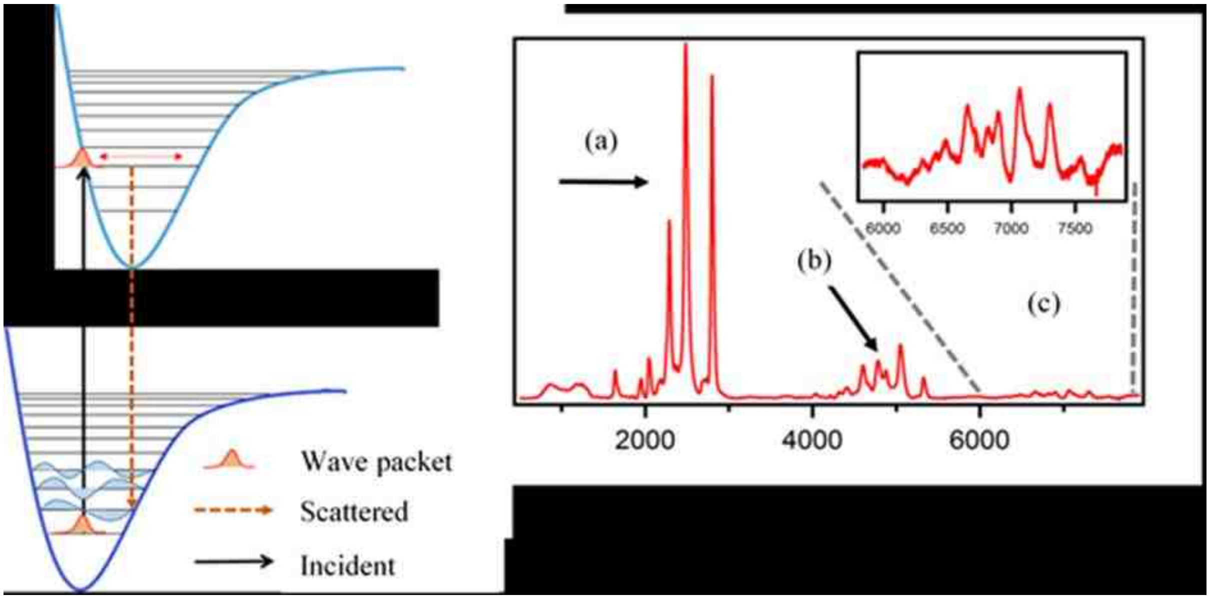

Figure 2.11 Diagram showing wavepacket oscillation in the excited state (left) which can generate intensity in Raman overtones shown in the experimental data (right). (a) fundamental Raman peaks, (b) first overtones, (c) second overtones.

Raman spectra were collected from samples using an inverted confocal microscope with a Zeiss achromatic 1.4 NA oil objective. Scattered light was collected using the same objective (back scatter configuration) and output directed to an Andor Newton Shamrock 303i spectrograph equipped with a water-cooled EMCCD detector.

High resolution data was collected using a 1700 l/mm holographic grating and low resolution spectra were collected using a 300 l/mm ruled grating with a 500 nm blaze. Raman imaging data was fit using custom scripts run in Igor Pro software.

2.4 Electrical Testing:

Standard photovoltaic device characterization begins with a fundamental electrical performance analysis. This is accomplished by attaching the device to electrical probes which can both apply and measure voltage and current. Once is done, the voltage applied to the device is swept from a negative voltage beyond the reverse-breakdown voltage to a positive voltage beyond the forward breakdown voltage (see Fig. 2.12). Current flow through the device is measured as the voltage is swept. This is done twice, once while the device is in the dark and again while the device is illuminated. The illumination is generally standardized for easy comparison with other devices, with this standard being set at the average solar intensity through a given type of atmosphere with a particular declination with respect to the sun. The most widely used standard is AM 1.5 set by NREL

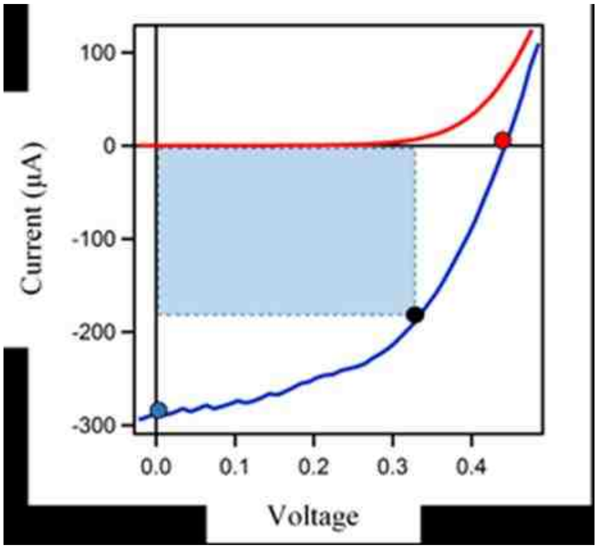

Figure 2.12 Typical I-V curves from an OPV device in the dark (red trace) and under AM 1.5 illumination (blue trace). JSC (blue dot), VOC (red dot), and point of maximum power production (black dot) are shown as well as the Fill Factor (FF) which is represented by the shaded blue rectangle.

Once these current-voltage (I-V) sweeps have been performed, device performance characteristics such as the fill factor (FF) and power conversion efficiency (PCE) can be determined. Series and shunt resistance values can also be calculated from the full scale version of these curves (not shown). The inverse of the slope of the curve between the forward breakdown voltage to the conduction point is the series resistance value, while the shunt resistance value is the inverse of the slope of the curve between the reverse breakdown voltage to zero bias.

Photocurrent “spectroscopy” is a means of imaging the current producing capabilities of working devices on a microscopic scale. Electrical probe leads are attached to the device while it is mounted in an x-y position stage on a microscope. Excitation light is focused to a diffraction limited spot on the device using a high numerical aperture objective, the device is raster scanned over the excitation spot, and the photocurrent produced from each spot is measured and recorded. All of this data is then compiled to create an image of current production correlated with physical position. This technique can be particularly useful when there is large scale phase separation within the film as current production may vary widely with composition and structure within these films. Photocurrent imaging can be informative, especially when coupled with structural information gained from Raman spectroscopy, about the structure-photocurrent relationship in OPVs.

Solar cell device performance metrics were measured using a Keithly 2400 source/ measure units. Illumination was provided by a calibrated xenon arc lamp (Newport Oriel) with an AM 1.5 filter. Measurements were taken in the dark and under illumination for all devices. Current-Voltage sweeps of dummy devices (capacitors) were taken using the same source/ measure unit but without illumination.

2.4.1 Optical frequency response measurements

Modulating the intensity of the excitation source and measuring the photocurrent or photovoltage produced by an operating PV device can also be used as a type of analysis. These techniques are called intensity modulated photocurrent (IMPS) and intensity modulated photovoltage (IMVS) spectroscopy (see Fig 2.13). The modulation frequency may be swept from very low frequencies (10 Hz) to very high frequencies (10 GHz) in these experiments, and the frequency dependent current or voltage response is collected. IMPS analysis can yield information regarding charge carrier formation and transit time, while IMVS analysis yields information regarding dielectric response (polarization) time within thin films devices.

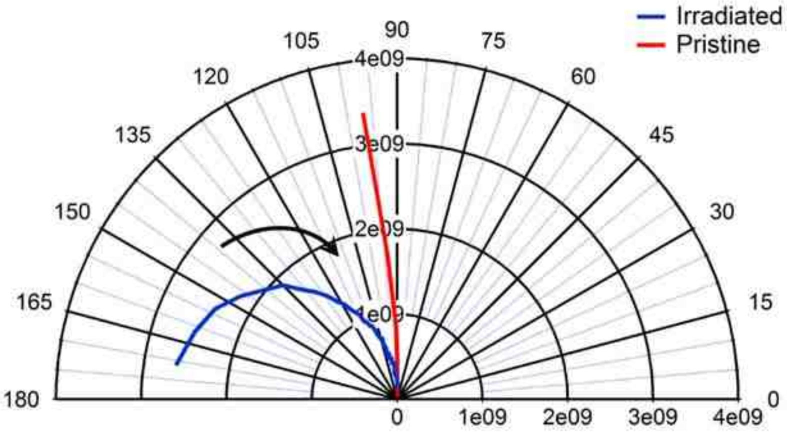

Figure 2.13 Polar plot of IMVS data for fresh OPV device (red trace) and irradiated OPV device (blue trace) showing the changes to the polarizability of the device active layer. At low frequencies the irradiated device shows a 180˚ phase shift which is indicative of the formation of an additional capacitive element in the active layer.

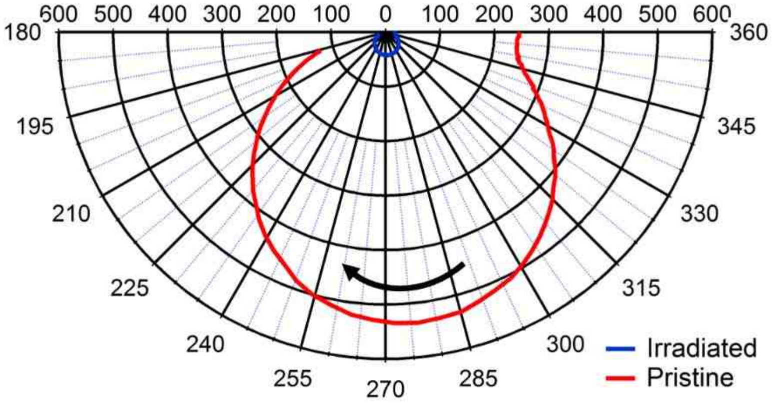

Figure 2.15 Polar plot of IMPS data for a fresh OPV device (red trace) and a heavily irradiated OPV device (blue trace). There is no change in the phase angle or lineshape of the traces. The damaged device simply shows a decrease in total photocurrent as a result of irradiation.

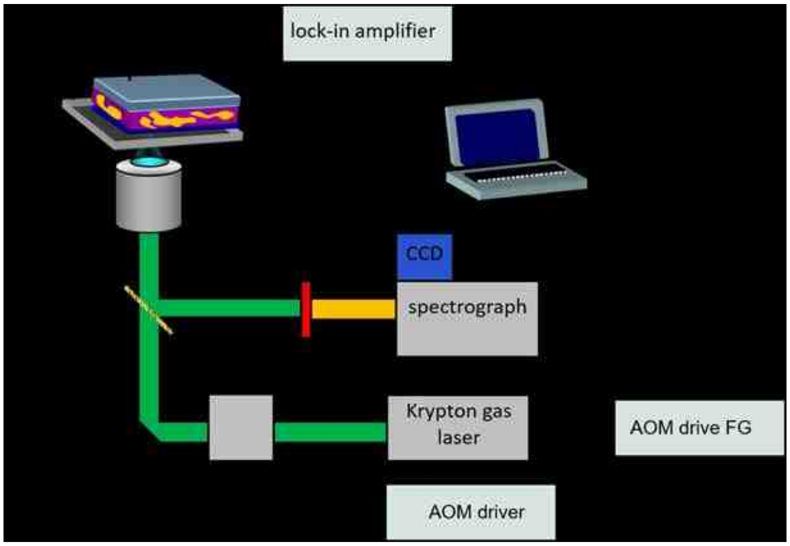

Figure 2.16 Experimental set-up for Photocurrent and Frequency Dependent Photocurrent Imaging.

2.5 Profilometry

Profilometry measurements were taken using a KLA-Tencor Alpha Step 500 profilometer. 5-10 measurements were taken in an “X” pattern over a film surface and the average of these measurements was reported. The profilometer was calibrated using a manufacturer supplied standard before each use.

2.6 Imaging

One of the most powerful techniques in materials analysis is imaging. Two and three dimensional maps, or images, of spectroscopic or electronic data can yield a wealth of information regarding the correlation between structure and function in organic electronic materials that cannot be captured with single-point or ensemble analyses. In addition, using multiple techniques to characterize a single sample area can lead to enhanced information correlation.

Imaging was performed using a nanopositioning stage (Mad City, Nanoview/M-XY) that was attached to the inverted confocal microscope. The stage was raster-scanned over the imaging area of a sample substrate positioned in a specialized sample holder located on the stage of the inverted confocal microscope. As the stage was scanned over the sample area, the stage would pause at each location and spectroscopic or electronic data collected. The ensemble of data points was then interpreted as a two-dimensional image from a preset number of points. While resolution in this microscopy system is diffraction limited with the high NA objective, stage step size was frequently smaller than the resolution limit to afford higher quality (non-pixelated) images.

Fluorescence imaging data was acquired using avalanche photodiodes mentioned previously in this section. Raman imaging data was collected using the Andor spectrograph, and photocurrent and frequency dependent photocurrent data was collected by a Stanford Research Systems SR830 lock-in amplifier (see Figure 2.16).

Chapter III

High Intrachain Order Promotes Triplet Formation from Recombination of Long-Lived Polarons in Poly(3-hexylthiophene) J-Aggregate Nanofibers

3.1 Introduction

Understanding the influence of conformation and packing on the electronic properties of conjugated polymers remains a long-standing challenge to optimize the performance of these materials for optoelectronic applications. In particular, the efficacies of energy and charge transfer along or through polymer chains as well as interactions and interconversion between electrically neutral exciton and charged polaron species are intimately dependent on the polymer structural attributes, which are usually difficult to control using conventional material processing techniques[77,78]. However, the tendency of some polymers to assemble into ordered, π-stacked aggregates can lead to efficient multidimensional (i.e., intra- and interchain) charge and energy transport, which offer researchers greater opportunities to tune material functionality and improve performance[79,80].

P3HT is perhaps the most recognized conjugated polymer system capable of forming extended aggregates, which has made it a benchmark material in solar cell and field-effect transistor applications. Following initial reports of efficient multidimensional charge and energy transfer in P3HT aggregates by Sirringhaus et al. and Osterbacka et al., respectively, numerous studies have sought to further exploit aggregates to understand and improve device performance figures of merit. The development of the weakly coupled HJ aggregate exciton model by Spano and co-workers has proven a powerful tool in these efforts, which relates microscopic structure and ordering information to exciton coupling characteristics and strength from one photon optical spectra[81]. This model has been used extensively in the study of P3HT aggregate optical and electronic properties and their dependence on intrachain (i.e., monomer coplanarity) and interchain (i.e., packing) order. Exciton coupling can be determined using the H/J aggregate model by comparing the one-photon absorption strength of the pure electronic origin transition (0-0) to the first vibronic sideband (0-1).5 0-0/0-1 values of <1 are found for H-aggregate exciton coupling (i.e., face-to-face dipole coupling), entailing greater interchain exciton character in the P3HT π-stack[82]. These excitons are most commonly observed in thin-film P3HT aggregates with low intrachain order arising from polydispersity-induced stacking faults and disorder[83]. On the other hand, 0-0/0-1 ratios of >1 have only recently been reported in P3HT aggregates, indicating high intrachain order that strongly attenuates interchain coupling (e.g., ,$k_B T$) due to extended intrachain exciton delocalization[50]. This is the J-aggregate coupling limit (i.e., head-to-tail coupling) that arises only in situations when molecular weight fractionation occurs during the aggregate assembly leading to very few stacking faults. Because conventional processing methods of P3HT functional forms (i.e., thin films) typically do not promote fractionation, this mode of exciton coupling is very rare in P3HT systems[54]. Our group has recently demonstrated that solution-based self-assembly of P3HT aggregate nanofibers (NFs, also known as nanofibrils or nanoribbons) can be used to select H/J exciton couplings through effective control of aggregate order and sizes as well as the boundaries between aggregated and amorphous domains. Importantly, the latter has been proposed to facilitate conversion of neutral excitons into free charge carriers (polarons), which makes the understanding and control of these features vital for further maximizing material performance[84]. This intrinsic charge generation mechanism has been demonstrated in P3HT thin films and has since generated interest in further understanding the structure-function relationships of this charge generation process[85,86]. Autoionization may also occur in single P3HT chains (typically within aggregates) either by hot exciton dissociation or delocalization-induced polaron pair formation[87,88]. In addition to forming charged species, long-lived triplet states may emerge and, together with polarons, interact with singlets generated on nearby chromophores via intra- or interchain mechanisms[67].

These interactions are mediated primarily by the polymer structural characteristics, but intrinsic nano- to micrometer scale morphological features tend to obscure specific molecular-level structural and conformational factors regulating triplet generation mechanisms and interactions.

Here, we study chain conformation- and packing dependent exciton interconversion, interactions, and dynamics in P3HT aggregates by self-assembling two limiting NF structures with well-defined packing and ordering characteristics. Single NF photoluminescence (PL) modulation spectroscopy and imaging techniques are used that have already seen extensive use as probes for understanding the roles of conformation and packing on photophysical outcomes in conjugated polymers[89–95]. Exciton−polaron interactions[96–98] and singlet−triplet interactions[97,99,100] can also be interrogated on sub-100 nm size scales, and we now extend these studies to single P3HTNF structures by measuring PL quenching dynamics on∼100 ns to 1 ms timescales. By carefully controlling the kinetics of nanofiber formation (i.e., solvent −solute interactions), the intra- and interchain order and, hence, exciton coupling within aggregates can be tuned, thus affording more accurate structure−function information[50,54]. To this end, two types of P3HT NFs are studied that represent the limits of excitonic degrees of freedom in P3HT aggregates, namely, (i) highly ordered, crystalline J-aggregates and (ii) less ordered, polymorphic H-aggregates[47,50]

Despite the fact that the HJ aggregate model was originally developed considering neutral and optically accessible singlet excitons, its underpinnings can be extended to understand exciton−polaron interactions and interconversion processes outlined above. Specifically, intra- and interchain (packing) order and coupling inferred from singlet-exciton optical transition line shapes can teach us how these structural factors influence the branching ratios of S = 1/2 polaron and S = 1 triplet formation mechanisms and their interaction with singlets over a broad range of time scales[93,96,101,102]. In particular, the high sensitivity of P3HT NF aggregate singlet-chromophore exciton coupling makes PL probes very attractive for elucidating the dependence of exciton−polaron and singlet−triplet interactions on chain-ordering characteristics, which is exceedingly difficult in thin films due to inhomogeneity effects[95,97]. We demonstrate efficient quenching of J-aggregate NF PL intensities on microsecond time scales from triplet states generated primarily from non-geminate recombination of long-lived, intrachain-delocalized polarons generated on earlier time scales from autoionization of singlet excitons. This mechanism of triplet formation is not effective in conventional thin-film aggregates and less ordered H-type NF structures, because their lower intrachain order instead localizes excitons or polarons, which promotes faster relaxation, trapping, and geminate recombination processes.

3.2 Results and Discussion

P3HT NFs were prepared and characterized using methods published earlier[50,54]. TEM images of H- and J-type NFs are shown in Figure 3.1a,b, respectively. H-type NFs are typically ~15-20 nm wide and have a rope-like, segmented appearance that stems from their rapid formation kinetics in anisole. J-type NF widths, on the other hand, are ~30-40 nm and have a more diffuse appearance reducing contrast in their TEM images, owing to slow self-assembly over several days in toluene. These conditions promote molecular weight fractionation, resulting in aggregates with very few stacking faults. This effect does not occur in H-type NFs assembled in anisole and instead leads to polymorphic structures with poorer aggregate quality. Consequently, exciton coupling and intrachain ordering of P3HT chains comprising these NFs are distinctly different and can be assessed from optical absorption and PL spectra (Figure 3.1c, d) using the HJ aggregate model. J-type NFs possess high intrachain order that attenuates interchain coupling[103] due to the delocalized nature of singlet excitons. Recent time-resolved PL polarization anisotropy measurements also revealed that J-type excitons remain intrachain in nature throughout their entire lifetime[51,104]. H-type NF excitons are localized from disorder effects resulting in lower intrachain order and larger interchain coupling with adjacent chains in the aggregate π-stack.

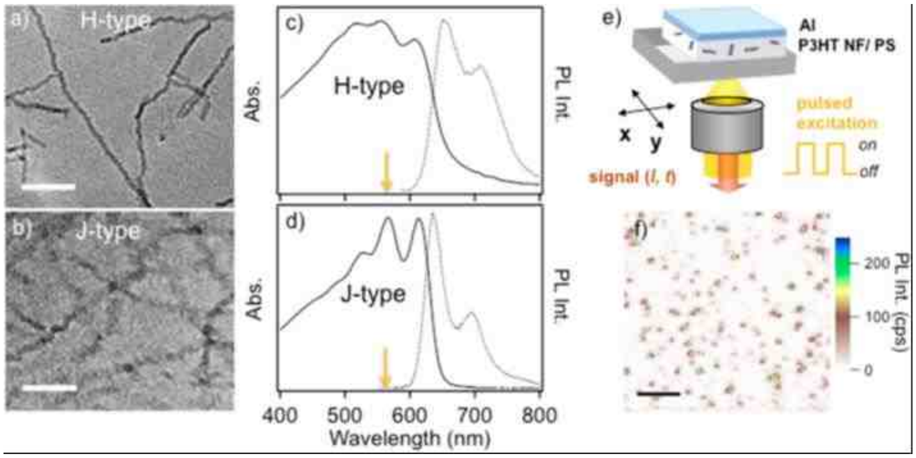

Figure 3.1 TEM images of H- (a) and J-type (b) P3HT NFs (scale bar = 200 nm). Optical absorption and PL spectra of H- (c) and J-type (d) P3HT NF dispersions. Arrows indicate excitation wavelengths used to excite PL in single NFs. (e) Scheme of excitation intensity modulated single-particle PL imaging and spectroscopy on P3HT NFs dispersed in Polystyrene (PS) and sealed with an aluminum overcoating. (f) Representative PL image of single NFs dispersed within the PS host matrix (scale bar = 5 μm).

Figure 3.1e highlights the experimental approach used in this study, where NFs are dispersed in an inert host matrix and interrogated using single-nanoparticle PL spectroscopy. The PL of individual NFs were excited using a sequence of laser pulses of varying intensities spanning the microsecond time scale regime. Samples were coated with aluminum to prevent unwanted photodegradation, and a typical PL image of well-dispersed NFs is shown in Figure 3.1f. Figure 3.2a displays a representative excitation intensity-modulated pulse sequence (I_{exc}) used to pump P3HT NF PL generated by shaping a CW laser with an acoustic optical modulator controlled by a function generator. Average excitation powers used were ~50 nW, corresponding to peak intensities of approximately 20W/cm^2 (I), 95 W/cm^2 (II), 220 W/cm^2 (III), and 370 W/cm^2 (IV), and pulse cycle periods ranged from 500 μs up to 5 ms. Figure 3.2 b, c show representative excitation intensity-dependent PL transients from H- and J-type P3HT NFs, respectively, recorded by synchronously averaging many pulse cycles using a multichannel analyzer (MCA). Once the laser turns on, the singlet-exciton PL intensity rises to its maximum (I_0) within the instrument-limited time resolution (~100 ns) usually followed by decay to a steady state level (I_{SS}) at later times. Quenching dynamics time scales are similar between NF types, showing PL modulation, but quenching depths (I_0/I_{SS}), however are markedly different depending on the packing and intrachain order of chains within the NF aggregates. Excitation intensity-dependent transients were measured from many NF particles for each type (>100), including different batches, that show similar behavior as reported in Figure 3.2 b, c.

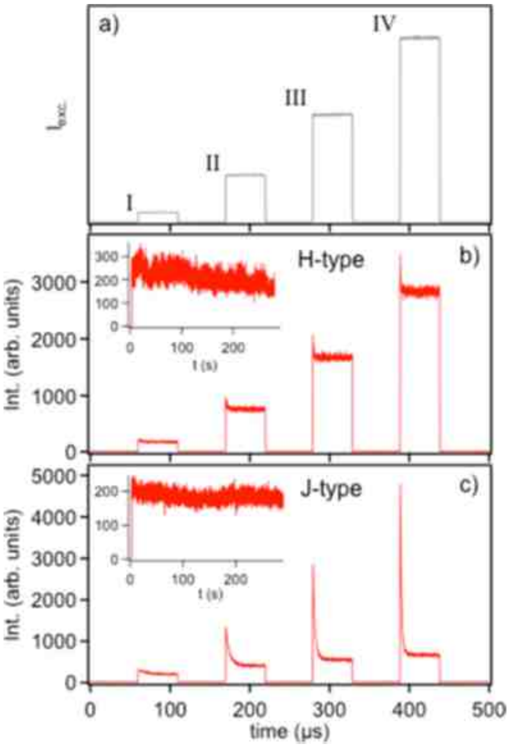

Figure 3.2 (a) Typical laser pulse excitation profile generated from scattered excitation light. See text for characteristic peak intensities for each pulse. Excitation intensity dependent transients were recorded using a multichannel analyzer (MCA) that synchronously averaged over many excitation cycles. (b, c) Representative transients of H-type and J-type P3HT NFs from over 100 individual particles. Insets show corresponding PL transients averaged over longer times (~110 ms) with a multichannel

scalar. These longer time transients were used to assess the NF photostability characteristics over the course of the experiment.

Polymorphic H-type NFs show relatively small average quenching depths ($I_0/I_{SS} \leq$ 1.2, Figure 3.2b) for particles displaying any discernible quenching (~30%) whereas the majority of particles studied (62%) displayed no PL quenching. Conversely, J-type NFs exhibit much larger quenching depths (I_0/I_{SS} g2) for ~70% of all particles studied, and PL modulation characteristics were independent of particle size (brightness, Figure 3.2c) as well as the overall excitation cycle frequency (see Supporting Information). A small fraction (7%) of all H-type NFs studied did show larger PL quenching depths, suggesting some of these structures are more J-like in nature. In a previous study of H-type NFs fabricated in anisole, PL excitation spectroscopy revealed that line shapes are dominated by minority, lower energy emitters populated by energy transfer from nearby higher energy chromophores[105]. Upon dispersing NFs in inert hosts, fragmentation occurs to varying degrees, meaning that energy transfer pathways are broken, and we propose the small fraction of H-type NFs displaying large PL quenching depths reflect these minority emissive traps. In a similar vein, approximately 20% of J-type NFs showed lower PL quenching depths (I_0/I_{SS} <1.5) that were mostly smaller (i.e., less intense) particles. For comparison, the same experiment was performed on regioregular P3HT thin films and P3HT nanoparticles prepared using reprecipiation techniques that, like most H-type NFs, exhibited no PL quenching regardless of excitation intensity. The smaller PL quenching response observed in H-type NFs further demonstrates these morphologies more closely resemble those of thin films (i.e., smaller aggregates with low intrachain order bordered by interpenetrating amorphous chains).

There is an additional possibility that fragmentation of NFs upon dilution and dispersion into polystyrene hosts can result in the presence of single P3HT molecules[50], which may contribute to unwanted background signal modulation. However, single P3HT molecule PL intensities are much lower than NFs, and measurements of backgrounds showed no evidence of PL quenching. NF PL transients (insets in Figure 2 b, c) recorded on longer time scales (∼1-10 ms dwell times/channel) with a multichannel scaler show good photostability when subjected to pulsed excitation, unlike single molecules, which normally tend to flicker and degrade much faster. Longer time scale PL transients from anisole H-type NFs frequently exhibited small fluctuations between intermediate levels but usually not much larger than the shot noise, which probably originates from stochastic switching due to energy transfer between distinct domains within the NF structure. Importantly, quenching depths and dynamics were dependent on excitation intensity (Figure 3.2 b, c), revealing key insights into the mechanism(s) of PL quenching in P3HT NFs (vide infra).

We now focus on J-type P3HT NFs and classify their PL quenching ratios and decay time scales to identify the dominant quenching species and their possible formation mechanism(s). Representative distributions of I_0/I_{SS} values and decay times are shown in Figure 3.3a,b, respectively, within a particular sample (I_{exc} = 350 W/cm^2). Average I_0/I_{SS} values for J-type NFs are ~3.6 for excitation intensities of >250 W/cm^2. A single-exponential decay function of the empirical form

$$I_{(t)} \propto I_0 \exp(-t/\tau) I_{SS} \quad (1)$$

was fitted to excitation intensity-dependent MCA transients, and quenching time scales (I_{exc} = 350 W/cm^2) were compared to I_0/I_{SS} values (Figure 3b). Larger I_0/I_{SS} values (>2) correlate with faster quenching dynamics, a trend noted earlier in intensity-dependent PL quenching of single polymer molecules[93], but decay time scales associated with smaller I_0/I_{SS} values (~1.5 or less) have a broader range (i.e., ~1-10 μs). The variation of quenching dynamics and I_0/I_{SS} with excitation intensities indicates a bimolecular process[106], probably involving multiple steps preceding PL quenching time scales observed here

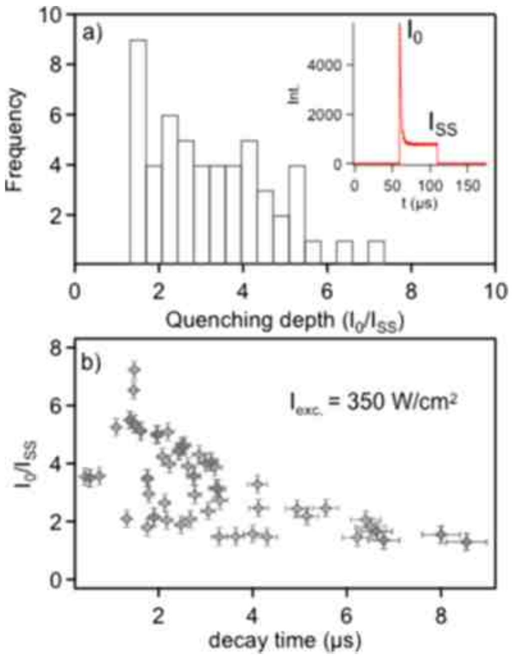

Figure 3.3 (a) Histogram of I0/ISS values of many J-type P3HT NF samples and (b) comparison of I0/ISS with decay times generated from single-exponential fits for a particular laser excitation intensity (I_{exc} = 350 W/cm2)

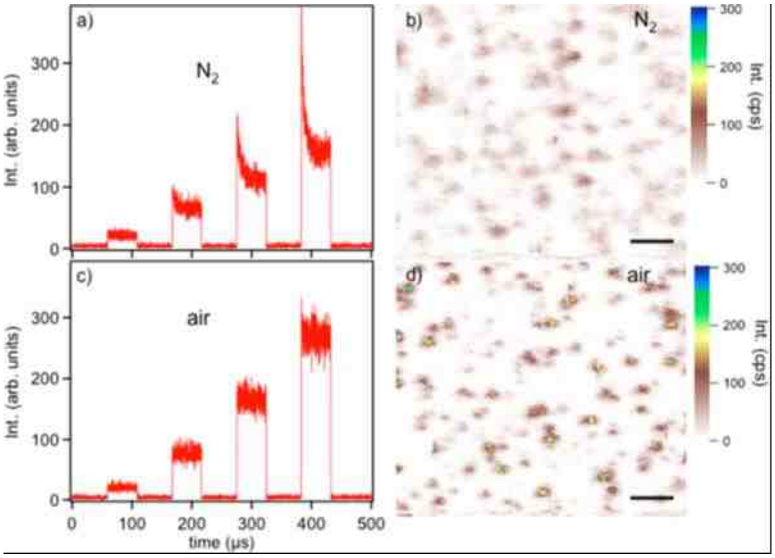

Figure 3.4 Representative single J-type NF intensity-dependent PL transients and images measured under N2 (a, b) and air (c, d).

On the basis of previous photophysical studies of P3HT and related polythiophene systems, it is straightforward to arrive at two likely candidate PL quencher species in P3HT NFs, namely, polarons and triplet states. Polaronic species, such as free charges or loosely bound, uncorrelated polaron pairs, are often present in appreciable levels, but their optical cross sections are generally weak and spectral line shapes are broad and unresolved. As mentioned briefly in the introduction, the generation of polarons or polaron pairs in neat polymers has become an increasingly important topic for reconciling performance characteristics in optoelectronic devices[85], but it is difficult to reliably control the yields of polaronic species in conventional thin film structures due to morphological inhomogeneity. Interestingly, embedding single molecules in model unipolar OLED-type devices has demonstrated that polaron levels can be controlled with device bias, thus allowing detailed molecular-level studies of exciton− polaron interactions[101].

Triplet excitons are relatively long-lived and can quench emissive singlets by energy transfer[107]. Triplets have received considerable attention for polymer solar cell applications since population of these low-energy states can be particularly detrimental because chromophores are effectively removed from photoexcitation cycling into allowed singlet states[108]. Strategies to either utilize or mitigate triplets have been pursued that have sought to take advantage of their longer lifetimes and, hence, larger diffusion lengths, although some studies suggest similar migration length scales as singlets[107]. The specific structural factors regulating triplet formation mechanisms and yields in polymers and related aggregates are still debated, but the prevailing consensus is that chromophore structural characteristics, such as intra- and interchain order, play an important role in determining triplet yields and dynamics[107]. Unfortunately, the subtle aspects of chain conformational and packing order are often masked in thin-film and solution spectroscopic studies from ensemble averaging effects. As demonstrated in Figures 2 and 3, these limitations can be circumvented in self-assembled NFs, especially for J-type NFs, owing to the ability to direct polymer conformation and packing.

Despite the promise of self-assembled NFs to resolve exciton– polaron interconversion and interactions, distinguishing either polarons or triplets as singlet exciton quenchers in P3HT NF intensity-dependent transients can be a difficult task because they may coexist and interact over similar time scales. However, when triplet energies are >1 eV, the presence of oxygen quenches triplets by efficient energy transfer, thus sensitizing singlet oxygen, thereby providing a valuable diagnostic tool for revealing the presence of these states in NFs. We now perform single NF imaging and excitation intensity-dependent transient studies by regulating the atmosphere over NF solid dispersions. Samples for this study were processed without the aluminum overcoating and placed in a flow cell, where they were initially kept under a dry N_2 environment. Ambient air was then bled into the flow cell, and NF PL images and transients were recorded to help uncover the identity of the dominant quenching species in J-type NFs. Figure 4 shows representative J-type single NF spectra and PL images under N2 (a, b) and exposed to air (c, d) using the same average laser power (~50 nW).

Unsealed samples recorded under dry N2 environments show the typical efficient intensity-dependent PL quenching behavior albeit with somewhat lower signal-to-noise ratios because they lack the metal overcoating (Figure 3.4a). PL quenching behavior in single J-type NFs disappears or is strongly attenuated almost immediately after samples are exposed to air (I0/ISS ~1), consistent with previously published oxygen diffusion constants in P3HT[109]. Average PL intensities initially display small, transient increases, which is discernible from comparison of the integrated intensities of transients before and after exposure to ambient air (Figure 3.4a,c), but then subsequently decrease from irreversible photodegradation processes. Excitation intensity-dependent transients were also recorded simultaneously with PL image acquisition by averaging over all particles in the image field-of-view that show similar behavior to single NFs in Figure 3.4a,c. The same experiments were performed on H-type NFs, and virtually no change in PL quenching behavior was observed upon exposure to air, demonstrating a much smaller amount of oxygen-sensitive quenchers formed.

The strong sensitivity of J-type NF PL quenching behavior to the presence of oxygen and lack of extended dark periods in corresponding PL transients indicate the dominant quenchers are triplet states. Previous reports of excitation intensity-dependent triplet quenching in single poly(3-octylthiophene) (P3OT) molecules showed similar behavior where average PL intensities increase substantially upon introduction of oxygen[110]. Schindler et al. performed PL imaging and transients on single ladder-type, poly(para-phenylene) molecules (MeLPPP) and were able to induce controlled bursts by introduction of air in the sample[111]. More recently, Steiner et al. used fluorescence correlation spectroscopy (FCS) to measure “on” and “off” times due to triplet blinking on single P3HT chains of varying molecular weight[93]. These authors found “on” times ranging from ~5 to 10 μs, which are comparable to PL quenching time scales reported here. Using the reported bimolecular rate constant of triplet quenching by oxygen in structurally similar P3OT (kQ = 1.4×10^{9} M^{-1} s^{-1})41 as an upper limit for P3HT aggregate triplets, triplet deactivation is expected to be very efficient in J-type NFs assuming high intrachain mobilities.

Further confirmation of triplets as the dominant quenchers in P3HT NFs comes from detailed electron spin resonance and optically detected magnetic resonance studies of P3HT. Sperlich et al. observed both reversible and irreversible interactions with oxygen[112], where the latter proceeds via triplet states. Reversible interactions with oxygen were shown to involve singlet excitons that usually manifest as long “off” times in PL transients of single polymer molecules from charge transfer complex formation with oxygen[97]. The introduction of ambient air into unsealed J-type NF samples, along with larger peak intensities from pulsed excitation, accelerates photodegradation and loss of PL signal due to the highly electrophilic character of singlet oxygen generated by triplet sensitization, which is not characteristic of a reversible charge transfer complex interaction[112]. Although these types of interactions with oxygen are possible and commonly observed in single-molecule spectroscopy of polymers, they are probably masked in our data owing to the multichromophoric nature of NFs.

3.3 Mechanisms of Triplet Formation in J-Aggregate P3HT Nanofibers

Despite apparent efficient triplet generation and quenching in J-type P3HT NFs, it is noteworthy that previous transient absorption spectroscopic studies of regioregular P3HT thin films instead showed preferential polaron generation[86,87]. This situation changes dramatically in P3HT solutions, where appreciable triplet populations were reported in P3HT chains with significant dynamic conformational disorder[113]. From comparison of intensity-dependent PL transient trends from H- and J-type NFs, the stark contrast in apparent triplet–polaron branching ratios in these P3HT forms can most readily be traced to differences in chain conformational and packing order. Similar dependences were reported earlier from photophysical studies of amorphous (glassy) and crystalline (β-phase) poly-(9,9-di-n-octylfluorenyl-2,7-diyl) thin films, which show much lower triplet populations for the planar β-phase due to efficient polaron generation[114].

The expected low triplet yields observed in polymer thin-film aggregates raise questions regarding the mechanisms in effect for efficient triplet generation in J-type NFs. It is first important to point out that the structural qualities of these aggregates are significantly different from those typically encountered in conventional polymer thin films and solution phase conformations. We propose that the unusually high intrachain order and packing integrity of these aggregates play key roles in determining the photophysical outcomes resulting in triplet formation, and we now consider several candidate triplet mechanisms known to be operative in conjugated organic molecules, namely, (i) singlet fission; (ii) intersystem crossing (ISC); and (iii) non-geminate polaron recombination to triplets.

Singlet exciton fission has received a great deal of attention lately for its potential to increase yields of photogenerated charge carriers in solar cells[103]. This process involves conversion of optically allowed singlet states into two spin-forbidden triplets on neighboring chromophores promptly following photoexcitation[115]. However, singlet excitation energies must be at least 2 times larger than the lowest energy triplet ($E_{S1} \geq 2E_{T1}$), making singlet fission more efficient in chromophores with large exchange energies and $S_1 - T_1$ energy gaps (ΔE_{S-T})[115]. Although singlet fission was shown to generate triplets on ultrafast time scales in P3HT solutions[87], we rule it out as a likely mechanism of PL quenching by triplets on microsecond time scales (Figures 3.2 and 3.3) since high intrachain order in J-type NFs and persistent, delocalized intrachain exciton character over its entire lifetime should result in lower exchange energies and ΔE_{S-T}[116]. Moreover, the excitation energy used to excite PL (568 nm, 2.18 eV) is not far above the optical gap, which would further reduce singlet fission efficiency.

Excited-state spin crossover on conjugated organic chromophores is more commonly reported on longer time scales (>1 ns), which typically corresponds to ISC events requiring sufficient spin−orbit coupling[116]. Bredas and co-workers calculated the ISC rate constant for planar oligothiophenes (idealized C_{2h} point group symmetry) and predicted very small triplet yields since spin−orbit mixing of the lowest energy excited singlet (^1B_u) and triplet (^3B_u) is possible only for the z-component (A_g) of the spin−orbit coupling[117]. This mechanism requires an out-of-plane backbone distortion in order to achieve nonzero spin−orbit S_1−T_1 mixing, which is better realized in solution-like, P3HT chain conformations with dynamic conformational disorder[117]. The stringent symmetry factors imposed by relatively planar P3HT chains in J-type NFs could possibly be circumvented by the expected lower exchange energies mentioned above. Consequently, smaller ΔE_{S-T} values could result in an increase of the ISC rate constant, although spin−orbit mixing of singlets and triplets is small[118]. Previous studies of exchange energies in a variety of polymers show a near constant value (~0.7 eV) in addition to similar ΔE_{S-T} values[107]. It is important to stress these studies were performed in solution and solid thin films with non-fractionated samples, which could potentially mask contributions from minority chains with high intrachain order common to J-type NFs. A comparison of heavy atom effects in π-stacked aggregates with high conformational order could perhaps better assess ISC yields, but such materials are not presently available for this study[119].

Another intriguing ISC pathway involves coupling S_1 to higher energy triplet states (T_n) in closer energetic proximity to S_1 with favorable symmetry followed by rapid internal conversion to the lowest energy triplet, T_1. This multistep process essentially mimics lowering exchange energies, but triplet−triplet absorption spectra of P3HT and related polymer systems show no evidence of higher energy triplet states in the energetic vicinity of the S1 state[107]. At this stage, it is not possible to definitively rule out ISC as a viable mechanism for efficient generation of triplets in J-type NFs. Nonetheless, the structural and symmetry factors responsible for the dominant J-aggregate exciton coupling conflict with established literature trends relating structural factors and $\Delta E_{S\text{-}T}$ indicating that ISC should not be efficient.

Similar to previous studies of autoionization processes in regioregular P3HT thin films, Martin et al. measured ultrafast transient absorption spectra for H- and J-type P3HT NF dispersions and found no distinct triplet signatures appearing on time scales ranging from ∼200 fs up to ∼1 ns[105]. On the other hand, delocalized polarons (DP) and intrachain polaron pairs (PP)[120] were reported with significantly longer lifetimes in J-type NFs compared to their H-type counterparts[105]. At early time scales (<200 fs) the PP:DP change in optical density (ΔOD) signal ratio was 10:1 for J-type NFs compared to a value of 1.5:1 found in anisole-assembled H-type NFs[105]. This result highlighted the stark contrast of intrachain order in both NF types, which serves to delocalize excitons and increase electron–electron correlation lengths. Although PP relaxation times were similar for both NFs[104], DP species showed much slower relaxation dynamics ($\tau > 2$ ns) in J-type NFs since they are more sensitive to interchain coupling[105], which is virtually absent in these aggregates.

The long-lived nature of uncorrelated intrachain DP species potentially sets the stage for non-geminate recombination at later times when these populations become significantly larger than earlier time scales probed by ultrafast spectroscopy. According to simple spin statistics, recombination of uncorrelated polarons to triplet vs singlet states should have a 3:1 branching ratio, respectively. Similar triplet generation mechanisms were proposed in para-hexaphenyl[121] and poly-(phenylene-vinylene)[67], although the ordering and size of these chromophores are probably lower than in J-type P3HT NFs. Because PP and DP species tend to recombine geminately on much faster time scales in H-type NFs due to the more localized character and larger interchain coupling, triplet recombination yields in these aggregates are expected to be small, resulting in much lower or no PL quenching on microsecond time scales, as shown in Figure 2b. This result is also consistent with previously reported low triplet yields in P3HT thin films owing to the morphological similarities between films and H-type NFs.

It is also noteworthy that several groups have demonstrated that polaron recombination does not always follow simple spin statistics. For example, increasing conjugation lengths (e.g., regioregular aggregated P3HT vs regiorandom amorphous P3HT) tends to favor increased recombination to singlets, which is consistent with smaller ΔE_{S-T}[122,123]. While our present results do not enable us to quantitatively estimate the triplet populations from PP/DP recombination, the longer triplet lifetime and expected diffusion lengths still result in effective PL quenching of singlet excitons, even at lower populations than predicted from spin recombination statistics. On the basis of these considerations, we attribute triplet formation on >1 ns time scales in J-type NFs largely to non-geminate recombination of polarons generated on earlier time scales.

Regardless of the specific mechanism of formation, the spin-forbidden, non-radiative relaxation back to the ground electronic state (S_0) of triplets occurs by reverse ISC and should be similar to values reported from other P3HT forms (i.e., thin films, nanoparticles, and single molecules). We use a sequence of two excitation pulses delayed with respect to each other that reveal triplet quencher relaxation time scales via reverse ISC and compare the results to established literature trends. A steady-state triplet population is generated by the first PL excitation pulse that subsequently decays to S_0 in the dark by reverse ISC once the pulse shuts off. By delaying the second pulse to excite the NF particle within the expected triplet lifetime, the ratio of initial intensities generated from both pulses ($I_0[1]/I_0[2]$) with respect to the pulse time delay (Δt) exposes the presence of unrelaxed triplets apparent from quenching of $I_0[2]$ levels

Figure 3.5 shows representative J-type NF spectra generated in samples with aluminum overcoatings at short (a, 5 μs) and long (b, 40 μs) delays. $I_0[1]/I_0[2]$ values are plotted with their respective delay time, Δt, for a single NF and average over ~30 particles collected over various delay times

A single-exponential fit to these curves produces an average time constant of ~9 μs, which we assign to reverse ISC back to the ground S0 state (Figure 3.5d). This value is within a factor of 2 of reverse ISC rate constant estimates determined from single P3OT molecules (kISC0 ~16 μs) using a coupled photodynamic model in addition to average "off" times of 18 μs determined from FCS measurements of single P3HT molecules[93]. The faster triplet relaxation time scales found in NFs are consistent with observations from previous studies of size-dependent energy transfer and polaron dynamics in conjugated polymer nanostructures[91].

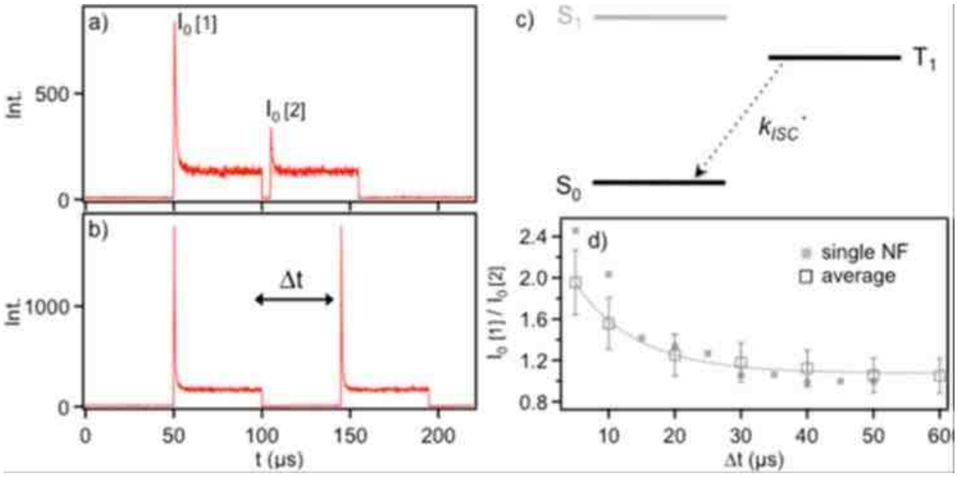

Figure 3.5 (a, b) Variable pulse time gap single NF PL experiment on sealed NF samples. Pulses of the same intensity and duration are delayed on time scales of∼5100 μs. (c) Reverse ISC process probed by the variable time delay pulsed excitation PL experiment. (d) Comparison of initial intensities (I0) for each pulse and their respective time delays (Δt) for a single NF (solid squares) and ensemble averaged NFs acquired from many individual particles for each time delay.

While increasing Δt in these experiments does increase peak excitation intensities, taking the ratio of I_0 values from both pulses removes this dependence, allowing for comparison of triplet relaxation between various pulse delay times. Moreover, quenching dynamics time scales were always within the range reported earlier in Figure 3.3. PL rise times for both pulses were also identical and showed no variation with the delay time of the second pulse.

3.4 Conclusions

We have shown that high intrachain order in J-type P3HT NFs facilitates delocalization of excitons, leading to the eventual formation of triplets from non-geminate recombination of delocalized polaron species. These mobile triplets interact with emissive singlet excitons and lead to efficient PL quenching on microsecond time scales. The identity of triplets as the dominant quenching species was confirmed from the strong sensitivity of PL modulation depths, I_0/I_{SS}, to the presence of oxygen. By comparing excitation intensity dependent PL quenching responses from J-type and less-ordered H-type NFs, previously reported low triplet yields encountered in thin films can be explained in terms of P3HT chain ordering within the aggregate. Namely, lower intrachain order in H-type P3HT aggregates localizes excitons and polarons, making non-geminate polaron recombination to triplets inefficient due to the dominance of faster geminate recombination processes. Overall, our results demonstrate the potential of self-assembled polymer nanostructures to understand and, ultimately, control the photophysics responsible for populating various spin states over a wide range of time scales. We further propose that reliable control of polymer intrachain order within coupled, multichromophore systems might eventually prove useful for manipulating spin populations and transporting these species over larger distance scales than what is currently possible in conventional polymer functional forms.

Chapter IV

Interchain Charge Transfer States Mediate Triplet Formation in Purified Conjugated Polymer Aggregates

4.1 Introduction

The formation of electrically neutral, spin-forbidden triplet excitons in conjugated organic polymer materials is generally regarded as a loss channel for various optoelectronic device applications, such as solar cells and light-emitting diodes[66,124–127]. Ongoing efforts aimed towards either bypassing or harvesting these long-lived states* have had limited success due to the lack of detailed, molecular-level structure-function relationship information governing triplet formation. Recent reports of singlet fission[128] in conjugated organic small molecule and polymers alike have inspired new debate over the structural and electronic factors governing the efficacies of this and other perturbative triplet generating mechanisms, such as intersystem crossing[117,129,130]. However, heterogeneity arising from polydispersity or polymorphism presents serious obstacles for elucidating mechanistic details of triplet formation and controlling their branching ratios.[72,131,132]

Here, we use self-assembly approaches to effectively manage polydispersity induced disorder effects in conjugated polymer aggregates, which generates new insights into the structural factors regulating exciton delocalization, coupling and spin conversion. Purified aggregate nanofibers of poly(3-hexylthiophene) (P3HT) are assembled via the whisker method in toluene solutions over long periods of time (>24 h). These nanofibers consist of single P3HT chains folded into highly anisotropic π-stacked conformations with stem lengths often exceeding 40 nm and interchain stacking distances of ~3.7 Å.[52,133] Importantly, only the higher molecular weight fraction forms aggregates[54] and individual chains subsequently associate into extended nanofiber structures leading to morphologies distinct from more common P3HT aggregate fibrillar nanostructures.[78] Fractionation, or, purification, towards higher molecular weight chains leads to high intrachain order (monomer co-planarity) within aggregate π-stacks[86], which promotes delocalization of singlet excitons along the intrachain direction over their entire lifetime.[51,134] The exceptionally large conjugation lengths (coherence lengths) arising from purified aggregates gives rise to spectroscopic signatures resembling classical J-aggregates, i.e., the strength of the electronic origin transition (0-0) is always larger than that of the vibronic sidebands (0-n, n≥1).[135,136]

In contrast, unfractionated aggregates typical of P3HT thin films possess more stacking faults and torsional disorder (i.e., low intrachain order).[78] Franck-Condon activity of backbone torsional vibrations and interchain Coulombic dipole-dipole interactions causes photogenerated singlet excitons to self-localize rapidly (<1 ns)[83,137,138]. The dominant interchain character of these excitons produces spectroscopic signatures resembling H-aggregates.[83,139] By comparing H- and J-aggregate structures, we now show that intrachain order plays a crucial, but subtle, role in regulating excited state relaxation pathways, such as exciton spin state conversion.[123,140]

Recently, there has been increased interest in the roles of optically dark charge transfer (CT) states in mediating excited state relaxation processes, in particular, spin state interconversion. CT states are especially important for determining the performance metrics of solar cells based on organic donors and acceptors[66,141] but may also impact pristine materials due to significant overlap of electron-hole wavefunctions on neighboring polymer segments. This interaction is mediated chiefly by the conformational and packing characteristics of individual chains and can vary significantly over the material due to heterogeneity. Interestingly, Spano and co-workers demonstrated that, in the regime of large exciton coherence lengths, the through-space dipole-dipole coupling contribution vanishes and, instead, the sign of the electron-hole wavefunction overlap determines the exciton character.[47] It was further proposed that manifestations of wavefunction overlap should only be apparent in polymer aggregates with high purity (i.e., high intrachain order), such as P3HT J-aggregates. Most importantly, this description requires the inclusion of interchain CT states originating from electron (hole) transfer to adjacent chain segments (stems) in the aggregate π-stack.[47] It was further shown that CT states can mix with J-type exciton states but not with H-type excitons due to symmetry constraints.[47]

In the following, we show that P3HT J-aggregate nanofiber excitons possess significant CT character that we propose act as triplet precursors. Time-resolved, electric field-dependent single molecule photoluminescence (PL) spectroscopy of isolated J-aggregates reveals large modulation of a long-lived PL decay component that we attribute to the delocalized exciton with CT state admixture. We further demonstrate that the relative densities of CT states and triplet yields increase with nanofiber size. We propose that increased CT character in delocalized intrachain excitons lowers singlet-triplet exchange splitting that, at longer times, leads to triplet exciton formation. Our results demonstrate the importance of subtle chain ordering on exciton delocalization and the importance of interchain CT states as conduits for exciton spin conversion processes.

4.2 Results and Discussion

CT states have received greater attention due to their roles in mediating excited state photovoltaic processes[142] and spin conversion processes. These states are intermolecular in nature and typically weak overlap of the separated carrier wavefunctions makes direct spectroscopic identification difficult. To better elucidate the presence and structural origins of these dark states in P3HT J-aggregates, we begin by investigating size-dependent exciton properties and triplet quenching of nanofiber PL emission. Signatures of delocalized intrachain (J-type) excitons only become apparent in P3HT aggregates when significant purification occurs during assembly, which is accomplished using selective solvation of various molecular weight fractions. Optical absorption spectroscopic lineshapes are monitored during the J-aggregate nanofiber assembly process to assess the fundamental nature of excitons and coupling mechanisms.

Figure 4.1a shows the evolution of J-aggregate P3HT nanofiber absorption spectra in toluene solutions over a period of ~24 hours at a constant temperature of ~22 °C. Following initial cooling, well-resolved absorption line shapes emerge at lower energy with 0-0/0-1>1 and relatively sharp vibronic linewidths (FWHM~350 cm^{-1}). The inset in Fig. 4.1a shows a representative absorption spectrum of a nascent J-aggregate, which are comprised of well-folded single chains corresponding to the high molecular weight fraction of the total distribution. Based on earlier TEM imaging studies[133], X-ray diffraction[143] and time-resolved fluorescence polarization anisotropy measurements[51], P3HT segments within J-aggregate conformations are highly planarized which support extended exciton and polaron delocalization.[52,133]

The rapid emergence of well-resolved J-aggregate signatures in Fig. 1a is consistent with our earlier model consisting of single P3HT chains folded into highly ordered, anisotropic conformations that subsequently associate into hierarchical nanofibers. Vogelsang et al. demonstrated similar rod-like conformations could be produced in non-crystalline, alkoxy substituted poly(phenylene-vinylene) (PPV) derivatives by solvent vapor annealing of isolated polymer chains in dilute solid dispersions. By carefully controlling the polymerization synthesis and processing conditions, Mazzio et al. observed J-aggregate-like features in thin films of high molecular weight and regio-regularity. Fauzell et al. very recently demonstrated similar motifs in a push-pull type conjugated polymer where chains self-fold into anisotropic conformations which then associate into larger structures. These authors further note that the basic spectroscopic unit of aggregates can be as small as a single folded polymer chain.

Assuming a nominal molecular weight of ~80 KDa for the high molecular weight P3HT fraction, the expected contour length is ~100 nm or larger implying a single J-aggregate P3HT chain can fold onto itself at least 3×. At longer times (>24 hr.), nanofiber stacks reach lengths of 1-10 μm and J-aggregate signatures are diminished (i.e., 0-0/0-1 ratios <1) and accompanied by vibronic linewidth broadening compared to single chain building blocks. The apparent loss of J-aggregate character indicates a larger interchain coupling contribution leading to greater H-aggregate, or, interchain character.

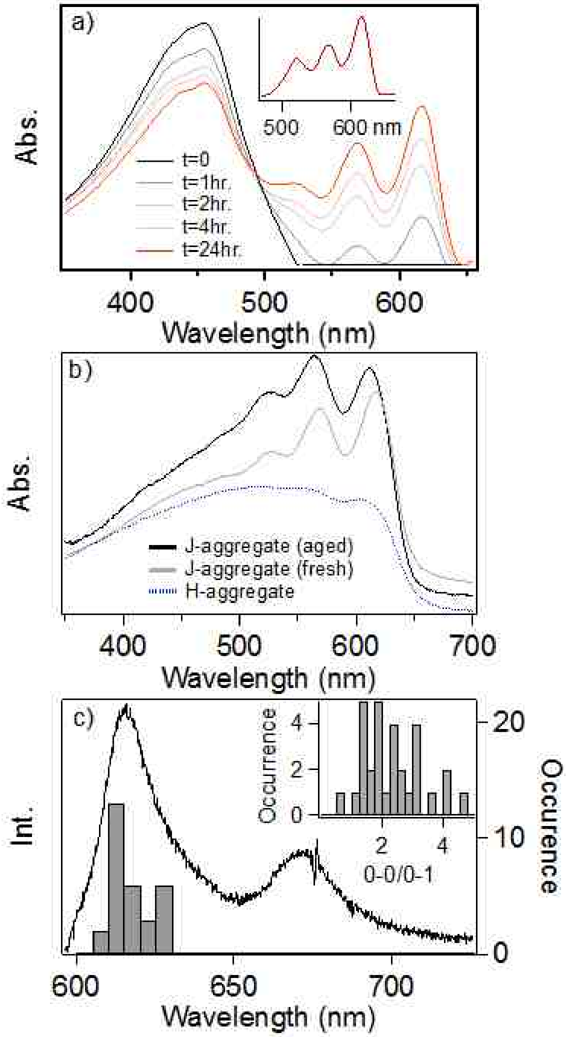

Figure 4.1 a) Time-dependent optical absorption spectra of P3HT J-aggregate nanofibers during self-assembly. Inset: Spectrum of isolated single chain aggregate. b)

Comparison of fresh and aged P3HT J-aggregates with H-aggregate nanofibers. c) Representative PL spectrum of a single J-aggregate and distributions of PL maxima (λ_{max}). Inset: Histogram of vibronic 0-0/0-1 ratios.

Examples of this behavior can be found in Figure 4.1b displaying representative absorption spectra of fresh (gray trace) and aged (black trace) J-aggregate nanofibers. For comparison, a typical H-aggregate nanofiber absorption spectrum is shown that was assembled in anisole, a non-solvent for P3HT at low temperatures that does not permit molecular weight fractionation of aggregated zones. In aged J-aggregate samples 0-0/0-1 absorption ratios are ~0.85 although vibronic linewidths increase slightly (~400 cm-1).

We previously attributed the loss of J-aggregate character in larger (older) nanofibers to the sensitivity to small structural perturbations that disturb the delicate interdependence between intra- and interchain exciton dipole-dipole coupling to structural order within the aggregate π-stack.[50] An alternative explanation stems from recent predictions by Spano and co-workers that considers the sign of the overlap of electron-hole wave functions which dominates in situations when Coulombic coupling vanishes due to large exciton coherence lengths.[47] Moreover, transformations between H- and J-like excitons are facilitated by interchain polaron pair, or, CT states, determined by the registry (i.e., lateral and longitudinal displacement) of P3HT monomers in the π-stack. Although the monomer registry in single P3HT J-aggregate chains clearly favors dominant intrachain exciton coupling, the larger amounts of these self-folded P3HT chains in aged J-aggregate nanofibers increases the likelihood of registry mismatch at chain-chain contacts. This scenario increases interchain or, H-aggregate, character via CT state intermediates that require sufficient delocalization of intrachain excitons in order to be populated.

The ability to delocalize excitons or polarons in conjugated organic macromolecules is primarily determined by the intrachain conformational order. The lack of torsional disorder in P3HT J-aggregates ensures that self-localization of excitons is almost completely suppressed. When these delocalized excitons encounter a chain-chain contact, one carrier can undergo interchain transfer leading to an inter-chain CT state. Cursory evidence of chain-chain contacts as CT sites can be observed from sonication or dilution of J-aggregate nanofibers in solvent or solid dispersions, respectively.[50] In both cases, J-aggregate character is recovered in absorption and emission spectra (see Supporting Information). Figure 4.1c shows a representative photoluminescence (PL) spectrum of an isolated J-aggregate P3HT chain from an aged sample diluted into a polystyrene host. The distributions of PL 0-0 maxima and 0-0/0-1 ratios are shown as a histogram for ~50 particles. The latter reflect the extent of intrachain delocalization with some particles appearing as ideal J-aggregates (0-0/0-1 > 4) with others more closely resembling H-aggregates (0-0/0-1 ~1) that also had much lower signal-to-noise ratios. Comparisons with time-dependent nano-fiber absorption spectra in Fig. 4.1a reveal consistent trends where a larger nanofibers possess greater interchain, H-like character. We now show that the combination of delocalized intrachain excitons and chain-chain contacts in J-aggregates can facilitate formation of triplet excitons on longer (>1 ns) time scales.

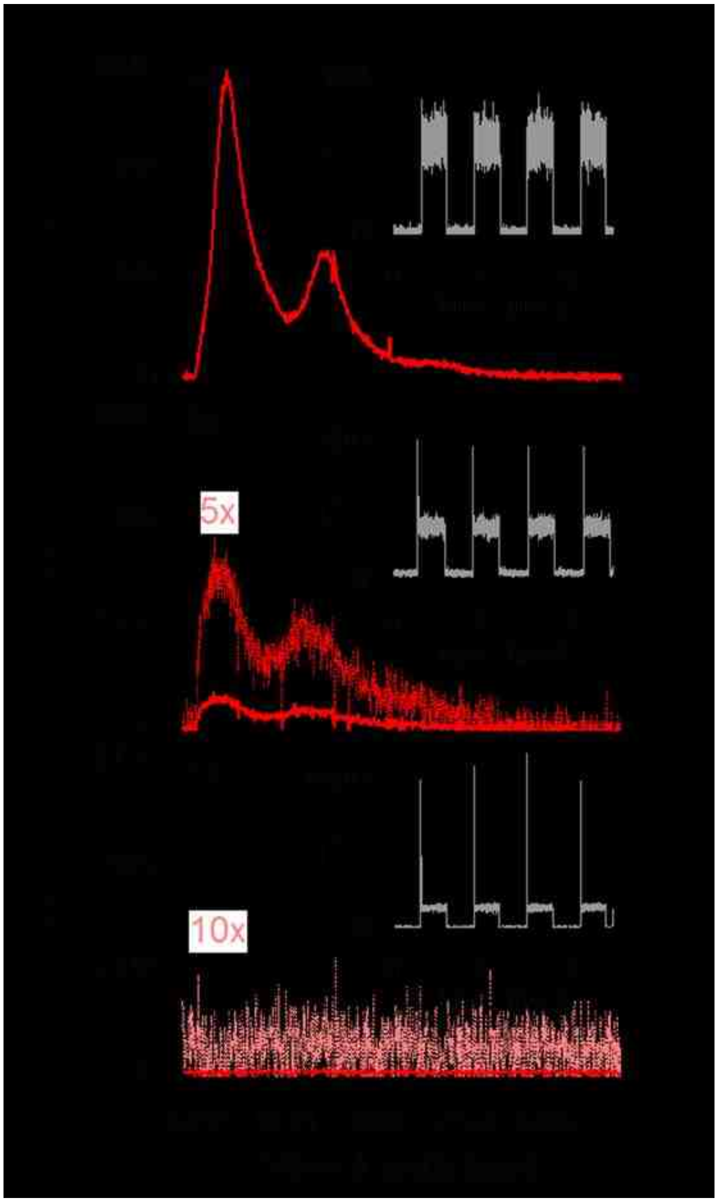
5x
10x

Figure 4.2 PL spectra and intensity modulated transients (insets) of P3HT J-aggregate nanofibers of varying size. a) Small, b) medium, and c) large nanofibers.

In an earlier study, we demonstrated efficient quenching of emissive singlet excitons by triplets in isolated P3HT J-aggregates using time-resolved, excitation intensity de-pendent PL modulation spectroscopy.[144] Briefly, when the excitation light turns on, only emissive singlet excitons are present, however, the prompt intensity (I_0) usually decreases rapidly (within ~1-10 μs) to a steady-state level (I_{SS}). PL quenching depths (I_0/I_{SS}) and decay time scales serve as proxies for triplet populations and singlet-triplet interactions, i.e., larger triplet levels lead to faster and more efficient PL quenching. These figures of merit also varied significantly from particle-to-particle and with excitation intensity consistent with expected size heterogeneity effects and photoinduced triplet generation, respectively. For ex-ample, I_0/I_{SS} typically vary from ~2–10 for excitation peak intensities of ~300 W/cm^2 and PL quenching kinetics and recovery were also comparable to measured triplet lifetimes in related systems.[93,110] Similar measurements on P3HT H-aggregate nanofibers and thin films (~10 nm) revealed much smaller triplet yields (I_0/I_{SS} <2) under the same excitation conditions.[144] We initially posited that larger triplet yields in J-aggregates originates from lower singlet-triplet exchange energy splitting because of expected larger intrachain electron-hole delocalization.[145] This scenario may result in larger intersystem crossing rate constants (k_{ISC}) provided there is a sufficient spin-orbit mixing be-tween singlet and triplet states.[116,117]

To further understand how J-aggregate packing and chain conformational characteristics within the π-stack influence triplet formation yields, we perform correlated PL and MCA spectroscopy size exclusion chromatography to investigate size-dependent triplet quenching. Figure 4.2 shows representative PL spectra and intensity modulated triplet quenching transients of a sampling of J-aggregates of different sizes acquired using a synchronously averaged pulsed excitation scheme described earlier. Here, I_0 represents the relative nanofiber size and, for smaller nanofibers (Fig. 4.2a), intensities typically reflect PL emission from as little as one single P3HT chain, which was confirmed separately from PL intensity transients measured in the presence of oxygen. It is also interesting to PL line shapes exhibit prominent J-aggregate character but triplet quenching of singlet excitons is very weak or non-existent (I_0/I_{SS} ~1). This result is surprising since earlier re-ports of singlet PL quenching by triplets was relatively efficient in single polymer chains.[100,110] Conversely, larger particles (Figs. 4.2b,c) show greater triplet quenching (I_0/I_{SS} >1) although PL spectra show substantial decreases in signal-to-noise and 0-0/0-1 intensity ratios.

The apparent loss of J-aggregate character and concomitant increase in triplet quenching in larger nanofibers is consistent with greater CT character in these structures. According to the wavefunction overlap model, it is possible for intrachain exictons with large coherence lengths to exhibit H-aggregate features in optical spectra due to offset in the registry between monomer units. We propose this registry mismatch at chain-contacts between self-folded J-type P3HT chains are likely structural origins of interchain CT states. However, it is important to stress that greater inter-chain character does not necessarily imply lower intrachain order. For example, the fact that triplet yields increase in larger NFs whereas P3HT H-aggregate nanofibers and thin films (i.e., aggregates with lower intra-chain order) show very low to nonexistent triplet yields due to predominant polaron generation[84,87,146] illustrates that increased interchain CT character merely expand relaxation pathways for intrachain excitons. Once a CT state is populated via inter-chain hole (electron) transfer, spin correlation is lost which, upon recombination of separated carriers at later times, can lead to triplet formation according to simple spin statistics.

Although triplet generation mediated by interchain CT states provides the most plausible explanation for size-dependent triplet PL quenching shown in Fig. 4.2, it is worth-while to first consider possible contributions from conventional perturbative triplet formation mechanisms, such as ISC. As an alternative to interchain CT states as triplet precursors, intrachain polaron pairs (PP) could potentially explain facile triplet formation in J-aggregates.[147,148] For example, large electron-hole separation (i.e., beyond the exchange radius) could diminish singlet-triplet exchange splitting to nearly degenerate levels, which then requires only a small amount of spin-orbit mixing to cross into the triplet manifold. However, the direct products of irreducible representations of orbital component of both singlet and triplet wavefunctions can only mix via the out-of-plane component of the spin-orbit operator assuming idealized C_{2h} point group symmetry. As previously noted by Beljonne et al., this scenario should result in negligible spin-orbit mixing.[117] Moreover, contributions from vibronic mechanisms are also expected to be ineffective in highly planarized conjugated organics, such as P3HT J-aggregates. We conclude that ISC mediated by PP states is probably not an efficient route for generating triplets in these structures despite expected reductions in singlet-triplet energy gaps.

Similar to intrachain PP states, identifying reliable inter-chain CT state signatures can be fraught with difficulty owing to their intrinsically low oscillator strengths (optical cross-sections). Spano and co-workers demonstrated, in the wavefunction overlap description, that CT states can mix with intrachain J-aggregate excitons due to symmetry. This feature should allow for detection of CT character using PL techniques that we further expect to exhibit size-dependent behavior, similar to triplet generation. Recently, Hu et al. found compelling evidence for CT states in close energetic proximity to the emissive singlet by varying the polarity of surrounding solvent medium.[149] These authors studied co-polymer derivatives and observed that PL emission yields decrease substantially in polar solvents because of stabilization of CT states below the emissive singlet exciton emission energy.[149] CT excited states have also been proposed to facilitate efficient conversion of singlet excitons into triplets via singlet fission although there is presently debate over the efficacies of this mechanism and the reliability of spectroscopic markers of intermediates (e.g., spinless triplet pairs).[150] Unfortunately, the accessible range of suitable solvents for dispersing P3HT J-aggregates is severely limited, which precludes similar solvent variation studies. Instead, we turn to alternative PL probes for elucidating the roles of CT states in exciton spin conversion processes in P3HT aggregates, namely, electric field-dependent time-resolved single molecule spectroscopy.

Application of electric fields has revealed interesting and novel phenomena in conjugated polymers as well as basic physical pictures of excitons and their properties. For example, Reufer et al. used electric-fields to induce exciton dissociation leading to polaron-pair type states that, once the field was turned off, recorrelation and recombination into either singlets or triplet states could be studied.[151] Related electroabsorption or electrofluorescence studies on various conjugated polymer thin films show linear and quadratic Stark effects that reflect changes in permanent dipoles and polarizabilities, respectively.[152–154] However, most cases involve heterogeneous bulk films with substantial disorder that manifests as inhomogeneous broadening and energy funneling to emissive traps, respectively. Electrical leakage can also be a factor in devices without blocking layers in addition to significant charge transfer interactions with electrodes. To avoid complications from charge movement and contact effects, P3HT aggregates are dispersed in polystyrene and cast into thin films on top of an indium tin oxide (ITO) coated glass coverslip with an additional layer of SiO2 (~50 nm) to block current flow when the device was biased. Similar measures were employed on the other electrode by depositing an additional layer of polystyrene without dispersed aggregates prior to thermal evaporation of a metal contact.

Figure 4.3a shows representative PL decays from H- and J-aggregate P3HT nanofibers within capacitor devices. Many decays were measured with no applied bias to assess the range of intrinsic PL decay kinetics. Both aggregate types exhibit biexponential decay signatures according to eq. 1 and Figures 3b,c displays fits obtained from the aver-age of many decays along with the averaged time constants and amplitudes for each component.

$$F(t) = \left[a_1 * \exp\left(-\frac{t}{\tau_1}\right)\ \right] + \left[a_2 * \exp\left(-\frac{t}{\tau_2}\right)\ \right]$$

H-aggregate P3HT nanofiber PL decays are dominated by the fast component, $\langle\tau_1\rangle = 200$ ps, representing over 80% of the total decay. P3HT J-aggregates have similar fast component time constants but much larger contributions from the slower decay component. It is also interesting to note that the slow decay time constant is significantly larger in J-aggregates than H-aggregates, $\langle\tau_2\rangle = 2.4$ ns vs. $\langle\tau_2\rangle = 1.4$ ns, respectively

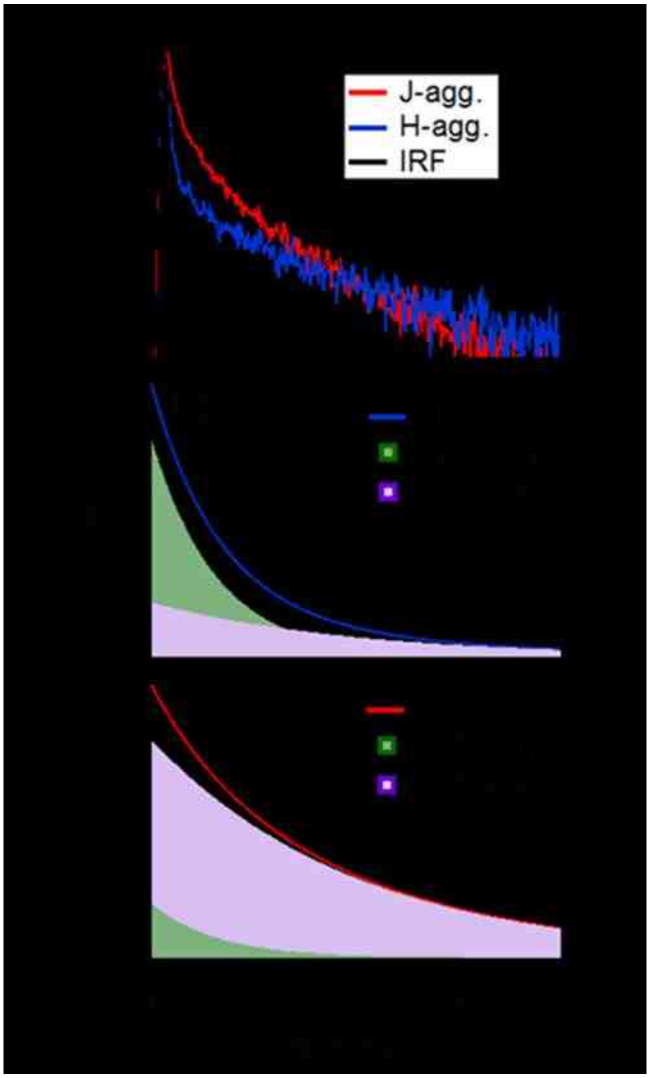

Figure 4.3 a) Representative PL decays of a single P3HT J-aggregate (red trace) and H-aggregate (blue trace) and the instrument response function (IRF). b), c). Fits and contributions of fast and slow PL decay components for averaged H- and J-aggregate PL decays, respectively.

Moreover, the fraction of the slow decay component decreases with increasing J-aggregate size suggesting greater H-aggregate character similar to trends in size-dependent optical spectra shown in Fig. 4.1. The origins of these components are still actively discussed which include, torsional relaxation, charge transfer and polymorphism.[155,156] Korovyanko et al. also noted that the non-radiative PL decay contribution is unlikely to be affected by aggregation[157] although it was probably unlikely that intrachain ordering effects could be discerned. It is widely believed that the fast component represents emission from the unrelaxed (distorted) emitter.[155] The fact that this component dominates decay characteristics in H-aggregate structures is consistent with their lower intrachain order and large Franck-Condon active torsional motions leading to rapid exciton localization and interchain character. Correspondingly, at zero bias, the greater fraction of the slow decay component in J-aggregates is consistent with their assignment as intrachain delocalized excitons. We propose the larger value of the slow decay component arises from substantial CT character as expected from theoretical predictions.[47] Application of electric fields can now be used to resolve this CT character.

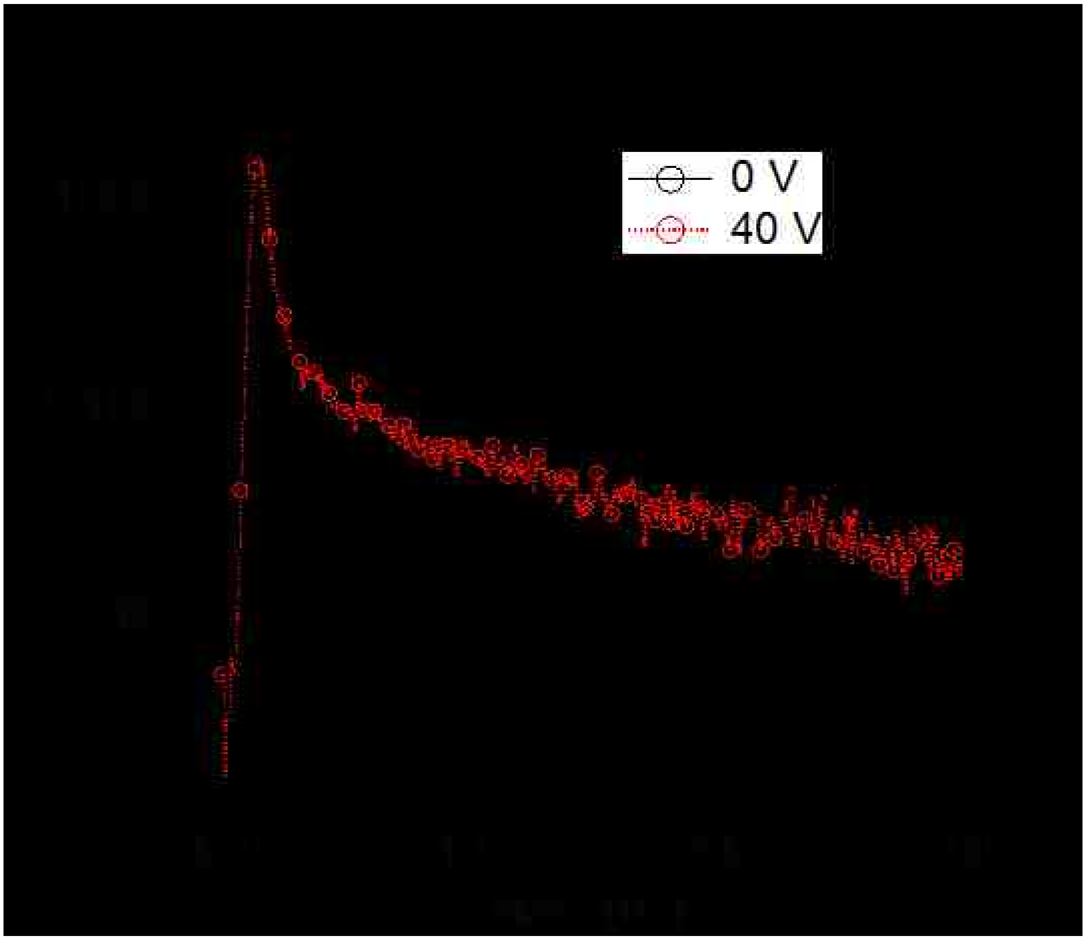

Figure 4.4 Typical PL decay response of an individual P3HT J-aggregate nanofiber with and without an applied electric field.

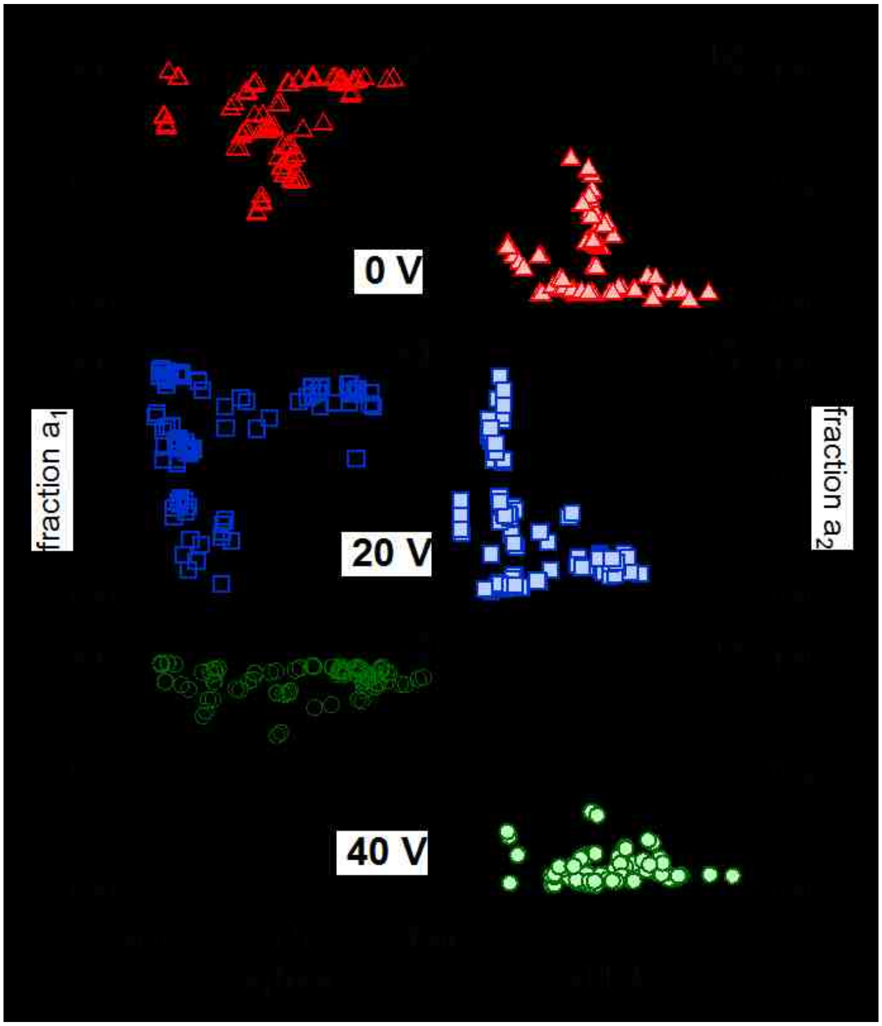

Figure 4.5 Scatter plots of the fast (open symbols; a, c, e) and slow (filled symbols; b, d, f) PL decay components of ~100 P3HT J-aggregate nanofibers with increasing electric field strength. Voltage bias levels (peak-to-peak) are shown for each data set.

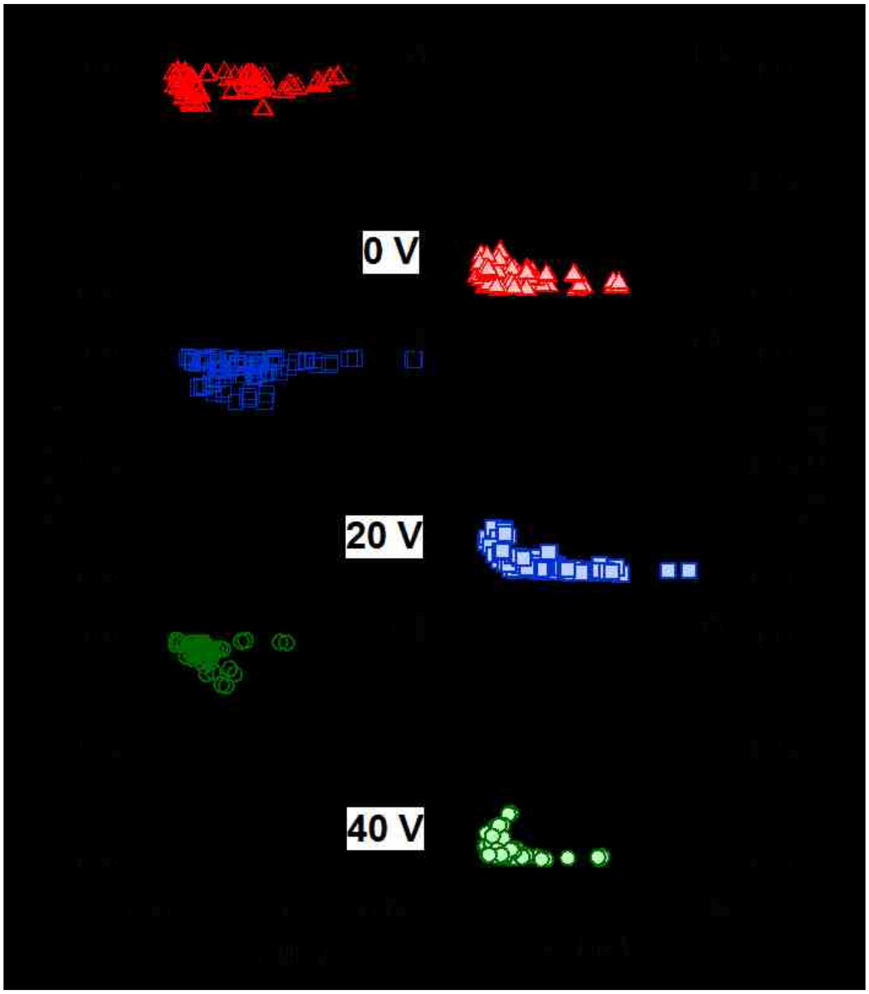

Figure 4.6 Scatter plots of the fast (open symbols; a, c, e) and slow (filled symbols; b, d, f) PL decay components of ~100 P3HT H-aggregate nanofibers with increasing electric field strength. Voltage bias levels (peak-to-peak) are shown for each data set.

Table 3. Average and standard deviations of the P3HT aggregate fast and slow PL decay time constants.

	H-aggregate		J-aggregate	
Voltage (p-p)	$\langle\tau_1\rangle$ (ns) a_1 (arb. units)	$\langle\tau_2\rangle$ (ns) a_2 (arb. units)	$\langle\tau_1\rangle$ (ns) a_1 (arb. units)	$\langle\tau_2\rangle$ (ns) a_2 (arb. units)
0 V	0.19±0.12	1.44±0.73	0.47±0.19	2.41±0.69
	0.93±0.04	0.073±0.04	0.68±0.16	0.31±0.17
20 V	0.25±0.11	1.98±0.91	0.27±0.25	1.31±0.88
	0.93±0.05	0.68±0.005	0.72±0.23	0.27±0.25
40 V	0.14±0.06	1.54±0.59	0.55±0.27	2.69±0.79
	0.94±0.05	0.061±0.05	0.91±0.06	0.085±0.06

The capacitor type model devices used here are biased up to ±20 V (40 V peak-to-peak) corresponding to a maximum electric field strength of ~106 V/m. A square voltage waveform (1 KHz) was used and emitted photons were routed into separate channels of the photon counting sys-tem to determine the directional dependence of the electric field response. It is useful to note that the disparity be-tween electric field modulation frequency and PL decay dynamics responses are sufficiently large implying a quasi-DC nature of the field. Nevertheless, our choice of AC applied electric fields minimizes unwanted contributions from permanent polarization of the dielectric medium (i.e., host matrix). Figure 4.4 shows representative electric field-dependent PL decay of a single P3HT J-aggregate with and without applied bias. Cursory inspection reveals that the relative amplitude contributions are most affected by applied electric fields indicating populations of emitting species are altered rather than intrinsic electron-hole recombination characteristics. Importantly, electric field-dependent PL responses (e.g., modulation depth and direction) varied considerably from particle-to-particle demonstrating that polarization and leakage effects were negligible. Figures 4.5 and 4.6 show scatter plots of both PL decay components (amplitude and time constant) of over 100 P3HT H- and J-aggregates each, respectively, with applied electric fields. On average, individual nanofiber PL decays recorded showed no dependence on the sign of the applied voltage bias. Approximately 10% of nanofibers exhibited different behaviors with positive and negative bias but these are most likely due to close proximity to the metal top contact. Because of the invariance with direction of the electric field, the responses recorded for positive and negative bias were averaged together in Figs. 4.5 and 4.6.

The most noteworthy feature observed over the entire range of electric field strengths was the large modulation of the slow PL decay component amplitude occurring almost exclusively in J-aggregates. A decrease of the slow decay time constant was observed at 20 V p-p for ~55% of the particles together with an increase of the amplitude although the average amplitude showed little change from 0 V. Corresponding electric field-dependent responses of H-aggregates shows very little modulation even up to 40 V p-p except for reductions of the fast and slow time constants by ~30%. Signal-to-noise levels at this electric field strength also diminish probably from enhanced electron-hole recombination. Interestingly, in J-aggregates, the slow decay component amplitude decreases drastically at this field strength with a much broader distribution of both fast and slow decay time constants. With the slow PL decay component now <10%, this behavior closely resembles H-aggregate PL decay characteristics at 0 V.

We conclude that the large perturbations of the slow PL decay component in P3HT J-aggregates results from significant admixture of CT character leading to greater polarizability (i.e., large excited state dipole moments). CT ad-mixture further explains the larger observed slow PL decay component in J-aggregates in the absence of an applied electric field. We further posit the larger exciton coherence lengths of the J-aggregate intrachain exciton enhances interactions with CT states. For example, using known exciton mobilities and measured lifetimes, exciton diffusion lengths are expected to range between ~5–10 nm in J-aggregate structures. This length scale ensures a greater likelihood of delocalized excitons encountering or, acquiring, CT character before recombining. The fact that larger nanofibers exhibit stronger electric field-dependent PL de-cay modulation is also consistent with the view that CT states are concentrated at chain-chain contacts or perhaps cis-type conformational defects that enable P3HT chains to fold into highly anisotropic (rod-like) structures.[78]

Earlier estimates of CT state energies in P3HT place these states ~0.5 eV above the lowest energy excited singlet exciton state.[32] The ability of the electric field to modulate the slow PL decay component of P3HT J-aggregates implies that the intrachain exciton already has acquired significant CT character before the emitter has completely relaxed. This suggests lower CT states energies in P3HT J-aggregates, which is plausible due to the delocalized nature of these systems. The loss of the slow decay component at large field strengths indicates a large decrease of the CT state energy probably due to field-induced dissociation. The anomalous decrease of the slow component decay time observed at 20 V p-p may reflect an electric field induced change in the non-radiative rate constant although the exact origins for such an effect are not completely clear at this time.

In light of electric field-dependent PL decay responses on shorter time scales, we consider the possibility that CT states could potentially cause PL quenching observed on slower time scales in addition to triplet quenching due to dissociation into free carriers. If this were the case, excitation intensity-dependent PL transients (e.g., Fig. 4.7) should exhibit a dependence on an applied electric field. To assess if appreciable CT state populations or free carriers exist on the time scales of triplet-induced PL quenching, we per-formed electric field-dependent intensity modulated single molecule spectroscopy –

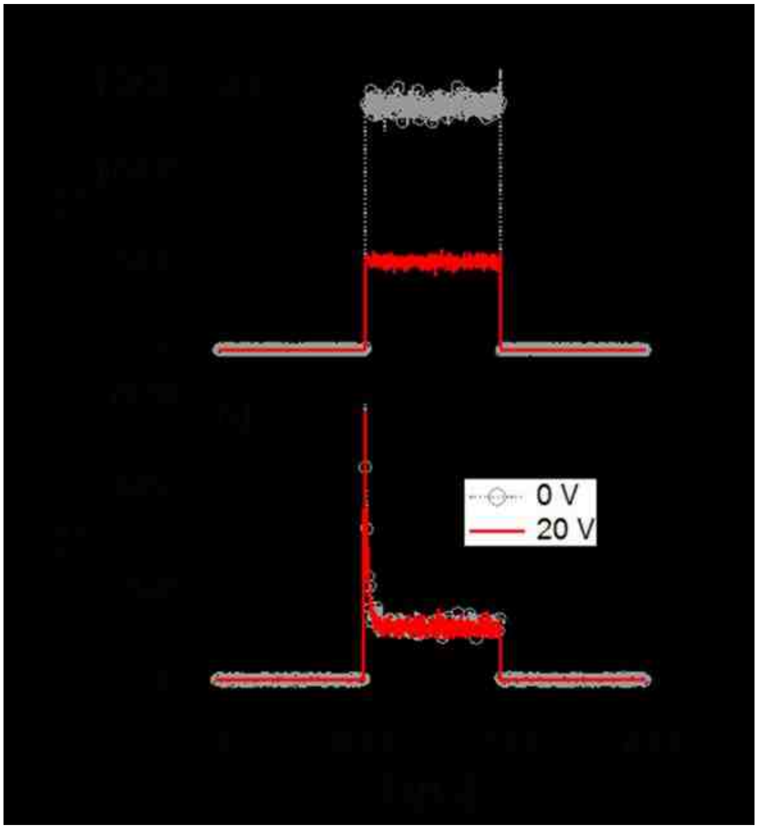

Figure 4.7 Representative intensity modulated PL transients of H-aggregate (a) and J-aggregate (b) P3HT nanofibers with and without applied voltage bias (electric field).

– on both H- and J-aggregate P3HT nanofibers. Figure 4.7 shows typical intensity modulated PL transients of H- and J-aggregates at 0 V and +20 V. DC voltage bias was applied to the capacitor devices in this experiment because of the longer averaging times required to generate sufficient signal-to-noise ratios. Separate experiments performed using negative polarity showed identical behaviors ruling out coupling of large dipole moments with the applied field as a likely origin of the observed responses. The majority of J-aggregate type nanofibers showed virtually no modulation of typical PL quenching responses with an applied electric field. This result demonstrates no appreciable CT character or free carrier levels present on longer time scales (>10 ns). Though H-aggregates do not show significant singlet PL quenching dynamics, we observed large – changes in steady-state PL intensities with applied electric fields. As noted earlier in transient absorption spectroscopy studies of P3HT thin films, only polaronic signatures are apparent on time scales investigated here with no evidence of triplets.11, 43, 45, 55, 57 Together with electric field-dependent PL decays, these results demonstrate that CT states do not persist on long time scales and have either recombined to a singlet or triplet exciton or decayed non-radiatively back to the ground electronic state.

4.3 Conclusions:

Size- and electric field-dependent PL spectroscopy of isolated P3HT H- and J-aggregate nanofibers has revealed the presence of intermediate CT states that direct photophysical outcomes over a broad time range. We demonstrate that the presence of

CT states can only be elucidated in nanostructures of high purity due to suppression of disorder (torsional) induced exciton localization. By shelving carriers in interchain CT states, recombination of separated carriers at later times favors triplet exciton formation, which are manifest in J-aggregates. Similar to earlier time-resolved spectroscopy studies in P3HT thin films, H-aggregates only exhibit signatures consistent with polaronic species as evidenced by electric field-dependent PL transients on longer time scales.

Our study demonstrates the crucial role of structure (con-formation and packing) and ordering on the eventual fate of primary photoexcitations in polymer aggregates. While disorder-induced exciton localization between polymer stems in π-stacks of H-aggregates promotes interchain character leading to polaron formation, J aggregates only acquire this type of interchain wavefunction overlap if sufficient interchain contact sites exist. Shelving carriers in these interchain CT sites causes loss of spin correlation which, upon recombination at later times, should favor preferential triplet state formation followed by slow non-radiative recombination back to the ground electronic state in addition to interacting with, and deactivating nearby emissive singlets. The fact that the majority of intrachain excitons on the P3HT stems in J-aggregates are electronically isolated from each other due to a lack of both dipole-dipole coupling and improper symmetry for significant interchain exciton character, creates a unique scenario by which CT mediated triplet formation pathways can be ex-posed. We stress that this mechanism is only manifest in cases where exciton localization effects are minimized by selective control of aggregate forming polymer chains.

Chapter V

Polythienylene−Vinylene Structure−Function Correlations Revealed from Resonance Raman Spectroscopy and Photocurrent Imaging

5.1 Introduction

Solar cells based on conjugated polymer donor and fullerene acceptor blends have demonstrated enormous potential as candidates for efficient and inexpensive alternative energy resources[108,158–160]. Despite large improvements in device performance and lifetime, there is still room for improvement since power conversion efficiencies are often well below theoretical limits. Ideally, there should be minimal losses of the incident photon energy; however, efficient non-radiative excited state deactivation channels involve high-frequency (fast) backbone skeletal vibrational motions promoting rapid energy dissipation[161]. These processes take place on time scales < 100 fs; thus, charge separation of neutral, singlet excitons must occur on comparable or faster time scales[162,163]. Recent studies have demonstrated the importance of fullerene crystallites in facilitating ultrafast charge separation before polymer exciton relaxation takes place[164]. This mechanism requires substantial coupling between high-energy singlet exciton states and charge separated states[161], which is ultimately dictated by blend nanomorphology (e.g., polymer−fullerene miscibility and crystallinity). Charge separation yields may also be improved by extending the lifetimes of polymer excitons to ensure these bound states reach a fullerene interface before relaxing (radiatively or non-radiatively) back to the ground electronic state. This scenario is realized when singlet excitons spontaneously convert into spin-forbidden, triplet excitons with substantially longer lifetimes than their singlet counterparts[107]. Singlet−triplet intersystem crossing is usually not efficient in conjugated organic molecules; however, singlet fission has received increased attention for splitting a singlet exciton into two triplets on ultrafast time scales[115]. This process has been reported mostly in conjugated acenes, although recent studies have observed singlet fission in –

Scheme 1. Synthesis Route of P3ATV

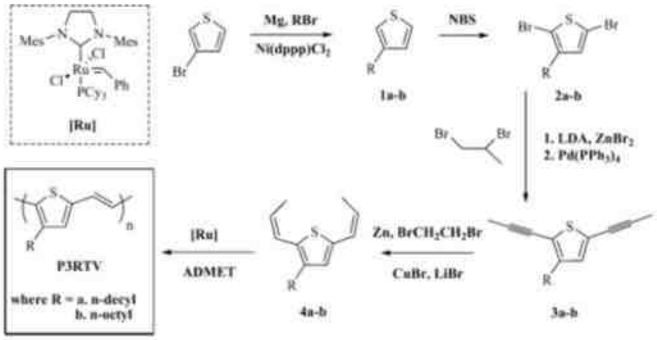

Figure 5.1 Synthetic scheme detailing formation of PTVs used in these experiments.

–polythiophene systems[87,165]. Interestingly, efficient singlet fission was demonstrated in dilute solutions of a poly(3-alkyl-thienylenevinylene) (P3ATV) derivative which has significant implications for potentially utilizing triplets before they relax back to the ground electronic state[165]. Harvesting triplet byproducts of singlet fission has also been proposed to increase charge generation yields[166], but it is less clear how singlet fission yields will be affected by the complex morphological landscape of photovoltaic polymer/fullerene blends in addition to the intrinsic conformational heterogeneity of polymers.

We use resonance Raman spectroscopy to study the extent of excited state geometric rearrangements and their dependence on the packing characteristics of two P3ATV molecules. Resonance Raman intensities are particularly sensitive to vibrations displaced in the initial allowed ^{1}Bu excited state and the local environment of the resonant chromophore. Previous photophysical studies of related P3ATV derivatives noted ultrafast relaxation to a low-lying dipole forbidden ^{2}Ag excited state resulting in nearly quantitative fluorescence emission quenching[167]. Musser et al. recently amended this interpretation by demonstrating that population of the ^2A_g excited state in P3ATV solutions occurs from efficient intramolecular singlet fission on sub-100 fs time scales[165].

Although resonance Raman spectroscopy does not permit direct investigations of the ultrafast relaxation dynamics and optically forbidden (dark) excited states, it is possible to obtain detailed views of vibrational mode-specific geometrical displacements involving the initial “gateway” excited state in singlet fission. Moreover, excitation wavelength-dependent Raman frequencies and intensities reveal contributions from distinct structural forms that are usually masked in absorption spectra but nonetheless have a profound impact on photophysics and material performance.

P3ATV Raman spectra display well-resolved progressions of overtone and combination bands involving multiple high frequency backbone symmetric stretching vibrations (~1200−1600 cm^{-1}) indicating a significantly distorted geometry change between the ^1A_g ground state and the ^1B_u excited state. Raman excitation profiles and frequency dispersion were next measured by varying laser excitation energy across the $^1A_g \rightarrow {}^1B_u$ absorption line shape that show larger enhancements near the red absorption edge and larger variation of Franck−Condon active P3ATV CC vibrational frequencies across the absorption envelope, respectively. We show these behaviors can be explained by excitation of aggregated and amorphous P3ATV chains with distinct optical and Raman line shapes. Similar behaviors have been reported in other polythiophene systems, and this assignment is also supported by reports of polymorphism in related P3ATVs (i.e., two distinct P3ATV phases with different packing characteristics)[168].

Raman intensities were simulated by calculating the time dependent Raman cross-correlation function for each displaced vibration that enabled estimates of mode-specific vibrational displacements in the excited state. These parameters were then used to simulate one-photon absorption spectra that showed excellent agreement with experimental P3ATV absorption spectra in the region where aggregates typically absorb. Subtracting simulated and experimental absorption spectra exposed a higher energy, weaker, and broadened absorption transition assigned to absorption of amorphous P3ATV chains. In a similar fashion, the characteristic Raman pattern of the amorphous component was elucidated by exciting P3ATV absorption spectra with post-resonant excitation and comparing to line shapes generated using pre-resonant excitation that preferentially selects only the aggregated component. The latter tend to dominate line shapes due to additional resonance enhancement effects, especially with longer (lower) wavelength (energy) excitation.

Functioning solar cell devices were next fabricated by blending P3ATVs with a soluble fullerene derivative to promote photoinduced charge transfer. Despite their lower energy absorption transitions and tendency to aggregate, P3ATVs have so far seen limited use in solar cells mainly owing to relatively poor power conversion efficiencies (PCE)[169–172]. Non-ideal interface morphologies have been suggested as the chief origin of low PCEs and poor charge generation efficiency. However, detailed morphological studies and direct correlations to performance in device environments have been lacking. We apply our model to P3ATV solar cells using resonance Raman spectroscopic and photocurrent imaging to spatially map morphology-dependent structure to material performance. In situ maps of aggregated and amorphous P3ATV fractions were constructed revealing new microscopic views of polymer/ fullerene interactions that can be directly correlated to local photocurrent yields. Unlike other aggregating polymers, addition of fullerenes does not disturb P3ATV aggregate amounts and packing characteristics. However, larger photocurrent production was observed in aggregated regions with greater fullerene content (i.e., lower P3ATV Raman intensities) than corresponding amorphous regions. Greater demixing was observed in the amorphous P3ATV fraction (i.e., higher P3ATV Raman intensities), resulting in photocurrent decreases presumably due to poor charge generation yields.

Our results have exposed not only the underlying spectroscopic signatures of aggregated and amorphous P3ATV structures but also important details of the vibrational mode-specific geometrical rearrangements incurred in the allowed ^1B_u excited state. The latter may help shed light on the roles of high-frequency displaced vibrations in mediating early excited state relaxation processes. The relative insensitivity of each P3ATV fraction to the addition of fullerenes indicates weak interactions with the polymer-conjugated backbones, although these acceptors are probably more miscible with alkyl side groups. We propose that careful choice of side group substitution may enable reliable control of P3ATV packing and more favorable interactions with fullerenes to tune photophysics as well as device performance.

5.2 Results and Discussion

Figure 5.2 shows optical absorption spectra of P3DTV and P3OTV in solution and thin films. Both samples show a resolved vibronic progression interval of ~1450 cm^{-1}, and–

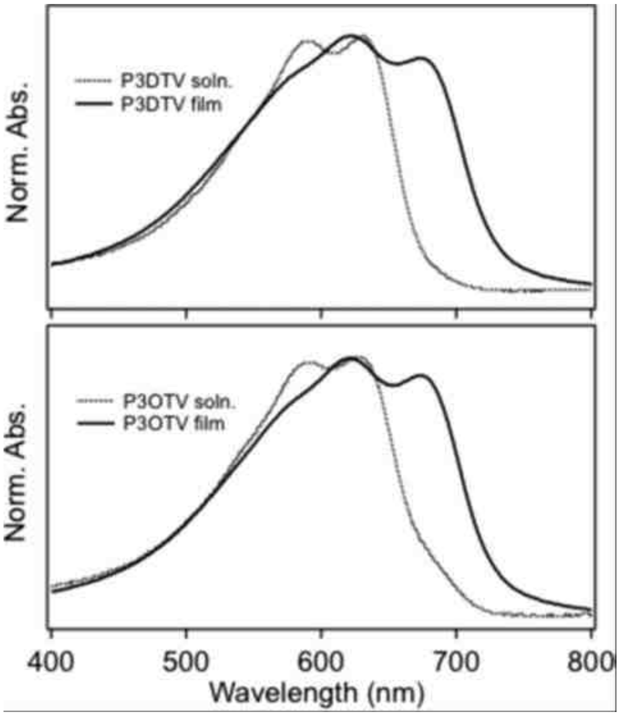

Figure 5.2 Absorption spectra of P3DTV (top) and P3OTV (bottom) solutions and thin films.

–the lowest energy transition (i.e., electronic origin, 0−0) absorption strength varies significantly between solution and solid phases, but vibronic intervals are similar. The overall P3ATV absorption line shape profile closely resembles those from ordered. (aggregating) polythiophenes[83]. The persistence of resolved vibronic structure in dilute solution suggests that P3ATV chains exist in collapsed conformations, which may correspond to aggregate seed precursors.

This conformation is also consistent with observations of singlet fission in dilute solutions that require polymer chromophoric segments to be in close proximity (i.e., significant interchain interactions) and possess suitable orientations[165]. In thin films, aggregates are more developed and exciton coupling is expected to be interchain in nature[168], similar to most polythiophenes[82,173], although packing distances differ from current benchmarks (e.g., regioregular poly(3-hexylthiophene)).

X-ray crystallography studies were next performed on P3ATV powders and thin films to further explore the nature of chain packing in aggregates. XRD data are shown in Figure 5.3 for powders and thin films of P3DTV and P3OTV. Both P3ATV derivatives have similar patterns in both powder and thin film forms. Three scattering peaks positioned at 2θ values of 5.4°, 10.9°, and 16.4° are observed for P3DTV, corresponding, respectively, to the lamellar (100), (200), and (300) scattering and a d spacing of ca. 16.4 Å. This lamellar spacing is comparable with those reported for P3HT and shorter than the end-to-end distances of two stretched n-decyl groups, thus indicating intercalation of the side chains in the solid state. intercalation between adjacent polymer chains. A relatively sharp peak at 2θ of 21.3° is also observed for the P3OTV powder, corresponding to a d spacing of ca. 4.2 Å. We tentatively assign this scattering peak to originate from π−π stacking Similarly, three lamellar peaks at 2θ of 6.3° (100), 12.8° (200), and 19.3° (300) are observed for P3OTV, corresponding to a d spacing of ca. 14 Å that indicates side chain, which is larger than that observed for P3HT ($d_{\pi-\pi}$ =3.7 Å). This increase is presumably caused by the intercalation of the alkyl side chains and/or more backbone flexibility imparted by the main-chain double bonds

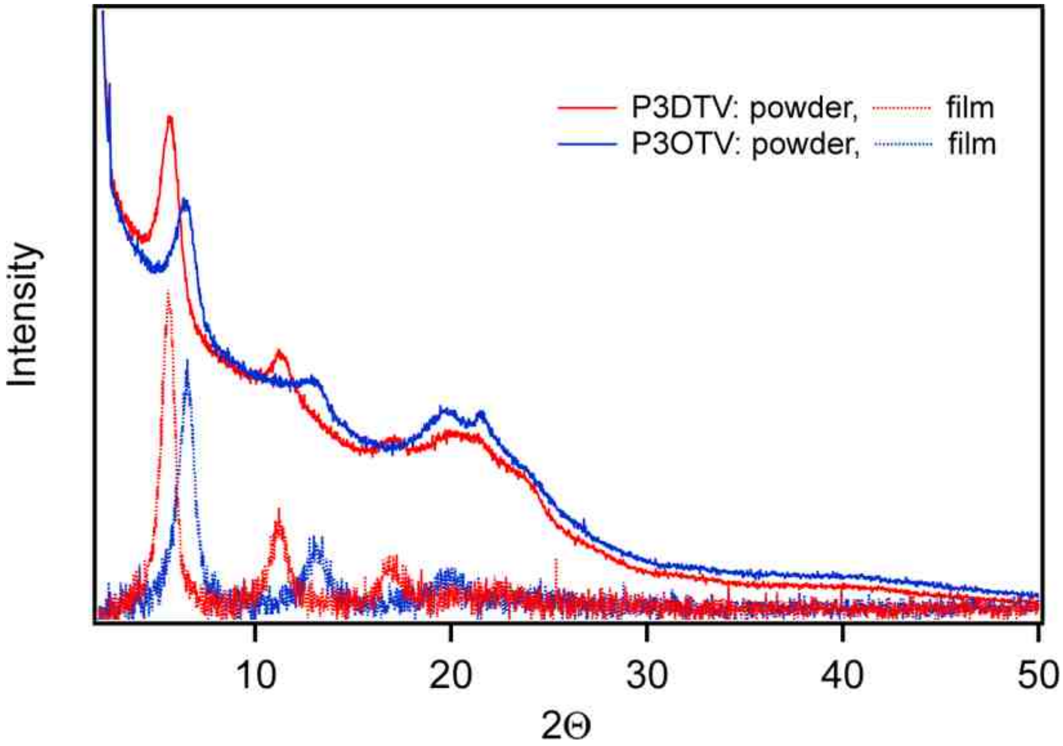

Figure 5.3 Powder and thin film XRD spectra of P3OTV and P3DTV.

A comparison of the XRD results with the absorption trends in Figure 5.2 points to a large aggregated fraction in both P3ATV derivatives that dominates the overall absorption line shape. The slightly larger interlamellar spacings in P3DTV do not appear to significantly impact exciton characteristics compared to P3OTV. Absorption line shapes also appear qualitatively similar to P3HT aggregates near the low-energy onset region, but the larger π−π stacking distances suggest weaker exciton couplings than found in P3HT. Despite the prevalence of aggregates in absorption spectra and X-ray data, intrinsic polydispersity effects usually dictate that not all polymer chains adopt the same ordered conformations, leading to polymorphs as well as minority fractions of amorphous (unaggregated) chains. Spectroscopic contributions of unaggregated chains are typically broadened and blue-shifted transitions, and their relative amounts are usually strongly dependent on processing conditions[83]. A key goal of our study is to identify spectroscopic contributions of underlying P3ATV aggregate and amorphous components and determine how these distinct structures affect material performance in device environments with complex morphologies. Furthermore, we will examine the extent to which specific vibrational modes couple to excitations and displace in the initial excited relative to their ground state equilibrium ground state geometry.

While useful, absorptive spectroscopies offer relatively limited views of aggregation, polymorphism, and excited state vibrational rearrangements mostly due to inhomogeneous broadening effects leading to line shapes with poorly resolved vibronic features. We instead turn to resonance Raman spectroscopy to examine Franck−Condon active vibrations by selectively exciting across the allowed $^1A_g \rightarrow {}^1B_u$ absorption transition line shape (Figure 5.2). Resonance excitation often produces large enhancements of Raman-active modes displaced in the excited state, and intensities are sensitive to the local environment of the chromophore. These features, along with sharp spectral line widths, make resonance Raman spectroscopy ideal for unmasking contributions from distinct structural subspecies that are usually masked by overlapping and broadened transitions in absorption spectra.

Figure 5.4a shows representative resonance Raman spectra of P3DTV thin films excited with 488 nm light corresponding to the high-energy tail of the absorption spectrum. Raman line shapes of both P3ATV derivatives were virtually identical, similar to one-photon absorption spectra (Figure 5.2), confirming the similar nature of chromophore segments despite minor variations in packing distances. Multiple overtone/ combination band progressions are resolved involving the C−C and C=C symmetric stretching vibrations of the P3DTV backbone (see Table 1). These features indicate a significantly distorted excited state geometry along multiple vibrational coordinates.

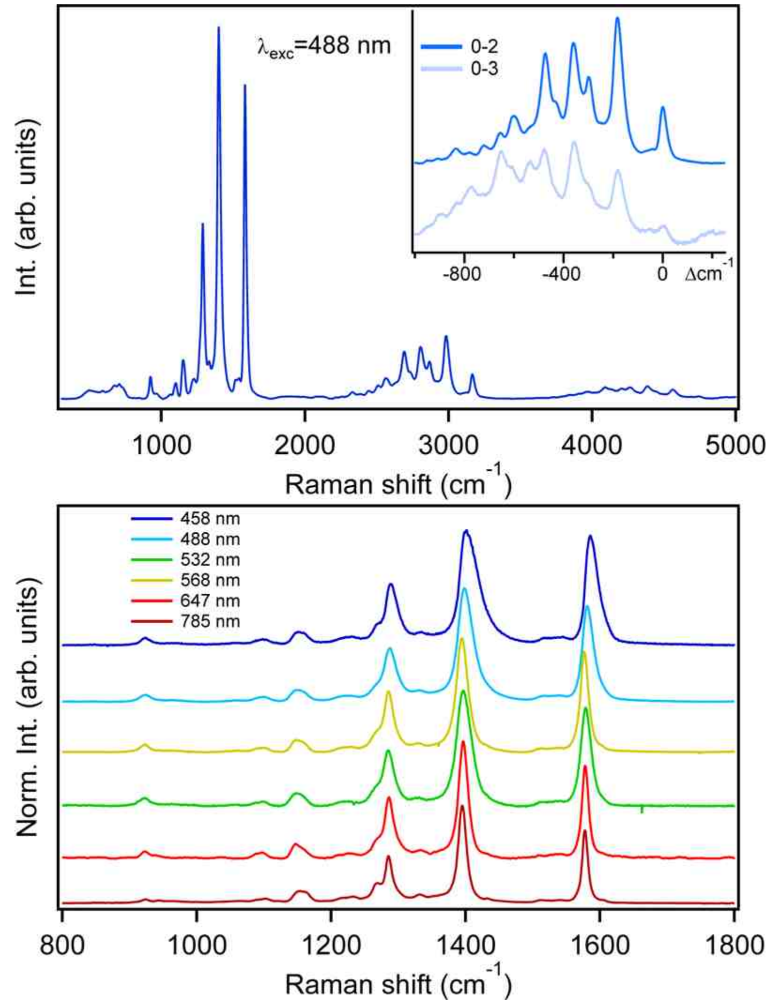

Figure 5.4 Resonance Raman spectrum of P3DTV (λ_{exc} = 488 nm) showing **m**ultiple resolved progressions of overtone and combination bands (top). Comparison of Raman line shapes as a function of excitation wavelength (bottom).

Table 1 Experimental P3ATV Raman Vibrational Modes and Assignments and Calculated Displacements

mode (k)	frequency (cm−1)	Δk (dimensionless)[a]	assignment[b]
ν2	664	0.21	thienylene ring C−H wag
ν3	913	0.27	vinyl C−H out-of-plane wag
ν4	953	0.27	vinyl bend
ν5	1047	0.2	thienylene C−H bend
ν6	1088	0.2	inter-ring C−C breathing modes
ν7	1143	0.51	
ν8	1210	0.24	
ν9	1278	0.67	vinyl C−H bend
ν10	1390	0.87	thienylene ring C=C stretch
ν11	1573	0.67	vinyl C=C stretch

first overtone/combination region	
ν3 + ν10	2315
ν7 + ν9	2430
ν6 + ν10	2490
2ν9	2555
ν9 + ν10	2680
2ν10	2790
ν9 +ν11	2855
ν10 +ν11	2970
2ν11	3155

[a] From time-dependent simulations of the Raman cross-correlation overlap function. $\Gamma = 380\ \text{cm}^{-1}$; $E_{0-0} = 14\ 700\ \text{cm}^{-1}$. [b] Reference [174].

We next evaluated the effect of excitation wavelength (energy) on the Raman line shapes, and Figure 5.4b displays the fundamental region of P3DTV thin films. As excitation wavelengths decrease, line widths broaden on the blue edge of the prominent, higher frequency thienelyene and vinylene C=C stretching modes (1390 cm^{-1}, ν_{10}, and 1573 cm^{-1}, ν_{11}) and apparent blue shifts of frequencies up to ~15 cm^{-1} were observed. P3ATV Raman spectra were next measured with 780 nm light, which is pre-resonant with the main absorption line shape (Figure 5.2) and should interrogate only longer chromophore segments. Comparison of pre- and post-resonant Raman line shapes (e.g., 780 vs 458 nm excitation) reveals stark differences in line widths, frequencies, and intensities, although patterns are similar, i.e., overtone/ combination transitions are still resolved with pre-resonant excitation and no new transitions are present. This indicates resonance enhancements are derived solely from the allowed ^1B_u excited state[174,175], but the large variation in line widths and frequencies is suggestive of selective excitation of structurally distinct P3ATV chains with different absorptivity coefficients and concentrations. We reported similar behavior in well-studied polythiophenes and polythienophenes where Raman signatures vary strongly with choice of excitation wavelength and material processing conditions[176]. Previous spectroscopic and theoretical studies of a related P3ATV derivative also noted the presence of two distinct geometrical phases differing in interchain stacking distance[168].

In addition, the near quantitative fluorescence quenching in P3ATVs by rapid relaxation to the dark ^2A_g excited state may have implications for Raman scattering when excitation is resonant with the allowed ^1B_u state. For example, Ozaki et al. observed larger frequency dispersion for P3ATVs compared to common light-emitting polymers and attributed this behavior to the presence of A_g excited states in close proximity with allowed ^1B_u states[175]. Unfortunately, it is not possible to directly probe these states with Raman, and attempts to measure their absorption spectra (e.g., by increasing sample concentrations) proved ineffective. To help sort out contributions from either conformational polymorphs or dark excited states, we examine excitation wavelength-dependent Raman intensities and frequencies. Raman frequency dispersion plots for both P3ATV derivatives were generated using the method described in ref 102 that takes the product of the squares of scaled frequencies. We consider only the dominant progression forming P3ATV backbone vibrations ($\nu 9 - 11$), and plots were scaled using the frequencies obtained from pre-resonance excitation, ω_0 (i.e., 780 nm excitation), corresponding to excitation of the lowest energy chromophores (longest conjugation length). Frequency dispersion plots are shown in Figure 5.6, and comparisons to previously published results from related P3ATV derivatives measured over the same excitation wavelength (energy) range reveal similar trends[175].

In addition to excitation dependent vibrational frequencies, Raman excitation profiles measure the intensity of a specific band as a function of excitation wavelength and are capable of exposing underlying excited states contributing to Raman scattering. In the case of overlapping and couple excited states, Raman profiles usually exhibit anomalous behavior (e.g., de-enhancements) from interference effects[177,178]. These may be apparent from comparisons with absorption spectra in the form of dips or non-constant vibronic intervals and non-Poissonian envelopes. Figure 8 shows experimental resonance excitation profiles of P3DTV for the $\nu 9-\nu 11$ fundamental and overtone transitions generated by using an external intensity standard (sapphire). P3OTV excitation profiles show nearly identical behavior and but are not shown here. Herein we display representative spectroscopic data for either P3ATV derivative for brevity due to their nearly identical features and behavior.

Relative Raman cross sections of $\nu 9-\nu 11$ fundamentals are smaller for shorter excitation wavelengths and then increase substantially at longer excitation wavelengths. Raman first overtone profiles show similar patterns across the P3ATV main absorption envelope but deviate from fundamental profiles probably from their different time evolution characteristics[179,180]. Enhanced activity near the red absorption edge is apparent and suggests either enhanced contributions from aggregates, consistent with the weakly resolved vibronic features in the low-energy region of the absorption spectrum (Figure 5.1) or possibly interference from dark (A_g) excited states on the high energy absorption tail. Similar Raman enhancements from π-stacked polymer aggregates have been demonstrated in P3HT and confirmed by varying processing conditions (i.e., aggregate content)[181]. McHale and co-workers also reported detailed resonance Raman data from molecular nanoaggregates and described a secondary resonance enhancement effect from these structures[182].

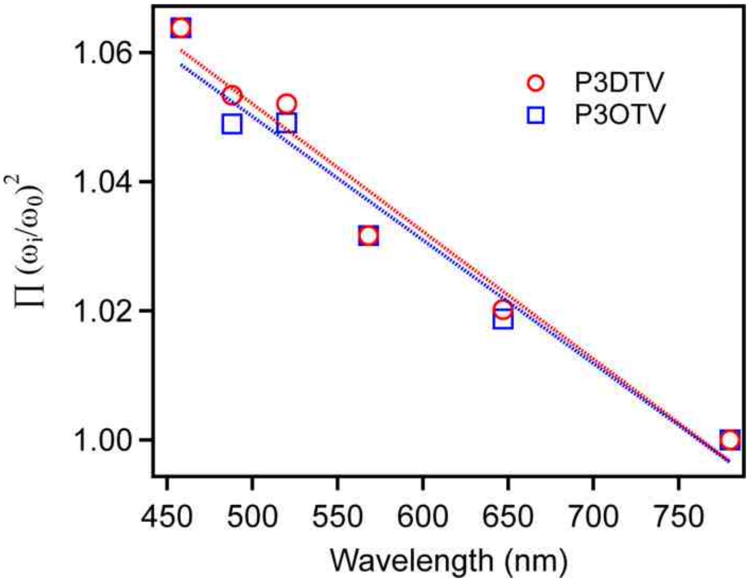

Figure 5.5 Raman dispersion plots for P3DTV and P3OTV thin films.

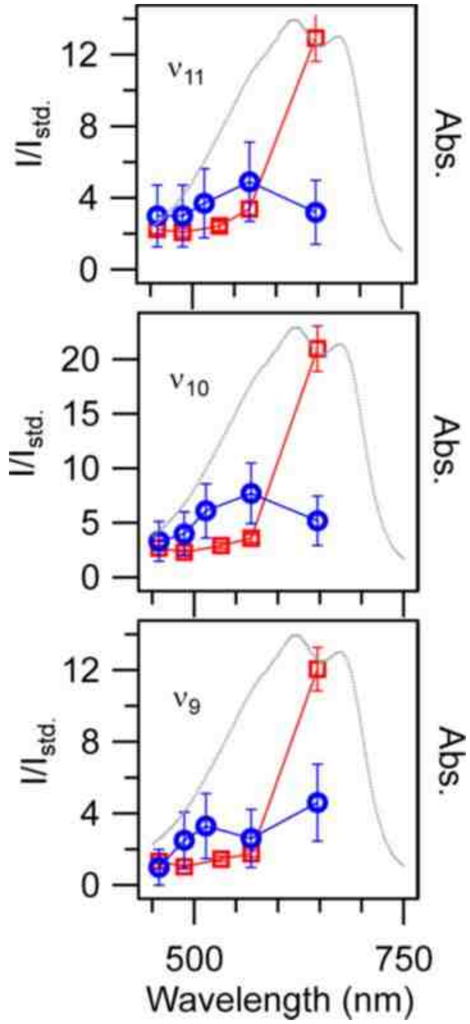

Figure 5.6 Raman excitation profiles for P3OTV thin film main skeletal vibrations (ν9−ν11). Fundamentals (0−1, red open squares) and first overtones (0−2, blue open circles) are shown. Thin film absorption spectra are shown for comparison.

Excitation wavelength-dependent Raman intensities and frequency dispersion behavior in Figures 5.5 and 5.6 are characteristic of selective excitation of structurally distinct P3ATV chains as opposed to previously proposed interactions with dark excited states. In this picture, aggregated P3ATV chains absorb in the lower energy (longer wavelength) region and, based on absorption and X-ray data, represent the dominant structural form in thin films. Conversely, amorphous (unaggregated) chains tend to absorb at higher energies (shorter wavelength) and correspond to minority species with shorter conjugated segments due to disorder. Discerning spectral line shapes of P3ATV structures can be accomplished by analyzing Raman line shapes generated on resonance with electronic absorption transitions from either structural form. We now use time-dependent wavepacket simulations to calculate Raman intensities and absorption spectra that, in addition to extracting mode-specific excited state geometrical rearrangements, provide a basis for discerning line shape contributions from aggregated and amorphous P3ATV chains.

5.3 Time-Dependent Raman Intensity and Absorption Simulations.

We first calculate the time-dependent Raman cross-correlation function for each displaced P3ATV vibrational mode using the framework developed by Heller and coworkers[179,180]. The model assumes that both ground and excited electronic states are undistorted harmonic potentials, and the transition dipole is not dependent on vibrational coordinates. In this limit, the cross-correlation overlap function can be calculated analytically for fundamentals and overtones as well as combination band transitions involving up to 3 modes. The total time-dependent overlap is given in eq. 1, which is the product of overlaps from each displaced mode.

$$\langle \phi_f | \phi(t) \rangle = \prod_k \left\{ \exp\left[-\frac{\Delta_k^2}{2}\left(1 - \exp(-i\omega_k t)\right) - \frac{i\omega_k t}{2} \right] \times \ldots \left(1 - \exp(-i\omega_k t)\right)^{n_k} \times \frac{(-1)^{n_k} {\Delta_k}^{n_k}}{(2^{n_k} n_k!)^{1/2}} \right\} \quad (1)$$

The parameters Δ_k and n_k are the displacement and order of the kth vibrational mode. The Raman polarizability, α, and intensities are obtained by a half Fourier transform of the cross correlation overlap

$$[\alpha_{fi}] = \frac{i}{\hbar} \int_0^\infty \langle \phi_f | \phi(t) \rangle \times \exp\{ i(\omega_k + \omega_l)t - (E_{0-0} + \Gamma)t \} \mathrm{d}t \quad (2)$$

$$I_{i-f} \propto \omega_l \omega_k^3 [\alpha_{fi}]^* [\alpha_{fi}] \quad (3)$$

The zero-point vibrational frequencies, ω_k, and energy of the electronic origin, E_{0-0}, are obtained directly from experimental Raman and absorption spectra and held constant. The fitting procedure entails adjusting vibrational displacements, Δ_k, at a constant incident excitation frequency, ωI, until good agreement between experimental and calculated intensities is obtained. Γ is a phenomenological damping factor that attenuates the overlap amplitude and, when excited on resonance, represents the characteristic lifetime of the chromophore (including coupling to the surrounding medium). In the following we briefly discuss the physical implications of these parameters, and additional details of the model can be found in refs 107 and 108.

Figure 5.7a shows simulated Raman intensities from the time-dependent wavepacket model and experiment, and best-fit parameter values are listed in Table 1

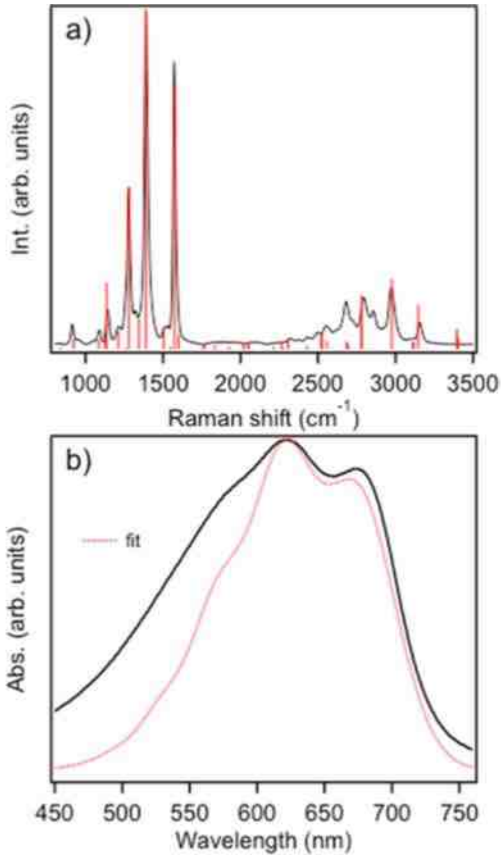

Figure 5.7 (a) Comparison of simulated (red sticks) and experimental (black) P3ATV Raman intensities (λ_{exc} = 488 nm). Fit parameters are provided in Table 1. (b) Simulated (red dotted trace) and experimental (black solid trace) absorption spectra.

Overall, the fits reproduce relative experimental intensities including overtones and combination bands. It is interesting to note that several weak combination bands involving lower frequency backbone bending vibrations appear in the vicinity of the dominant CC stretches, similar to experiment. The good correspondence between theory and experiment indicates that the actual potential energy surfaces are not significantly distorted from the ideal harmonic oscillator approximation used here.

We now use the same parameters to simulate the one-photon absorption spectrum (Figure 5.7b), which not only serves as an independent check on fitted parameters (i.e., Δ_k and Γ) but also reveals potential contributions from other states and structural forms. The simulated absorption spectrum exhibits a weakly resolved vibronic progression similar to experiment with excellent agreement near the band maximum and low-energy onset. We assign this region as absorption of P3ATV aggregates. The discrepancy between the fit and the high energy tail of the experimental absorption spectrum is — based on our earlier studies with P3HT — indicative of absorption contributions from shorter, less-ordered (unaggregated) P3ATV segments that represent the amorphous fraction. Importantly, contributions from exciton coupling are neglected in our approach, although these values are expected to be considerably smaller than the benchmark P3HT system due to larger π-stacking distances in P3ATV aggregates. This is supported by the fact that absorption fit parameters were obtained independently from Raman intensity simulations, meaning that exciton coupling contributions would probably not lead to appreciable changes in the absorption vibronic line shape beyond the harmonic approximation.

It is also possible to simulate Raman excitation profiles using eqs. 1−3 by varying the incident photon energy (ωI) for each mode while holding all other fit parameters constant. Simulated profiles were included in the Supporting Information to this article and show similar qualitative characteristics as experimental profiles (i.e., enhancements near the absorption maximum and low-energy onset). More detailed comparisons between experimental and calculated profiles were not possible because of the lack of sufficient excitation wavelengths near the P3ATV absorption onset and maximum.

In addition to exposing vibrational mode-specific excited state rearrangements in P3ATV aggregates, it is informative to consider the implications of Γ that dictate the extent to which time-dependent vibrational wavepackets propagate on the excited state potential surface. Although this parameter is described here as a phenomenological damping term, it represents the intrinsic lifetime of the resonant chromophore and coupling to the medium (e.g., phonon bath). Comparing mode-specific wavepacket cross-correlation overlaps reveals that the high-frequency P3ATV backbone vibrations (i.e.ν_{9-11}) make at least two return visits to the Franck−Condon region before their amplitude is completely damped. This feature can also be understood by comparing vibrational periods given by $(c\hbar\omega)^{-1}$, where c is the speed of light and $\hbar\omega$ is the vibrational frequency in cm^{-1}, with the characteristic time of Γ. From this relationship, the periods of ν_{9-11} are in the range of ~20−30 fs, much smaller than Γ (~90 fs). Interestingly, characteristic time scales of singlet fission from the initial $^{1}B_{u}$ excited state were reported to be ~45 fs.[165,167] The survival of the ν_{9-11} Raman wavepacket for several periods on the $^{1}B_{u}$ state potential surface suggests that electronic relaxation processes on similar time scales are possibly coupled to displaced backbone vibrational motions. This result uncovers potentially vital roles of vibrations in mediating relaxation between excited states beyond what is currently understood from pure electronic energy level models borne out from dynamics studies that neglect vibrations[165]. Furthermore, aggregated and amorphous P3ATV chains should have markedly different relaxation characteristics and singlet fission yields due to different exciton coherence lengths and singlet−triplet energy splitting. However, the overlapping nature of these absorption transitions, in addition to spectral resolution limits of transient absorption techniques, mask these contributions. It is important to stress that while we are not directly measuring relaxation dynamics between different excited electronic states, these processes must be considered as vibration assisted and we expect that time-resolved Raman experiments may further uncover details of the extent of vibrational coupling in interstate relaxation processes (i.e., Franck−Condon factors).

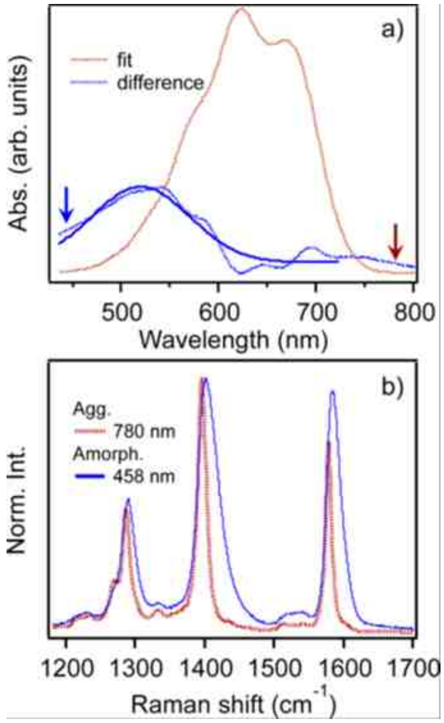

Figure 5.8 (a) Simulated P3ATV absorption and difference spectra generated from subtraction of the fit from the experimental line shape. A Gaussian function was fitted to the difference spectrum to extract band maxima wavelengths. (b) Raman signatures of the limiting aggregated (red) and amorphous (blue) P3ATV forms generated by selective resonance excitation (denoted by downward arrows in a).

Thus far we uncovered two new and important results that advance our understanding of P3ATV structural and electronic properties: (i) excited state geometries are significantly distorted along multiple coordinates relative to the ground electronic state unlike well-studied P3HT aggregates[181]; (ii) it is now possible to decompose experimental spectroscopic line shapes into contributions from both aggregated and amorphous P3ATV chains.

The absorption signatures of amorphous P3ATV fractions can now be visualized by subtracting the simulated absorption spectrum from experiment (Figure 5.7b). Figure 5.8a shows experimental and simulated P3ATV absorption spectra and difference spectra. A Gaussian function is fitted to the latter to determine line width and λ_{max}. As expected, these P3ATV absorb at higher energy, and line shapes are nearly devoid of resolved vibronic structure. Raman spectra of aggregated and amorphous P3ATV forms are obtained from selective excitation of their distinct absorption line shapes in Figure 5.8a.

P3ATV aggregate Raman signatures are generated by exciting on the red edge of the aggregate absorption (780 nm), whereas the amorphous form is selected using 458 nm light (Figure 5.8b). Absorption cross-talk is likely in the latter excitation regime due to small, but nonzero, absorption of the aggregates. As shown in Figure 5.8, both Raman line shapes have different characteristic frequency maxima and relative intensity distributions that can now serve as markers for determining the relative amounts of each species and variations in their structural properties. We chose not to fit the amorphous

P3ATV absorption line shape due to the lack of resolved structure that may lead to large uncertainty in fit parameters (i.e., Δ and Γ).

5.4 Resonance Raman and Photocurrent Imaging of P3ATV Solar Cells

The crystalline nature and lower energy absorption of P3ATVs make them good candidates for solar cell applications due to the prospect of enhanced charge transport and better harvesting of NIR solar photons. However, these materials have not performed nearly as well as related polythiophenes, which is believed to stem from non-ideal morphologies when blended with suitable electron acceptors (e.g., soluble fullerenes). These shortcomings may possibly be alleviated if triplet excitons can be harvested following singlet fission to generate multiple charges with a single photon. Unfortunately, basic structure−property knowledge has lagged considerably behind, thus limiting rational design strategies to optimize material performance. We now extend our studies to mapping microscopic structure − function relationships in model P3ATV/fullerene solar cells using resonance Raman and photocurrent imaging techniques. This approach benefits from our ability to resolve contributions from both aggregated and amorphous P3ATV fractions that are sensitive to changes in local packing and composition (i.e., fullerene content).

Bulk heterojunction (BHJ) type solar cells are fabricated by blending P3ATVs with a soluble fullerene derivative, PCBM, in solution and then spin cast to form the active layer. As previously shown in other polymer/fullerene blends, the polymer aggregate fraction is usually diminished when fullerenes are added but can be partially restored by annealing[183]. We exploit the high sensitivity of resonance Raman intensities to the polymer packing characteristics and generate in-situ maps of how specific structural variants are affected by local film composition (morphology). Moreover, valuable correlations between microscopic structure and performance are exposed that are not obtainable by conventional ensemble device and spectroscopic characterization or electro-mechanical surface probe techniques.

Figure 5.9 shows I−V curves of P3ATV solar cells in the dark and under AM1.5 irradiation for as-cast films. Overall, PCEs were typically <1%, similar to previous results from similar P3ATV/fullerene blends[172]. Light thermal annealing treatments (e.g., 130 °C, 20−30 min) brought about small improvements in performance, and small (<1 μm) fractal-like crystallites of PCBM became apparent in films annealed for longer times. Open-circuit voltages (VOC) are ~0.28 – 0.32 V, smaller than those found in more common polythiophene derivatives, consistent with either smaller HOMO − LUMO (donor−acceptor) energy offsets or unfavorable interface morphologies[184].

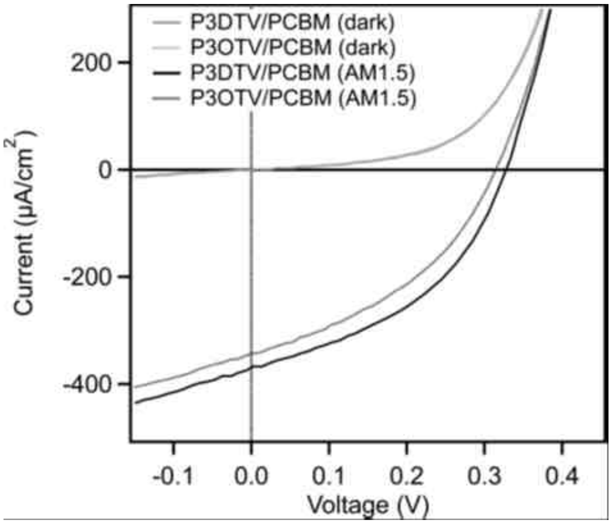

Figure 5.9 I−V curves of model P3ATV/PCBM solar cells in the dark and under AM1.5 illumination.

Resonance Raman and photocurrent imaging of P3ATV/PCBM solar cells was performed using an approach described in detail earlier[185]. The 532 nm line of a Kr-ion laser served as the excitation source that excites both aggregated and amorphous P3ATV components nearly equally, and the device was raster scanned over the diffraction-limited laser spot to generate Raman and photocurrent images over the same scan area. Excitation intensities were ~1 kW/cm2 for both measurements, which was necessary to produce currents above the detection limit due to the intrinsically low PCE. Figure 5.10

shows resonance Raman and photocurrent images for a representative annealed 3DTV/PCBM device.

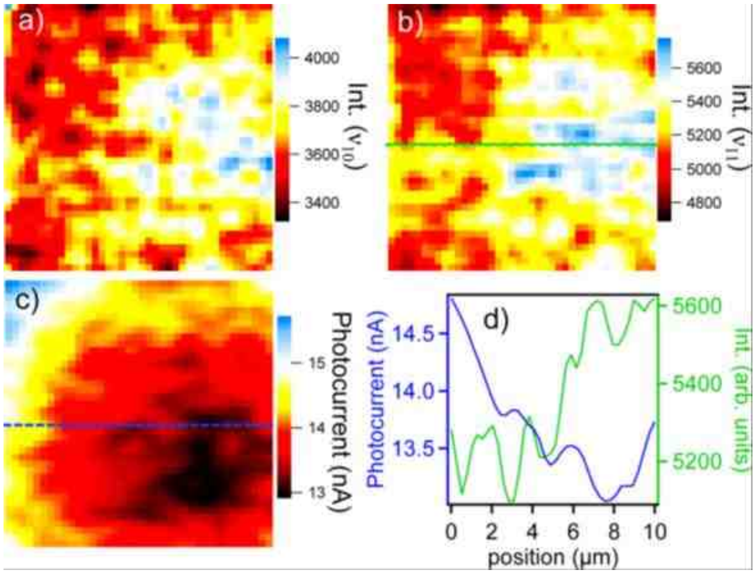

Figure 5.10 Raman and photocurrent images of an annealed P3DTV/PCBM solar cell under 532 nm excitation. Integrated intensity images (a, b) of C=C thienylene (ν10) and vinylene (ν_{11}) stretches. Photocurrent magnitude (c) from the same scan area (10 × 10 μm), and (d) comparison of Raman intensity and photocurrent linescans denoted in b and c.

Raman images are produced by mapping the integrated intensity for a particular band, and we focus on the dominant P3DTV C=C thiophene- and vinyl-symmetric stretches ($\nu_{10,\ 11}$) displayed in Figure 5.10a and 5.10b. Corresponding photocurrent images for the same scan are shown in Figure 5.10c. As-cast devices showed little discernible phase separation in both Raman and photocurrent images, indicating a well-mixed phase or separation below the spatial resolution of the instrument.

Comparing photocurrent and Raman intensity images for annealed devices reveals decreases in current production in regions with larger P3DTV concentration (intensity). This feature originates from some demixing between the polymer and the fullerene leading to poor charge generation. Surrounding regions show improved photocurrent production, suggesting better mixing and charge separation efficiency. Similar observations have been noted in annealed P3HT/PCBM blends where current decreases are observed in PCBM crystallites and P3HT aggregates due to the inability of PCBM to intercalate in the latter structures. Line scans of the ν11 mode Raman intensity image and photocurrent for the same region (Figure 5.10d) further illustrate the anti-correlation between P3ATV-rich regions and photocurrent generation efficiency. Again, these aspects are qualitatively similar to P3HT/PCBM solar cells where the tendency of both components to crystallize negatively impacts charge generation yields because of phase segregation when films are annealed. However, the miscibility characteristics of PCBM in P3ATVs are expected to differ considerably owing to the additional vinylene linkage between thiophene groups as well as longer alkyl side groups and packing distances.

Previous X-ray scattering studies of a related P3ATV blended with PCBM revealed that both components were well mixed in the regime of 1:1 w/w loadings or less[172]. Moreover, P3ATV aggregate diffraction peaks are still present and unaltered from the pristine state in this PCBM loading range[172]. This was further confirmed by measuring absorption spectra of P3ATV/PCBM blends that showed no significant –

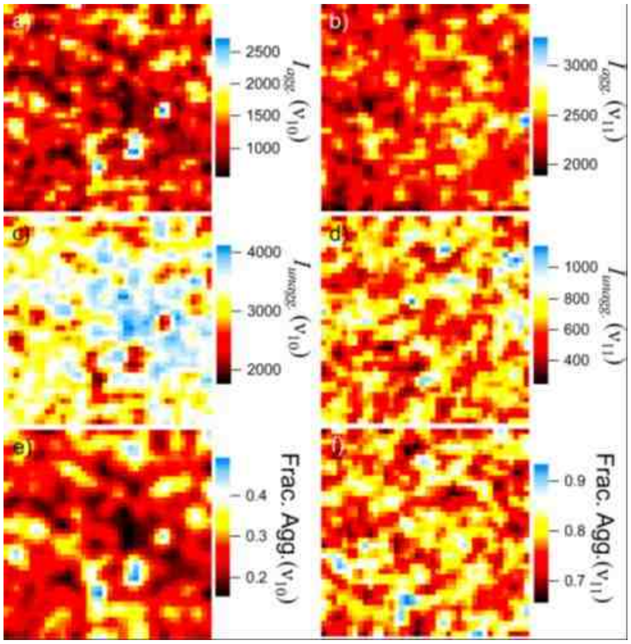

Figure 5.11 Raman integrated intensity images of modes ν10 and ν11 for aggregated (a, b) and unaggregated (c, d) P3ATV components. (e and f).

– changes in the P3ATV absorption line shape implying that PCBM mixes well with both polymer forms (see Supporting Information). Additionally, Raman spectra of P3ATV/PCBM blends (1:1 w/w) were measured with 780 nm light to verify the nature of aggregate chain packing and found virtually identical line shapes compared to pristine P3ATVs excited at the same wavelength.

Using our multispecies description of P3ATV optical and Raman spectra, it is now possible to spatially map contributions from aggregated and amorphous fractions of P3ATV in the blend solar cell active layer. We use Raman spectra of the two limiting identified earlier in Figure 7 and perform a linear least-squares fit of experimental Raman line shapes used to construct intensity images in Figure 5.10. Figure 5.11 shows integrated intensities of aggregated (Figure 5.11a and 5.11b) and amorphous (Figure 5.11c and 5.11d) P3ATV chains for ν10 and ν11 modes, respectively. Distinct correlations between the locations of aggregated and amorphous chains are apparent in ν10 images involving the thienylene-symmetric C=C stretching and the results clearly show that regions with greater amorphous fractions correspond to lower photocurrent output. This behavior is opposite of that observed in P3HT/PCBM where crystallization causes currents to decrease in aggregated regions. It is also important to note that the size scale and shapes of domain features are also different, which most likely originates from the molecular miscibility of PCBM with P3ATV.

On the basis of the invariance of absorption and Raman line shapes upon addition of PCBM, we propose that fullerenes remain on the periphery of P3ATV chains (either aggregates or amorphous) and do not interact significantly with the backbone. This is consistent with X-ray scattering studies showing that phase separation does not occur until PCBM loadings exceed 1:1 w/w, suggesting PCBM molecules tend to remain in P3ATV alkyl side groups or at domain boundaries[172]. Furthermore, no change in aggregate π-stacking or interlamellar spacing was observed when PCBM was added, which is consistent with the insensitivity of excitons to minor disturbances involving side groups. The reduced PCBM amounts in amorphous P3ATV zones is surprising generally because these chains can more readily accommodate fullerenes compared to aggregates where close packing can restrict access. This behavior indicates that PCBM may stabilize aggregates or possibly induce aggregation and ordering. However, annealing promotes PCBM crystallization, which might destabilize aggregates. Although we are pursuing detailed studies to further understand this phenomenon, the overall weaker interaction between P3ATVs and fullerenes elucidated from Raman spectroscopy and imaging helps close the loop in explaining the molecular origins of poor performance in solar cells

5.5 Conclusions

We used CW resonance Raman probes of non-emissive P3ATV systems to expose vibrational mode-specific excited state structural displacements and contributions of intrinsic polymorphs that have so far gone unreported in this class of polymers. X-ray diffraction and optical absorption spectroscopy verified the preponderance of aggregate formation in P3ATVs that remains undisturbed even in the presence of appreciable amounts of fullerenes. Excitation wavelength-dependent Raman frequencies and intensities showed strong evidence for overlapping transitions from both aggregated and amorphous P3ATV chains. This assignment was confirmed by time-dependent Raman wavepacket simulations to calculate Raman intensities, and parameters were then used to generate absorption spectra that showed excellent agreement with experiment. Simulated absorption spectra were subtracted from experiment to reveal the line shape of the minority amorphous P3ATV fraction. Raman line shapes of each P3ATV structural form were generated by selective resonance excitation of their characteristic absorption line shapes. This new description of distinct structural variants in P3ATV derivatives explains all observed spectroscopic behaviors without the need to invoke contributions of optically forbidden Ag dark states.

By extending this model to resonance Raman and photocurrent imaging studies of P3ATV/PCBM blend solar cells, we further uncovered new structure − function correlations. For example, spatial maps of morphology-dependent distributions of the limiting aggregated and amorphous P3ATV forms were produced and directly correlated with photocurrent production in the same scan area. Interestingly, regions with larger aggregate fractions showed larger photocurrents, contrary to earlier findings in the benchmark P3HT/PCBM blend, indicating better mixing with fullerenes. On the other hand, P3ATV-rich regions correspond to the amorphous fractions that have lower photocurrent output. Overall, these results confirm that although PCBM mixes well with both fractions the length of separation between polymer donors and fullerene acceptors is significantly larger than in related polymers. We believe this may be due to P3ATV side groups or chain packing arrangements (i.e., interpenetrating side groups), restricting PCBM from interacting with the conjugated backbone segments. The invariance of absorption, X-ray, and Raman spectra of P3ATV aggregates in the presence of PCBM support this hypothesis, which explains overall poor charge generation yields in these materials. We expect that new strategies to tune side group substitution patterns may enable better mixing and improve material performance.

Chapter VI

Spatially Resolving Ordered and Disordered Conformers and Photocurrent Generation in Intercalated Conjugated Polymer/ Fullerene Blend Solar Cells

6.1 Introduction

The degree of mixing of fullerene acceptors with conjugated polymer donors used for thin film BHJ solar cells has significant implications for determining morphologies and overall device performance[186,187]. Blends of PBTTT and PCBM are an ideal BHJ system for understanding how molecular mixing influences the outcomes of photovoltaic processes[188–190]. PBTTT chains readily assemble into well-ordered π-stacked lamellar crystalline structures[191], essential for establishing multidimensional charge and energy transfer pathways. Extensive X-ray scattering and diffraction[190–194], solid-state NMR spectroscopy[190], differential scanning calorimetry (DSC)[188], and IR spectroscopy studies on PBTTT/PCBM blends have demonstrated the preponderance of fullerene intercalation into the polymer alkyl side groups resulting in bimolecular co-crystals following annealing treatments[192,195]. PBTTT lattice spacing and paracrystalline disorder in the π-stacking direction increase with fullerene intercalation that is marked by broadening in

X-ray diffraction peaks and increased amounts of the gauche alkyl side group conformation[190].

The PBTTT/PCBM system has proven a useful model for predicting optimal blend stoichiometries and morphologies, however, solar cell power conversion efficiencies are <3%[196,197], well below current benchmarks[12,198,199]. This result is surprising considering the relatively high charge mobilities of pristine PBTTT (>0.001 cm2/V/s at low charge densities)[200–204], yet it underscores the need to better understand how ground state structure and interactions influence excited state photophysical processes[36]. Ultrafast pump − probe transient absorption spectroscopy (TAS) of PBTTT/PCBM blends show evidence of charge separation on time scales <1 ps. followed by efficient geminate recombination of separated charge carriers occurring on time scales of ~200 ps[205]. These results are consistent with a well-mixed phase favoring efficient charge generation but separated carriers lack sufficient transport pathways and cannot escape Coulomb attractions thus recombining on fast time scales[134,205]. Importantly, X-ray spectromicroscopy studies of PBTTT/PCBM blends produced estimates of acceptor miscibility of 42 wt. %9 implying that TAS dynamics are dominated by a well-mixed phase but it is difficult to determine if this corresponds solely to bimolecular crystals. Furthermore, spectroscopic and charge transport studies have shown evidence of structurally similar PBTTT conformational polymorphs (conformers) with energy differences of ~ 0.1 eV.24,25 PCBM intercalation is expected to disrupt PBTTT conformation and packing in blends but connecting specific ground state structures and interactions to the outcomes of excited state photovoltaic processes remains more elusive.

Here, we use resonance Raman spectroscopy to identify signatures of structurally distinct PBTTT conformers in PCBM blends and track their evolution by varying processing conditions, composition and excitation energies. Resonance Raman and photocurrent imaging are then used to spatially map and correlate their contributions to local material performance in model PBTTT/PCBM solar cells. We show that the PBTTT alkyl-thiophene symmetric C=C stretching vibration (~1490 – 1500 $\mathrm{cm^{-1}}$) can be decomposed into contributions from ordered (lower energy, $\hbar\omega_{C-C}$ = 1489 $\mathrm{cm^{-1}}$) and disordered (higher energy, $\hbar\omega_{C-C}$ = 1500 $\mathrm{cm^{-1}}$) PBTTT conformers which are not evident in optical spectra. We propose that both ordered and disordered PBTTT species are well-mixed with PCBM but only the former exist only in the bimolecular crystal phase. Density functional theory (DFT) Raman simulations and excitation energy dependent Raman spectra indicate that ordering of alkyl-thiophene rings defines the two observed PBTTT forms and the relative amounts of each are determined by the PCBM loading and film processing conditions. Raman excitation profiles further demonstrate that annealing converts the disordered form to bimolecular crystals suggesting that it is in fact a precursor kinetic phase. Well resolved overtone and combination transition intensities (up to 4 quanta) − chiefly involving the dominant PBTTT CC symmetric skeletal vibrations (~1400 — 1600 cm^{-1}) − are also apparent and intensities show much smaller sensitivity to PCBM loading indicating PBTTT excitations are electronically localized for both species.

Raman images demonstrate that a significant fraction of ordered PBTTT chains reside in PCBM-rich regions confirming these are indeed bimolecular crystals. However, corresponding photocurrent images show substantial losses in these regions, likely due to efficient geminate charge recombination. Intensity modulated photocurrent spectroscopy

(IMPS) measurements of annealed PBTTT/PCBM devices also display positive phase shifts at low modulation frequencies (i.e., photocurrent leads the modulation frequency), which is a signature of non-geminate charge recombination becoming operative[206,207]. IMPS images of these model PBTTT/PCBM solar cells reveals that this process is most prevalent at boundaries of ordered/disordered PBTTT and PCBM aggregates.

6.2 Results and Discussion

6.2.1 Optical and Raman Spectroscopy

In general, conjugated polymers become more disordered as fullerene loading increases due to disruption of packing arrangements and reduced planarity between monomers[181,208]. In crystalline polymers, such as the archetype poly(3-hexylthiophene) (P3HT) system, addition of PCBM breaks up π-stacked lamellar chains in aggregates leading to increases in a solution-like amorphous component with higher energy and featureless absorption lineshapes[83,185]. The ability of PCBM to intercalate into PBTTT chains presents an intriguing case challenging traditional views of order/disorder transitions. Spectroscopic and electrical imaging approaches are used here to (i) identify spectroscopic markers of intercalated PBTTT chains in PCBM blends, (ii) assess how ground state structures and interactions affect excited state processes, and (iii) spatially correlate local composition and order/disorder characteristics to material performance in functioning solar cells

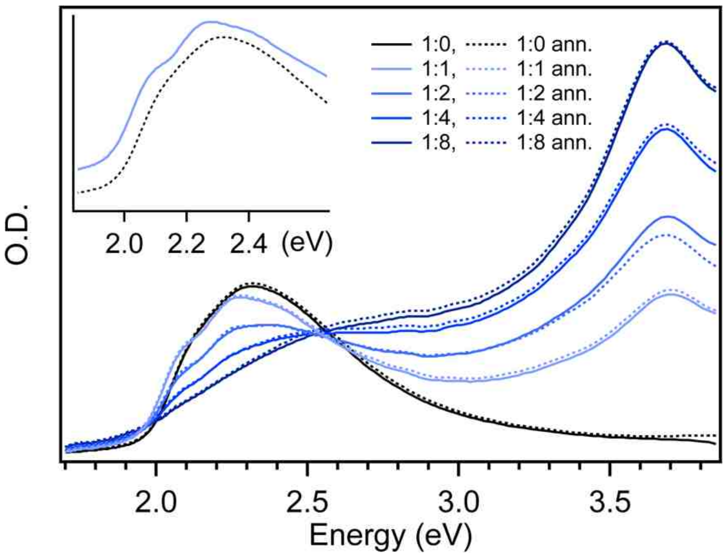

Figure 6.1 Optical absorption spectra of as-cast (solid traces) and annealed (dotted traces) PBTTT/PCBM blend thin films at several PCBM loadings. Inset: comparison of pristine PBTTT and a 1:2 w/w PCBM blend (offset for clarity).

We begin by re-examining the effect of variable PCBM content in PBTTT blend thin film absorption spectra which will be useful later for selection of resonance Raman excitation schemes (vide infra). Figure 1 displays as-cast (solid traces) and annealed at 140 °C for 20 min (dotted traces) PBTTT/PCBM blend thin films with 1:1, 1:2, 1:4, and 1:8 w/w ratios deposited on clean glass substrates. Improved resolution of vibronic structure near the PBTTT absorption onset is observed in addition to a slight red-shift

(~0.04 eV) relative to the pristine PBTTT line shape (see Figure 1 inset). As PCBM loading increases the PBTTT contribution decreases concomitantly with an increase of a broad and overlapping higher energy component consistent with the PCBM absorption line shape. Spectra from annealed blends show relatively small changes compared to as-cast films suggesting that conversion from a kinetic mixed (as-cast) phase to the bimolecular crystal phase is not as efficient as reported previously for higher annealing temperatures (i.e., approaching the liquid crystalline transition of PBTTT).

PBTTT/PCBM blend absorption spectra in Figure 1 generally resemble previously published spectra in the singlet exciton onset region[195,196] but differ from other reports that show better resolution of vibronic structure. This improvement of vibronic resolution upon PCBM addition and annealing has been attributed to bimolecular crystal formation. However, Gasperini and Sivula also recently showed that higher molecular weight PBTTT (>40 kDa) leads to entanglement of chains and rougher film textures that may inhibit bimolecular crystal formation in PCBM blends for larger PBTTT molecular weight fractions in our samples[209]. Single-molecule images and spectra of PBTTT diluted into a polystyrene host matrix were also recorded to verify if PBTTT chains were pre-associating in solution prior to blending with PCBM, which might also inhibit bimolecular crystal formation. Images show well-isolated, diffraction-limited spots and areal densities scale linearly with concentration demonstrating that no agglomeration or gelling occurs in our concentration range. We expect that incomplete conversion of a well-mixed, kinetic PBTTT/PCBM phase into bimolecular crystals may arise in films with larger PBTTT molecular weight and polydispersity. However, this feature is advantageous for our study because the range of accessible PBTTT conformations upon PCBM intercalation can be tracked and correlated with their performance attributes.

Evidence of adverse intercalation-induced disorder effects on electrical properties in PBTTT/PCBM blends manifest as over an order of magnitude decrease of charge mobilities[196,210]. This dramatic decrease in mobility is believed to originate from twisted PBTTT backbones and side group disorder due to intercalated fullerenes. Solid-state NMR studies of PBTTT/PCBM blends support this view and found that ^{13}C and ^{1}H signals from the less-ordered gauche alkyl side group conformer, a minority species in pristine PBTTT (<10%), increase with PCBM loading[190]. Likewise, a Franck−Condon analysis of pristine PBTTT absorption lineshapes showed evidence of two distinct transitions with electronic origin transitions separated by ~0.1 eV.24 The relatively small difference in energy between apparent intrinsic PBTTT structures potentially complicates the use of absorptive spectroscopies for quantifying amounts and properties of these species since lineshapes strongly overlap and become even more congested in PCBM blends. Resonance Raman spectroscopy can help overcome these issues using selective resonant excitation schemes to target specific electronic excited states corresponding to distinct PCBM intercalation-dependent PBTTT conformers.

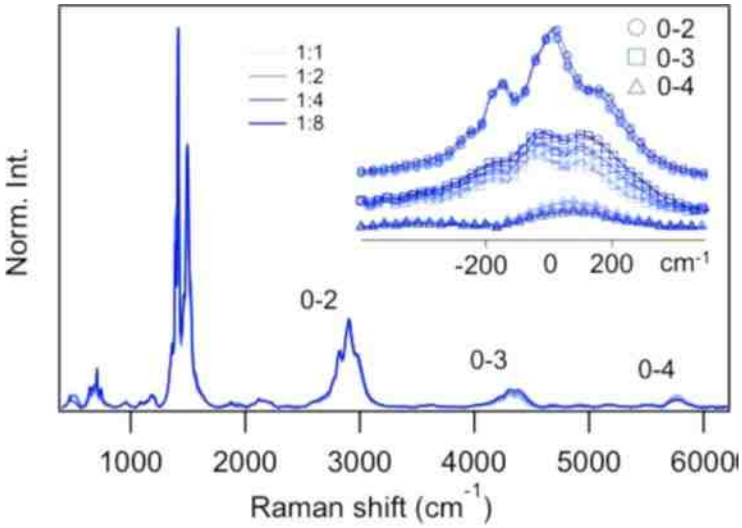

Figure 6.2 Resonance Raman spectra of PBTTT/PCBM blend thin films (excitation energy = 2.41 eV) with overtone/combination band transitions highlighted and shifted to the most intense transition (inset).

Figure 2 presents representative resonance Raman spectra of PBTTT/PCBM blend thin films excited with 514.5 nm (2.41eV) light corresponding to the maximum of the PBTTT absorption line shape. Resonance excitation usually leads to large enhancements (~1 × 105 to 1 × 1010) in Raman scattering cross sections of the resonant chromophore. Contributions from PCBM in the excitation wavelength range used are absent demonstrating that PBTTT Raman cross section enhancements overwhelm those of PCBM despite that it is usually present in larger concentrations (e.g., >1:1 w/w). Well-resolved progressions of overtone and combination bands, mainly involving vibrations of PBTTT C−C and C=C stretching character (see Table 1), are visible. Comparison to IR absorption spectra of PBTTT/PCBM blends in the first overtone/combination band region (0−2) as well as the appearance of higher order progressions confirm these are not fundamentals of high frequency modes (i.e., C−H stretches)[190]. Table 2 lists mode assignments of both fundamental and overtone/combination bands (for only the 0−2 region).

Table 2. Assignments of Main Backbone Raman Bands from PBTTT/PCBM Blends in the Fundamental (0-1) and First Overtone (0-2) Regions

peak	frequency (cm−1)	assignment
ν1	1340	
ν2	1365	
ν3	1391	thiophene C−C stretch[a]
ν4	1415	thienothiophene C=C stretch[a]

ν5	1467	inter-ring thiophene C−C stretch[a]
ν6	1489	thiophene C=C stretch[a]
ν7	1500	
ν8	1523	
ν9	1563	
	2771	2ν3
	2804	ν3 + ν4
	2831	2ν4
	2876	ν4 + ν5
	2908	ν4 + ν6
	2934	2ν5
	2977	2ν6; ν5 + ν7
	3013	ν6 + ν8

[a] Determined from DFT simulations (see below) and ref.[211]

From Figure 2, we note that only the C−C and C=C symmetric stretches of the thiophene and thienothiophene backbone rings display pure overtone transitions. Higher-order (>0−2) overtone/combination band clusters show greater broadening, probably because of dispersion effects (i.e., wavepacket broadening) due to coupling between nuclear motions. Weak clusters of combination bands from multiple low frequency vibrations, likely from thiophene-thienothiophene ring bends and librations, are also apparent before the 0−2 region (~1700 — 2500 cm^{-1}). The appearance of multiple apparent progression-forming modes suggests that vibrational displacements are large (i.e., large Huang−Rhys factors, $S = \sum_i^n \ {}^1\!/_2\, \Delta_i^2$, where Δ_i is the displacement for mode i. However, PBTTT absorption band line widths (fwhm) are not significantly different than P3HT or other crystalline polymers ($S \approx 1.0$)[81] meaning that the total vibrational displacements are probably similar. Raman lineshapes in Figure 2 also offer useful insights into PBTTT absorption features. Namely, the weakly resolved vibronic interval can be explained by the Franck−Condon displacement of multiple low frequency modes causing the “valleys” between dominant mode progressions (i.e., the PBTTT CC backbone symmetric stretches, $\nu 3 - 7$) to become filled in. Conversely, increased inhomogeneous broadening might also explain larger absorption vibronic line widths in pristine PBTTT, however, narrowing of line widths in PCBM blends suggests increased order or longer excited state lifetimes The latter effect is not expected due to the presence of intimately mixed PCBM electron acceptors. It is also useful to point out that overtone/combination band intensities show less sensitivity with increased PCBM loading (constant excitation energy) implying that either disorder effects are not important until longer times (several vibrational periods, >100 fs) or chromophores are spatially localized making them less sensitive to disorder. Typically, in large molecules with many displaced modes, overtone/combination intensities are usually extinguished before the first overtone (0–2) region because of destructive interference caused by rapid damping from strong coupling to the bath or among chromophores of different energies (inhomogeneous broadening)[76]. This effect appears suppressed in PBTTT systems and we speculate the persistence of the multimode overtone/combination band transitions in PBTTT/PCBM blend Raman spectra arises from weak coupling to the phonon bath and small contributions from inhomogeneous broadening effects.

6.2.2 Identifying Ordered and Disordered PBTTT Conformers

The qualitative picture emerging from Raman trends reported in Figure 2 is that the multidimensional excited state wavepacket survives for longer times allowing sufficient buildup of overlap and overtone/combination intensities. This scenario is most consistent with localized excitations despite the relatively high order of PBTTT (even in PCBM blends) that intuitively suggest delocalized electronic structures. The implications of localization/delocalization in polymeric solar cells are significant and have been the subject of recent investigations of ultrafast charge separation[164,212–214]. For example, Jamieson et al. highlighted the importance of fullerene crystallites in promoting charge separation while simultaneously suppressing geminate recombination in several polymer/fullerene systems that show varying degrees of mixing[214]. We consider these aspects for interpreting Raman/photocurrent images in the following.

Further insights into the nature of PBTTT chromophores PBTTT/PCBM blends can be obtained from resonance Raman spectra as a function of excitation energy spanning the PBTTT optical absorption line shape (~1.9 – 2.7 eV). Figure 3 displays variable excitation energy Raman spectra and are normalized to the thienothiophene ring C=C symmetric stretch (1415 cm^{-1} mode, ν4) for comparison. Raman patterns show significant changes with excitation energy consistent with resonant excitation of distinct PBTTT chromophores. In the 0−1 region, the relative intensity of the 1391 cm^{-1} mode (thiophene symmetric C−C stretching character) decreases and the ~1489−1500 cm^{-1} band region of the symmetric C=C thiophene ring stretch gains in intensity in addition to apparent blue-shifting and broadening with increased excitation energies. Comparison of the two PCBM loadings also demonstrates specific interactions with PBTTT backbones. For example, a large increase in relative intensity is observed for the ~1489−1500 cm^{-1} mode in the 1:4 blend for excitation near the PBTTT resolved absorption onset (1.92 eV), suggestive of bimolecular crystals.

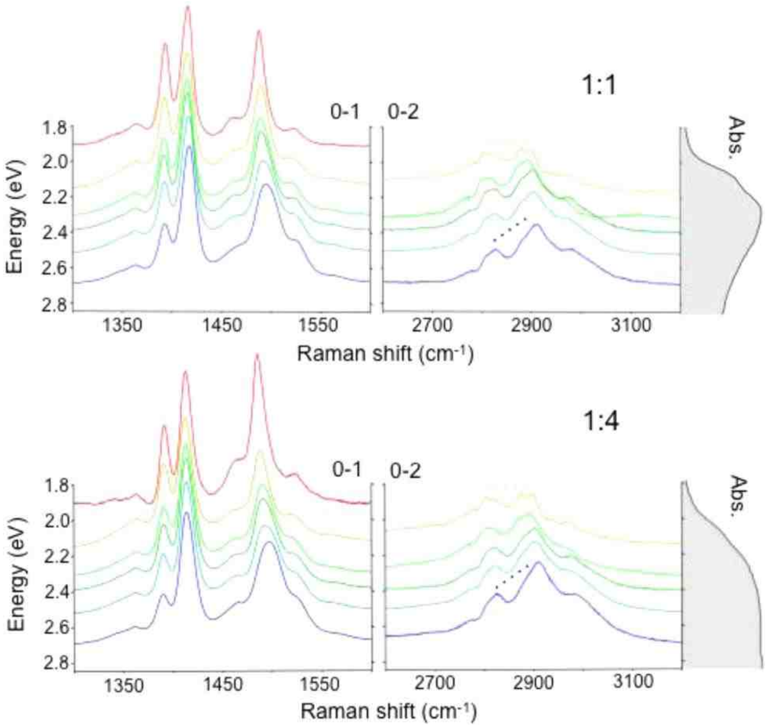

Figure 6.3. PBTTT/PCBM (1:1 and 1:4 w/w loadings) resonance Raman spectra as a function of variable excitation energies displayed in the fundamental (0−1) and first overtone (0−2) regions of the main PBTTT backbone stretching modes. Corresponding optical absorption spectra are shown and dotted lines indicate changes in 0−2 intensity distributions.

Chromophore-specific resonance enhancement is more obvious in the first overtone (0−2) region where increasing excitation energy causes intensity redistributions toward higher frequencies. Residual fluorescence masks overtone/combination bands in the background noise at the lowest excitation energy (647 nm, 1.92 eV) and these spectra were not included. For comparison, we measured Raman spectra of pristine non-resonant conditions (λ_{exc} = 785 nm, 1.58 eV), that show pronounced red-shifts of the main PBTTT skeletal stretching vibrations for the blend. It is likely that nascent bimolecular crystals in the blend become preresonant at this excitation energy, which also gives rise to very weak overtone transitions.

We propose that line shape (intensity) changes with excitation energy reflect the presence of both ordered and disordered PBTTT conformations whose populations are modulated by PCBM loading and annealing. Raman excitation profiles (REPs) are now constructed to test this hypothesis that reveal vibrational mode-specific views of the excited state potential energy landscape. Figure 4 shows REPs from as-cast PBTTT/PCBM films (solid traces) for all backbone skeletal vibrations showing appreciable intensity in resonance Raman spectra in Figures 2 and 3 (ν3−7) and intensities are reported relative to a non-absorbing external standard (i.e., sapphire). Generally, REPs bear similarity to absorption lineshapes provided that Raman and absorption transitions involve only a single excited state (i.e., single absorber). REP lineshapes in Figure 4 show noticeable deviations from one-photon absorption spectra (Figure 1) confirming contributions from multiple states. In particular, a pronounced dip around ~2.35 eV is observed as well as increased activity (cross sections) in the higher energy region of the main PBTTT absorption line shape. As PCBM concentration increases, the relative intensities of the lower energy feature decrease for all mode specific REPs reported. The dip at 2.35 eV probably results from the crossing of excited state potential energy surfaces of two states leading to destructive quantum interference and intensity de-enhancements[177].

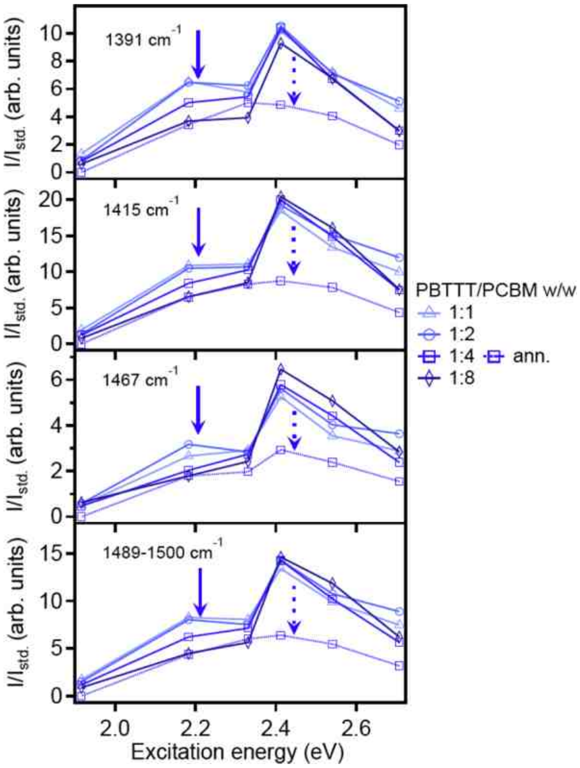

Figure 6.4 Raman excitation profiles (REPs) of the PBTTT backbone symmetric stretching fundamental (0−1) region from variable PBTTT/PCBM loadings.

On the basis of the trends observed here and from previous studies, it is relatively straightforward to assign the low (high) energy REP feature to ordered (disordered) PBTTT chains. Because of the amounts of PCBM used, PBTTT should always exist in a mixed phase owing to large cohesive energy densities between these molecules and available intercalation sites[188,215]. We next measured REPs of an annealed 1:4 w/w PBTTT/PCBM blend (dotted traces, Figure 4) and compare these to as-cast REP lineshapes. A pronounced decrease of the higher energy REP component is apparent indicating conversion to PBTTT chains with improved backbone and side group order consistent with intercalated bimolecular crystals. This result highlights the greater sensitivity of Raman techniques to chromophore environments compared to one-photon absorption spectroscopy (Figure 1), which can obscure contributions from closely overlapping states.

We now focus on the ~1489 — 1500 cm^{-1} region assigned to the C=C symmetric stretch of the thiophene rings (ν6,7, Table 1) that are particularly sensitive to PCBM loading and excitation energy (Figure 6.3). Figure 6.5a presents resonance Raman spectra generated from a PBTTT/PCBM blend thin film of a 1:2 w/w ratio in the thiophene C=C symmetric stretching fundamental region. Excitation at the PBTTT red absorption onset (i.e., 1.92 eV) selects the 1489 cm^{-1} (ν6) component that subsequently blue-shifts and coalesces into the ~1500 cm^{-1} mode (ν7) at higher excitation energies (i.e., 2.71 eV). These trends have been explained previously from theoretical studies of oligothiophenes where lower energy chromophores (viz. longer conjugation lengths) show red shifted Raman-active backbone vibrations[216]. The 1500 cm−1 mode is proposed to originate from disordered PBTTT C=C thiophene rings, probably because of fullerene intercalation induced disorder among the alkyl side groups causing twisting of the backbone thiophene rings and greater paracrystalline disorder. Likewise, the 1489 cm−1 component of the symmetric thiophene C=C stretch derives intensity from ordered PBTTT chains in bimolecular crystals, where side group and backbone order is improved. Line widths of both PBTTT C=C thiophene forms are also consistent with their proposed structural origins, namely, ordered conformers are ~15 cm-1 compared to ~25 cm−1 for disordered chains because of heterogeneity. This feature is also consistent with improved vibronic resolution in absorption spectra of PBTTT/PCBM blends, which indicates the presence of ordered PBTTT chains in bimolecular crystals. The relative amounts of ordered and disordered PBTTT conformers) are estimated by deconvoluting the C=C thiophene band using two line shape functions corresponding to the ν6 and ν7 bands (Table 1). We do not attempt to obtain absolute cross sections for each species but it is expected that these–

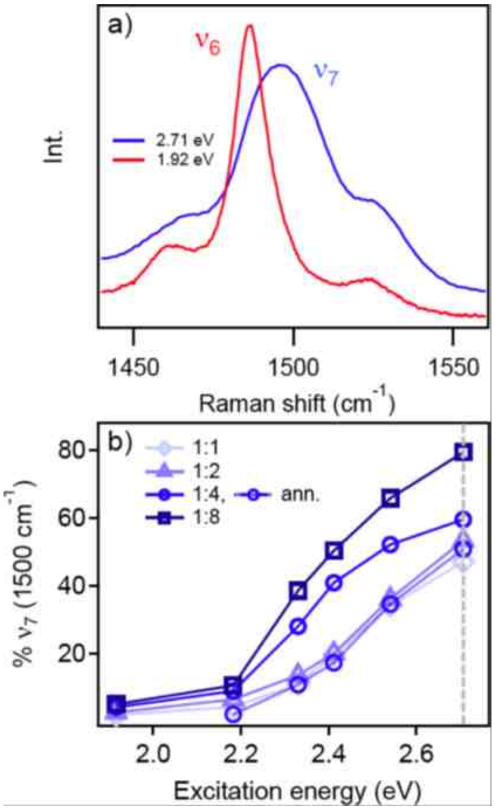

Figure 6.5 (a) Resonance Raman spectra of as-cast PBTTT/PCBM blend thin films (1:2 w/w) showing lineshapes of the two distinct PBTTT forms; ordered (ν6) and disordered (ν7) PBTTT chains. (b) Percent of disordered species present in all blend ratios as a function of excitation energy. The dashed line represents the resonance maximum excitation energy of the disordered form (2.71 eV).

–values are similar because of the structural similarity of ordered and disordered forms (i.e., energy difference of ~0.1 eV or less), which is much subtler than in other crystalline polymers displaying polymorphic behavior, such as P3HT. In this description, the total C=C thiophene Raman band intensity is a linear combination of both components and we use this simple model to assess how the amounts of disordered PBTTT conformers, $((I_7)/(I_6+I_7))$, change with blend film processing conditions. We further speculate that the disordered component is the precursor species to the ordered PBTTT form in bimolecular crystals and the evolution of both forms can be revealed from Raman spectra as a function of varying PCBM loading and excitation energy. Figure 5b presents estimates of the disordered PBTTT content in as-cast blends, which increases with PCBM content and excitation energies. For comparison, $((I_7)/(I_6+I_7))$ values were determined for an annealed blend (1:4 w/w) and displayed in Figure 5b, which has significantly less of the disordered PBTTT because of conversion into bimolecular crystals which is consistent with REP trends in Figure 4 and corresponding plots of $(I_7)/(I_6+I_7)$ values confirm this behavior (not shown).

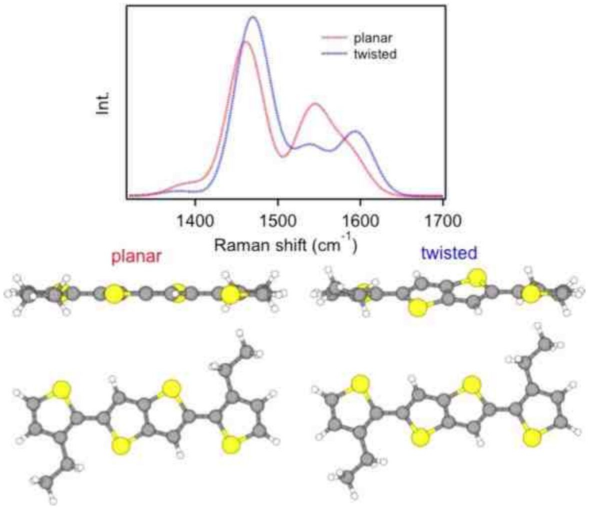

Figure 6.6 Simulated Raman spectra of the BTTT-C2 monomer and structures.

6.2.3 Theoretical Raman Simulations

DFT Raman simulations of a planar and twisted PBTTT model monomer system (BTTT-C2) are next performed to validate our proposed model and are shown in Figure 6 with their respective structures. Calculated DFT Raman line shape trends agree very well with experiment although non-resonant conditions are used in simulations and a scaling factor of 0.95 must be applied to calculated frequencies in order to compare with experiment. The nominal C−C symmetric stretch appearing at 1461 cm^{-1} for the planar conformation undergoes a blue shift of ~7 cm^{-1} in the twisted variant. Most notably, intensity redistributions occur between the inter-ring C=C symmetric stretch (1541 cm^{-1}) and the thiophene C=C stretch (1594 cm^{-1}) depending on backbone planarity. For example, the latter increase in intensity for the twisted BTTTC2 variant whereas the former dominate in the planar monomer. Previous DFT simulations of planar and twisted PBTTT trimer structures show similar trends as presented in Figure 640 confirming that at least two PBTTT types are present in PCBM blends revealed from PCBM loading- and excitation energy dependent Raman spectra. Moreover, calculated frequencies and intensities of trimers were very similar to experimental Raman spectra, suggesting that excitations are probably localized to a few monomer units.

Thus far we have shown that the ability of the two species model to decompose key Raman bands into separate contributions from morphology-dependent PBTTT conformers offers a much simpler means to assess order/disorder transitions in this system. Although DFT simulations predict observed experimental behavior, they do not allow us to incorporate side group disorder and paracrystallinity. It is also important to note that ordered PBTTT chains in bimolecular crystals are twisted but side group disorder should be diminished relative to the kinetic disordered intercalated form.

6.2.4 Spatially Mapping Order−Disorder and Photocurrent Generation in Solar Cells

Despite the relatively poor performance of PBTTT/PCBM, we have thus far demonstrated its value as a model for understanding donor/acceptor interactions and supramolecular organization and their impact material performance. Resonance Raman spectroscopic and photocurrent imaging techniques are now employed to spatially resolve how ordered and disordered PBTTT chains impact local device performance in model solar cell devices. For these experiments, as-cast and annealed PBTTT/PCBM blends in 1:4 w/w ratios (the optimal blend ratio reported for solar cells)[200,201] were prepared to compare morphology-dependent order/disorder spatial distributions. Because these studies emphasize model PBTTT/PCBM morphologies, power conversion efficiencies were <1% but nonetheless show good stability and expected diode-like behavior. We emphasize annealed devices because of better material performance in addition to better contrast in Raman and photocurrent images.

Figure 7 shows representative resonance Raman and photocurrent images of a 1:4 w/w annealed device and appreciable microscopic phase segregation is apparent within the active layer. Raman images represent the ~1489−1500 $\mathrm{cm^{-1}}$ spectral region of the thiophene C=C stretches and are generated using 458 nm (2.71 eV) excitation light. This excitation energy was specifically chosen to selectively interrogate disordered PBTTT chains and their spatial locations relative to ordered chains in bimolecular crystals. Because charge transfer and recombination processes are strongly dependent on local polymer ordering and composition we expect significantly different responses for each PBTTT form[217,218]. Figure 7a presents the total integrated intensity of the ν6, 7 modes and corresponding photocurrent over the same area is shown in Figure 6b. Lower PBTTT intensity represents PCBM-rich areas, but an appreciable amount of PBTTT still exists in these regions indicating these are most likely bimolecular crystals. Because the PCBM loading of these devices is high (1:4 w/w), it is unlikely that PBTTT completely phase separates meaning the entire film corresponds to ordered and disordered mixed phases. Photocurrent images (Figure 7b) show much lower output in putative bimolecular crystal regions probably originating from unbalanced charge transport as expected from increased charge recombination[219,220]

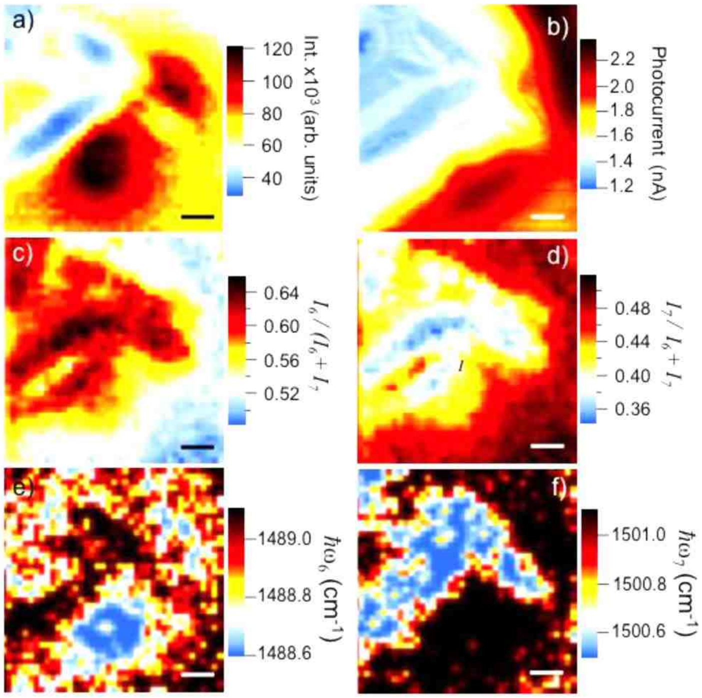

Figure 6.7 (a) Total integrated Raman intensity of C=C symmetric stretching mode (ν6, 7) and (b) corresponding photocurrent images of annealed PBTTT/PCBM (1:4 w/w) device (excitation energy =2.71 eV). (c, d) Ratios and (e, f) frequency dispersion of ordered (ν6) and disordered (ν7) PBTTT species, respectively. A ± 5% tolerance was applied for determining the center frequencies of each PBTTT component. Scale bar = 2 μm.

The PBTTT thiophene C=C stretch is now decomposed into its constituent components and Figures 7c,d shows fractional compositions of ordered $((I_6)/(I_6+I_7))$ and disordered $((I_7)/(I_6+I_7))$ forms, respectively, using the same procedure described above. Comparison of these images with morphology-dependent frequency dispersion characteristics (Figure 7e, f, respectively) confirm that bimolecular crystals are indeed most concentrated in PCBM-rich regions (i.e., lower PBTTT intensities, Figure 7a). Although Raman signatures for PCBM are absent, direct excitation may lead to photocurrent from hole transfer to PBTTT from photoexcited PCBM. We measured photocurrent images on the same devices using 488 nm (2.54 eV) light, which is near the PBTTT absorption maximum, but identical behavior is observed. The effects of excitation intensity and PCBM crystal size (annealing time) on local photocurrent production were also investigated and no significant differences were found. Interestingly, maximum photocurrent generation originates from regions with more disordered PBTTT content. We speculate that increased geminate charge recombination dominates in bimolecular crystals, which is consistent with previous TAS studies of PBTTT/PCBM thin films predominantly in the bimolecular crystal phase.

Raman and photocurrent images of as-cast PBTTT/PCBM (1:4 w/w) devices were also measured under the same conditions as annealed devices. These devices generally show relatively uniform morphological features and photocurrent is at least an order of magnitude smaller than annealed devices when illuminating with a diffraction-limited laser spot.

Resonance Raman and photocurrent images have so far demonstrated that morphology-dependent variations in material performance are determined not only from the type and amounts of PBTTT species but also their spatial distributions in the device active layer. Intensity modulated photocurrent spectroscopy (IMPS) and imaging is next used to expose how specific conformers and morphologies impact loss mechanisms in PBTTT/PCBM devices, namely, charge recombination.

IMPS uses a small (~10%) sinusoidal modulation of the excitation source and the frequency is swept over several decades (typically, ~0.1 Hz up to ~1 MHz). Figure 8 shows IMPS ensemble spectra from annealed (Figure 8a, c) and as-cast (Figure 8b, d) PBTTT/PCBM (1:4 w/w) solar cells recorded by using a wide field configuration that illuminates the entire device active area (~20 mm2). Ensemble IMPS sweeps show similar behavior as reported previously in related polymer/fullerene solar cells and a characteristic maximum is observed in photocurrent sweeps and the phase decreases significantly in this region toward its maximum (−180°). Photocurrents in the low frequency regime (<1 kHz) are almost entirely real and phase shifts are positive (<10°)

for annealed devices indicating that charge carriers lead the modulation frequency. On the other hand, as-cast films typically show lower photocurrents and phase shifts start at ~ 0°. At larger modulation frequencies, both devices show increasingly negative phase shifts due to charge carriers lagging behind the modulation frequency.

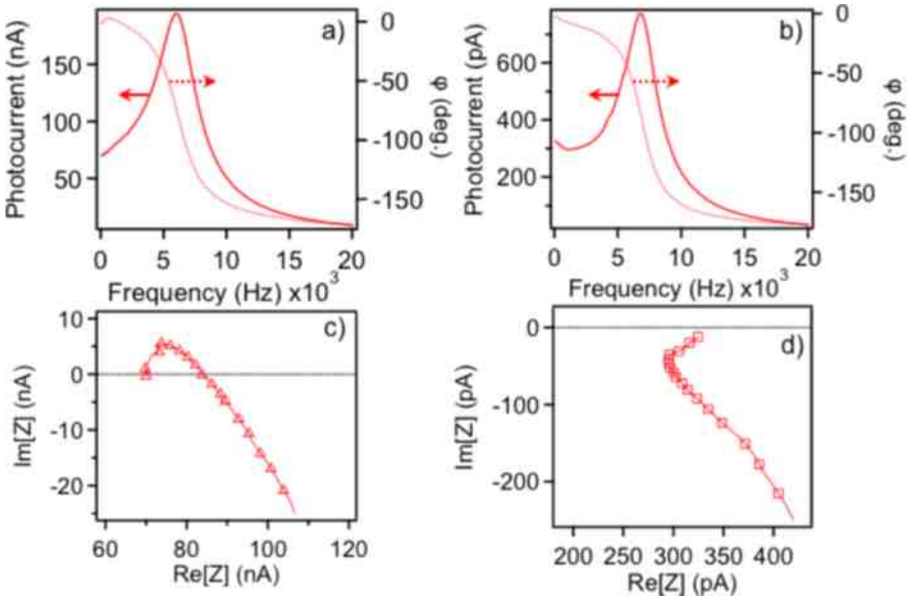

Figure 6.8 IMPS spectra (photocurrent and phase shift, φ) and Nyquist (complex) plots of (a, c) annealed and (b, d) as-cast PBTTT/PCBM (1:4 w/w) solar cells, respectively.

Seminikhin and co-workers first reported positive phase shifts at low modulation frequencies or, a component in the first quadrant of the complex (Nyquist) IMPS plot from P3HT/PCBM devices[206]. This feature has been attributed to non-geminate charge recombination that becomes more pronounced as the device ages. Luther and co-workers recently advanced this understanding by systematically studying device aging and preparation conditions and tracking IMPS responses[207]. These authors showed that first quadrant photocurrent contributions in Nyquist plots, result from the formation of deep traps and introduced a drift-diffusion model to account for this behavior[207]. The observation of positive phase shifts in the low-frequency modulation regime demonstrates that non-geminate recombination processes become operative in annealed PBTTT/PCBM devices indicating suppression of prevailing geminate recombination. The lack of this signature in as-cast devices (either fresh or aged) supports this view because geminate processes occur on faster time scales beyond what is currently accessible by IMPS techniques. Nonetheless, our ability to spatially correlate the specific PBTTT phase to local photocurrent production can be leveraged to map recombination sites or zones to morphological boundaries using a hybrid IMPS imaging approach.

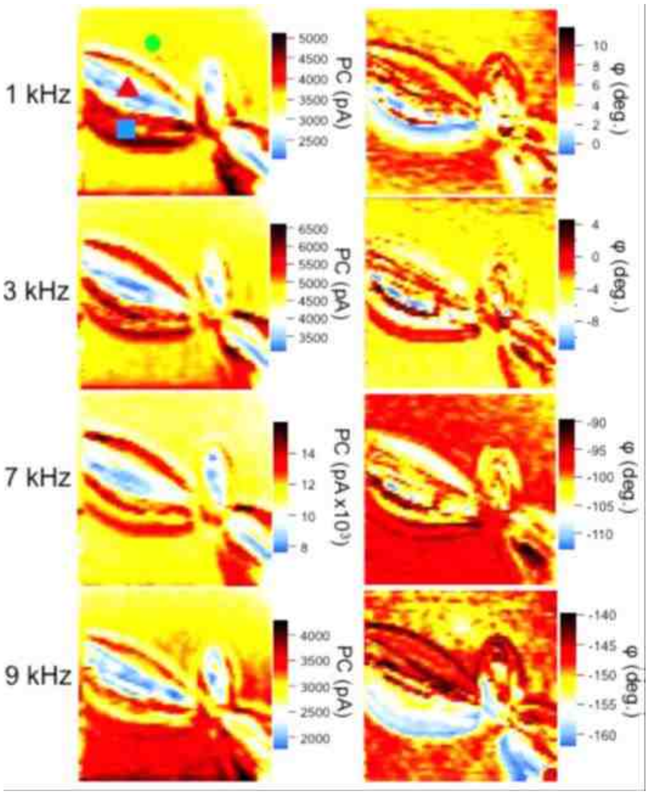

Figure 6.9 IMPS photocurrent (left) and phase shift (φ, right) images of same area at 1 kHz, 3 kHz, 7 kHz, 9 kHz laser modulation frequency of annealed PBTTT/PCBM (1:4 w/w) device (excitation energy = 2.54 eV). Image scan area = 400 μm^2.

IMPS images were generated using the same high NA objective used for Raman and quasi-DC photocurrent images and are shown in Figure 9. Scan ranges were expanded to 20 × 20 μm and laser modulation frequencies were held fixed throughout the scans using similar power densities as the quasi-DC photocurrent images shown in Figure 7. Several modulation frequencies were selected representing different charge transport and recombination regimes observed in ensemble IMPS spectra, namely, low frequency (e.g., 1 and 3 kHz), near the maximum frequency photocurrent (~7 kHz) and at the high-frequency regime (~9 kHz). PBTTT/PCBM blends were annealed for longer times in order to achieve greater phase separation that allows us to better resolve distinct phase boundaries. Similar to quasi-DC Raman and photocurrent images shown in Figure 7, bimolecular crystals in Figure 9 produce lower photocurrent output than the surrounding mixed phase. From the IMPS phase shift (φ) images, positive phase shift accumulates on the periphery of these regions. As the modulation frequency increases past the maximum, IMPS images lose contrast owing to carriers lagging behind the modulation. We infer that boundaries surrounding regions of positive phase shift (or, relative positive phase shift at higher modulation frequencies) represent recombination zones for non-geminate processes since separated electron−hole carriers can diffuse away from the interface before becoming trapped. In this case, trap sites are probably located at phase boundaries between ordered and disordered PBTTT regions, which is consistent with the current and phase maps (Figure 9). Despite loss of resolution at higher modulation frequencies, these results in general show that lateral diffusion effects are probably not significant since features of size scales comparable to the diffraction limit are resolvable.

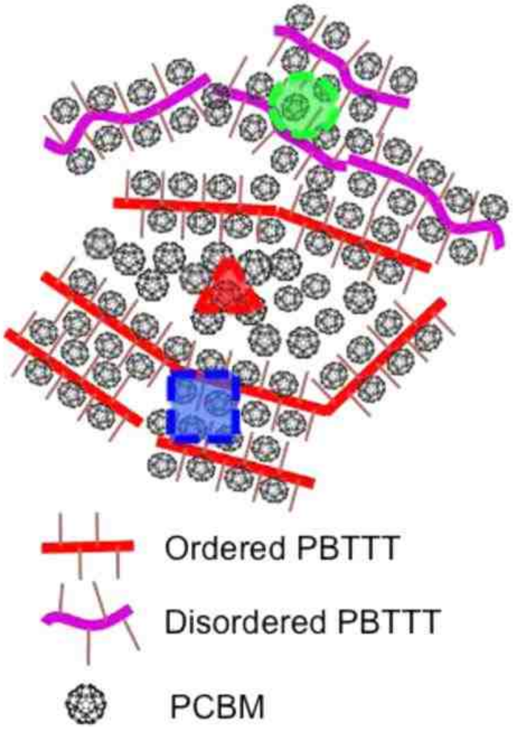

Figure 6.10 Proposed Morphology-Dependent Compositions in PBTTT/PCBM Films Shown in Figure 9 (see corresponding symbols in 1 kHz current image, top left)

On the basis of optical and Raman spectra of pristine PBTTT and PCBM blends, small energetic differences between ordered and disordered PBTTT species imply that charge traps are mostly shallow in nature. Troisi and co-workers reported "self-healing" phenomena occur in pristine PBTTT where facile de-trapping of charges occurs due to small structural changes (~k_BT)[204]. However, greater disorder in blends probably results in deeper traps, which is evident from IMPS results. Although it is unclear if a similar self-healing mechanism is conceivable in PBTTT/PCBM solar cells, effective management of order−disorder boundaries through new molecular-level organization strategies may help overcome detrimental trapping effects.

6.3 Conclusions

We have shown that resonance Raman spectroscopy of PBTTT/PCBM blends can be used in a straightforward manner to extract the relative amounts of ordered and disordered PBTTT conformers. Both ordered and disordered components exist in a mixed phase but, the former are found in bimolecular crystals whereas the latter correspond to precursors of the ordered forms. The larger frequency and line width of disordered chains likely originate from greater side group disorder and highly twisted monomer thiophene rings due to disordered alkyl side groups. DFT simulations and excitation energy dependent Raman spectra supported this assignment although we point out that previous studies have shown that PBTTT chains in the bimolecular crystals also tend to twist around the intercalated fullerene but side group and paracrystalline disorder is reduced. This common structural trait shared between ordered and disordered PBTTT chains localizes excitations, hence, the invariance of Raman overtone-combination intensities with PCBM loading. Resonance Raman and photocurrent images next expose the morphology dependence of intercalation-induced order/disorder and its influence on local current generation. IMPS spectra and images showed evidence for increased non-geminate recombination at the boundaries between bimolecular crystals and disordered mixed zones. Overall, these experiments help bridge the gap in understanding of how ground-state structure and acceptor interactions influence the outcomes of excited state photovoltaic processes.

Chapter VII

Effect of Ionizing Radiation Exposure on the Stability and Performance of Polymer/Fullerene Solar Cells

7.1 Introduction

Solar cells based on blend thin films of conjugated polymers and soluble fullerene derivatives have seen significant improvements in performance and stability in recent years. Device packaging technology, in particular, has extended lifetimes by excluding oxygen and moisture leading to photodegradation usually mediated by low-lying triplet or charged defect states. Although polymeric solar cells have tremendous advantages for terrestrial applications mostly in terms of cost and ease of processing, there is now increasing interest for employing these devices to power small space vehicles (e.g., cube satellites). Unlike conventional inorganic solar cells, the intrinsic lightweight and flexibility of polymer solar cells makes them attractive as power sources despite their intrinsically lower power conversion efficiencies. However, it is not yet clear if design rules developed for terrestrial applications (i.e., AM1.5 conditions) will directly translate into acceptable performance for space applications. For example, strategies for harvesting a greater fraction of NIR photons have extended polymer/fullerene solar cell power conversion efficiencies (PCE) beyond 10%. The greater flux of UV-vis photons under AM0 conditions encountered in low Earth orbits offers new opportunities for harvesting these photons, in addition to NIR photons. Before polymer solar cells can be introduced as low-cost alternative to space vehicle power sources, a detailed knowledge of stability in space environments is required. In particular, repeated exposure to high-energy ionizing photons, energetic protons and electrons as well as large temperature fluctuations may result in irreversible chemical and morphological changes that degrade performance to unacceptable levels.

Thin film solar cells of poly(3-hexylthiophene) (P3HT) and [6,6]-phenyl-C_{61}-butyric acid methyl ester (PCBM) (1:4 w/w) blends are excellent benchmarks for understanding ionizing radiation effects on organic active layers because of their well-characterized structure-function relationships. The semi-crystalline nature of both components also facilitates spectroscopic studies and correlations between morphology and performance and their changes with ionizing radiation exposure. Earlier studies on P3HT/PCBM devices found significant performance degradation upon X-ray irradiation, which was proposed to originate from space charge regions near the cathode. Street et al. further investigated radiation effects on P3HT/PCBM and other solar cells over a broad spectral range (i.e., X-ray up to NIR wavelengths) and proposed that hydrogen abstraction on the solubilizing alkyl side chains of the polymer as the primary degradation outcome[221]. These authors further noted this mechanism is reversible based on restoration of pristine device performance levels by post-irradiation annealing treatments. However, it is not yet clear how the heterogeneous morphological landscape of polymer/fullerene blends influences radiation-induced degradation mechanisms and their efficacies. For example, the blend composition varies greatly over the entire material which should modulate degradation pathways and kinetics. Because morphological characteristics also change with temperature and time, extracting reliable mechanistic details of degradation processes can often be fraught with many pitfalls. In order to both understand and possibly mitigate chemical and morphological changes in response to ionizing radiation exposure, morphology-sensitive physical probes are required to correlate the blend structure and composition to performance characteristics.

The primary motivation for our present study is to ascertain the response and stability of distinct blend morphologies to ionizing radiation exposure up to 1 Mrad. In particular, we are interested in characterizing the response of specific P3HT polymorphs (i.e., aggregates and amorphous chains) as well as local blend composition (i.e., PCBM content) to varying dosages of X-rays. The miscibility characteristics of PCBM in each of these forms (i.e., well-mixed amorphous P3HT/PCBM regions and complete exclusion from pi-stacked P3HT aggregates) will be further exploited to understand how morphological features are affected by radiation exposure. Because X-rays are not resonant with valence electronic transitions involved in photovoltaic processes (i.e., charge generation and transport), it should be possible to interrogate device performance changes while the cell is still operational. It is also noteworthy that recent studies have found evidence of cross-linking in P3HT thin films[222] in addition to alterations in PCBM crystallinity possibly from degradation of the C60 cage from prolonged X-ray exposure[223]. In the following, we attempt to bridge the gap in understanding of possible degradation pathways between pristine and blend solar cell materials, which are expected to significantly different due to the miscibility characteristics in various P3HT polymorphs. Both conventional (e.g., current density-voltage (J-V) measurements) as well as more specialized experimental techniques, such as intensity modulated photocurrent/photovoltage spectroscopy (IMPS/IMVS), to assess the response of carrier extraction and recombination kinetics to radiation exposure. These frequency domain measurements are particularly useful for resolving interfacial versus bulk charge recombination processes, which have different intrinsic kinetics and possibly different degradation mechanisms from ionizing radiation exposure. Resonance Raman spectroscopy and imaging are next used to identify and map the local composition of the P3HT/PCBM blend within the device active layer that can be directly correlated to device performance metrics. This technique is particularly effective for discerning blend composition and stability by taking advantage of strong resonance enhancements of the

P3HT Raman scattering cross-sections that also reveals local PCBM content due to its miscibility characteristics in different polymer conformers.

7.2 Results and Discussion

We examine radiation-induced degradation mechanism(s) and the role of the polymer/fullerene blend active layer morphology. Figure 1a shows a typical current density-voltage (J-V) of an annealed P3HT/PCBM solar cell device before and after exposure to X-ray radiation up to ~1 Mrad accumulated dosage. The typical rates of exposure used here were larger than those reported earlier in Ref. 1, however, smaller rates lead to similar responses (vide infra). Devices were annealed lightly to optimize morphologies and performance figures of merit (i.e., open-circuit voltage, V_{OC}, short-circuit current, J_{SC}, fill factors, FF, and power conversion efficiencies, PCE). These figures of merit were monitored in-situ, which all display gradual decreases with increasing accumulated dosage. Prior to irradiation, all devices show characteristic diode-like behavior with FF and PCE values of ~35-50% and ~1-3%, respectively (see Supporting Information). These values are lower than conventional P3HT/PCBM solar cells fabricated on thicker quartz substrates due to our need of thinner substrates to facilitate spectroscopic and current imaging experiments.

Following up to 1 Mrad dosages, pronounced losses of ideality and ‘s-curve’ character become apparent in all devices. This type of change in the I-V profile for OPV devices has been seen with extended illumination; that is, this behavior is similar to the normal mechanisms of device degradation over long periods of exposure to sunlight[224]. This effect has been previously assigned to alterations in charge extraction efficiencies at the cathode[225] from either interface layers or migration of fullerenes away from this contact. The latter suggest morphological changes in the blend thin film or modification of device contacts. Reductions in short-circuit current densities (J_{SC}) are also apparent, however, previous irradiation studies of P3HT/PCBM solar cells by Kouhestani et al. demonstrated similar trends but concluded that carrier generation rates are not significantly affected[226]. These authors further observed that the open-circuit voltage (V_{OC}) and carrier lifetime are particularly susceptible to X-ray exposure[227]. For comparison, Figure 1b shows V_{OC} values as a function of accumulated radiation dosage for several annealed devices with different PCEs. Because V_{OC} values are sensitive to the polymer/fullerene interface morphology (i.e., carrier recombination), the rate of change in this parameter with radiation exposure reflects the effect of bulk film morphology on the rate of degradation. Devices with larger V_{OC} values (>0.45 V) show V_{OC} degradation rates of -1.4×10^{-3} V/krad on average compared to -1.6×10^{-3} V/krad for devices with V_{OC} <0.45 V. Blend films with non-optimal morphologies (e.g., larger fractions of purified polymer and fullerene components) have lower V_{OC} values and shunt resistances. We propose that purification of P3HT/PCBM components from crystallization increases susceptibility to degradation by exposure to ionizing radiation (vide infra). Although V_{OC} degradation rates are not substantially different between solar cells, poorer performing devices (i.e., non-optimized blend morphologies) tend to degrade faster on average with X-ray irradiation.

For terrestrial solar cell applications, bypassing oxygen-related photodegradation processes involves rapid deactivation of polymer excited states before singlet oxygen sensitizing triplet states are populated. The relatively close proximity of fullerenes to conjugated polymers (depending on morphology) in solar cell blends leads to nearly quantitative photoinduced charge transfer which can bypass many photodegradation processes on slower time scales. However, very little is currently understood about the sensitivity of degradation mechanisms to the inhomogeneous morphological landscape of photovoltaic polymer/fullerene blends under AM0 operation and in oxygen-free environments. This task is further complicated by the non-resonant nature of ionizing radiation, i.e., photovoltaic processes need not be active for device degradation to occur.

Figure 7.1 shows J-V curves of representative annealed (a) and as-cast (b) P3HT/PCBM devices under dark and AM1.5 conditions. In the latter, there is a larger fraction of a well-mixed polymer/fullerene and the overall aggregate content of P3HT and PCBM are smaller. Beginning with poorer performing as-cast devices, pronounced s-curve character is present that increases in severity with radiation dosages up to 1 Mrad. Overall, as-cast P3HT/PCBM devices exhibit similar degradation trends as annealed devices suggesting little dependence on device processing conditions and morphology.

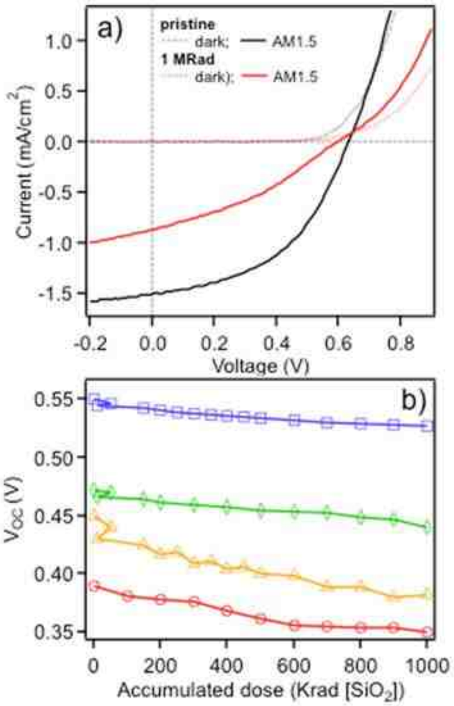

Figure 7.1 (a) Current-voltage (J-V) curves of typical P3HT/PCBM devices before (black) and after (red) exposure to ionizing radiation. b) Responses of several devices with accumulated radiation dosage illustrating the effect of device-to-device variation

Interestingly, Street and co-workers found that post-irradiation annealing treatments could recover device performance metrics to nearly their pristine values[221]. This result indicates that the degradation mechanism is reversible but it was not clear if recovery characteristics were predetermined by blend processing conditions (i.e., bulk morphology). Both as-cast and annealed P3HT/PCBM solar cells were subjected to post-irradiation thermal annealing treatments to assess the nature of the degradation mechanism(s), reversibility and its dependence on morphology. Devices annealed prior to irradiation showed virtually no recovery with post–irradiation annealing (see Fig. 2a) whereas as-cast films improved to levels similar to pristine annealed devices prior to irradiation. Additional irradiation exposures and post annealing treatments were performed on the recovered as-cast devices but no significant recovery was observed following subsequent post-irradiation annealing treatments. This result indicates that, unlike earlier findings, degradation is irreversible and morphology-dependent.

Putatively, we conclude that radiation exposure leads to irreversible defect formation in blends with larger amounts of purified phases (i.e., P3HT or PCBM crystalline aggregates). Significant reductions in V_{OC} and carrier lifetimes also point to enhanced charge carrier recombination yields assuming that no changes in the absorption band edge energies are invariant of radiation exposure. It is not possible, however, to conclusively determine if changes occur in the bulk or at contact interfaces from J-V curves alone. As an interesting note, pristine as-cast devise show a pronounced “s-curve” which has been attributed to a potential barrier charges must overcome for extraction[228], and this barrier disappears with annealing due to crystallization of the PCBM component alone[229]. This type of behavior reoccurs with high doses of radiation, and with extended exposure of devices to AM1.5 conditions.[224]

Charge recombination processes occur over a broad range of time scales (i.e., geminate recombination, ~100 ps up to ~100 ns, and non-geminate recombination, >1 μs) and the branching ratios heavily influenced by film morphology characteristics. For example, non-geminate recombination processes have been shown to dominate in annealed devices due to greater phase separation and formation of deep charge traps that become greater in density as the device ages. The identities of these deep trap species are typically byproducts of oxidative damage, which are not expected to be significant upon irradiation.

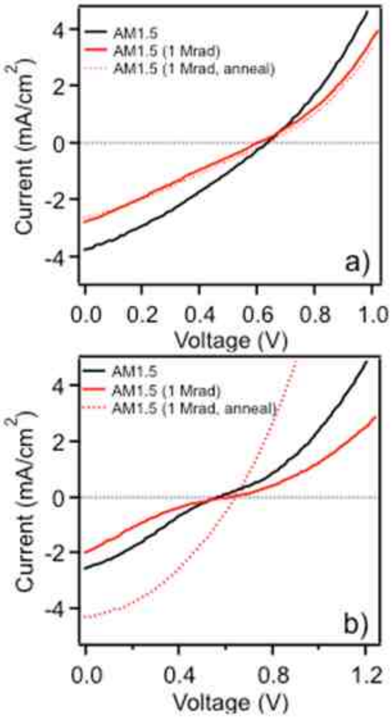

Figure 7.2 Current-voltage (J-V) curves of annealed (a) and as-cast (b) P3HT/PCBM devices before (black) and after (red) exposure to ionizing radiation (1 MRad). Dotted traces depict J-V curves of each type following a post-irradiation annealing treatment

Intensity modulated photocurrent and photovoltage spectroscopy (IMPS/IMVS) techniques are now used to determine if deep trap formation and non-geminate recombination accompanies radiation-induced performance degradation. Figure 3 shows IMPS spectra of an annealed P3HT/PCBM solar cell before and after irradiation. Similar experiments performed on as-cast devices were hampered by low photocurrent outputs often near the detection limit (~1 pA), which made it difficult to reliably compare the two device types. Because of the irreversible nature of irradiation-induced degradation due to greater phase purity in these blends (vide supra), we choose to focus on annealed devices. As the modulation frequency increases from ~DC levels, the photocurrent reaches a maximum at a characteristic drive frequency, f_{max}, and then gradually decreases at higher frequencies. Complex (Nyquist type) IMPS plots are shown in Fig. 3b representing the imaginary (quadrature) and real (in-phase) contributions to the photocurrent output. Earlier IMPS studies by Byers et al. and Set et al. on P3HT/PCBM solar cells reported positive phase shifts of the photocurrent output in both Bode and Nyquist plots at low modulation frequencies (e.g., <1 KHz)[206,207]. These features were assigned as signatures of non-geminate charge recombination that become more pronounced as the device ages, consistent with increased trap levels. From Fig. 3, IMPS responses of all irradiated P3HT/PCBM solar cells showed no significant accumulation of positive phase shift with irradiation up to 1 Mrad. This result suggests that non-geminate recombination yields are not large in the bulk blend material even in cases when photocurrent outputs decrease substantially because of exposure to large doses of ionizing radiation. In addition, small blue-shifts in f_{max} (~100-300 Hz) are apparent indicating changes in charge extraction kinetics, device geometric capacitance (i.e., RC time constant), or shunt resistance. By comparison IMPS responses from P3HT/PCBM solar cells annealed for long times (>30 min) show large red-shifts of f_{max} and losses in photocurrent upon irradiation. We propose that changes in IMPS spectral shapes are consistent with degradation in the vicinity of device contact interfaces as opposed to degradation of the polymer/fullerene interface, which is in agreement with Kouhestani et al. who found no change in charge generation rates (i.e., no degradation of P3HT/PCBM interfaces)[230].

Additional perspectives of radiation-induced changes in device performance can be obtained using IMVS measurements. Figure 4a depicts IMVS sweeps of pristine and irradiated P3HT/PCBM devices with the photovoltage magnitude (R) and phase as a function of drive frequency. Photovoltages are nearly the same for both pristine and irradiated devices that decrease to zero with increasing light modulation frequency. An approximation of the pseudo first order carrier lifetime (i.e., the inverse recombination rate constant) can be estimated from the minimum of the imaginary photocurrent component. We find that carrier lifetimes increase in irradiated devices although the scan range was limited due to lower signal-to-noise ratios at higher frequencies. These trends contradict earlier findings from analyses of V_{OC} with irradiation that show diminished carrier lifetimes following irradiation. This feature may result from increased charge screening that may suppress recombination processes. Photovoltage phase shifts show starkly different behaviors between pristine and irradiated devices. Pristine devices show decreases of the photovoltage with and phase shifts are ~90° over the entire modulation frequency range which is consistent with the expectation that a polymer solar cell can be approximated as an RC circuit below frequencies of ~10 KHz. In this scenario, voltage lags current by 90° and deviations from this simple approximation are indicative of non-ideality. Changes in IMVS spectra behaviors with irradiation are much more drastic with larger photovoltage phase shifts at ~DC levels that relax to similar values as pristine devices at high frequencies. Polar plots of the photovoltage magnitude and phase shift are shown in Figure 4b that accentuate the differences in IMVS responses from pristine and irradiated devices. Similar to the photovoltage magnitudes in Fig. 4a, photovoltages decrease towards zero and phase shifts converge toward ~90°. This behavior represents a significant departure from ideal behavior and is indicative of an additional charge storing mechanism. Comparing f_{max} values of the imaginary IMVS component reveals insights of the carrier recombination rates where, similar to IMPS, the imaginary IMVS higher frequencies in irradiated devices reflect faster carrier recombination rates. Shifts in f_{max} and response characteristics in both IMPS and IMVS with irradiation indicate that the most detrimental effect of irradiation occurs near the electrode contacts although the contribution increases with drive frequency and shifts in the maximum value toward exact nature of degradation is not entirely clear.

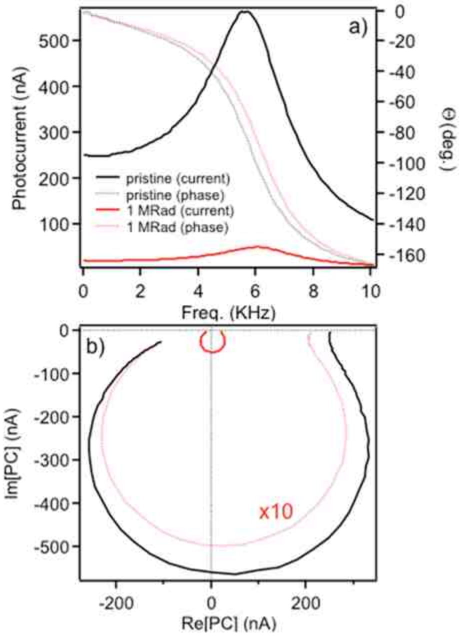

Figure 7.3 Intensity modulated photocurrent spectroscopy (IMPS) Bode (a) and Nyquist (b) plots of annealed P3HT/PCBM devices before (black) and after (red) exposure to ionizing radiation (1 Mrad). The phase of the modulated photocurrent signal in (a) is depicted as dotted traces.

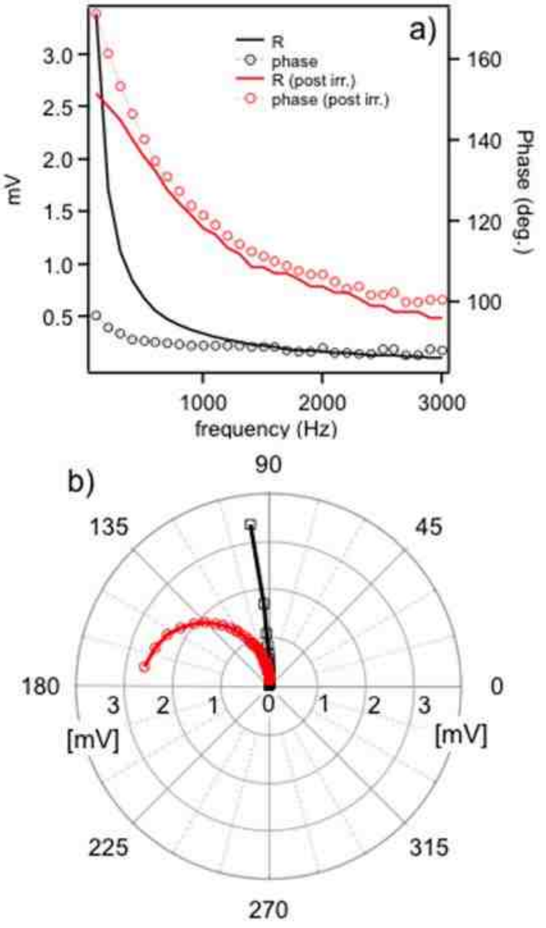

Figure 7.4 (a) Intensity modulated photovoltage spectroscopy (IMVS) Bode plots of annealed P3HT/PCBM devices before (black) and after (red) exposure to ionizing radiation (1 MRad). B) Polar plot of photovoltage and phase shift, blue arrow shows direction of increasing frequency.

We now use resonance Raman spectroscopy and imaging to identify and map specific structural polymorphs and morphological features to verify if significant material degradation is responsible for behaviors observed in Figs. 1-4. Previous studies by Street et al. assigned radiation-induced changes in device performance to proton abstraction on the alpha methylene group to the thiophene ring that can be restored upon annealing[221]. External quantum efficiency (EQE) measurements also revealed a weak feature coinciding with the red edge of the polymer optical absorption lineshape resembling a charge transfer transition. This feature was proposed arise from proton abstraction and appeared regardless of the incident photon energy. If a substantial number of abstraction events occurred as a result of irradiation, then large changes in Raman signals should be manifest due to disruptions in P3HT conjugation length and conformations. Changes in mesoscale blend morphology have been reported as well possibly from local heating but without significant changes in the packing of P3HT and PCBM components. Vaselabadi et al. also recently found that exposure to X-ray radiation can induce cross-linking in pristine P3HT aggregates, which are more prevalent in annealed P3HT/PCBM blends[222]. Resonance Raman spectroscopy is highly sensitive to the packing state of P3HT and can, in principle, uncover the nature of degradation in our devices and if bias exists toward either aggregates (PCBM-depleted) or amorphous (PCBM-rich) P3HT chains.

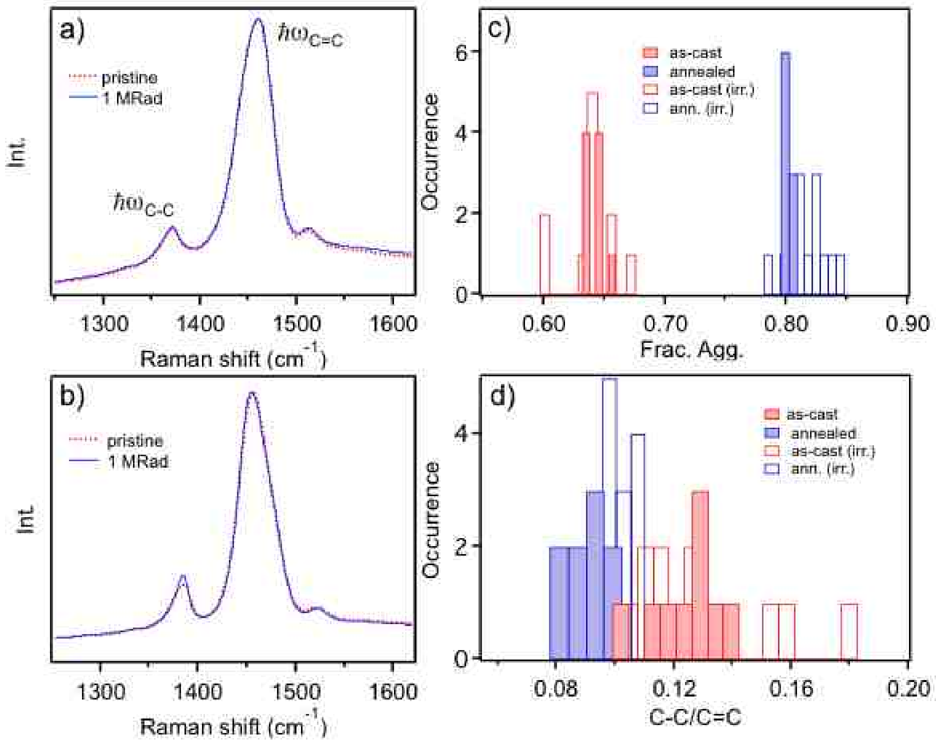

Figure 7.5 Averaged Raman spectra of as-cast (a) and annealed (b) P3HT/PCBM devices in the main CC skeletal backbone region before (dotted red trace) and after (blue solid trace) irradiation. c) Fraction of aggregates determined from decomposition of the P3HT C=C symmetric stretching band (~1450 cm^{-1}) and d) C-C/C=C integrated intensity ratios for as-cast (red) and annealed devices before (solid) and after (open) irradiation.

Raman spectra of P3HT/PCBM blends were acquired by raster scanning a diffraction-limited laser excitation spot within a functioning device and acquiring a spectrum at each point over the entire field-of-view (~100 μm^2) typically. Figure 5 shows ensemble averaged Raman spectra from these scans (~1000 individual spectra) of as-cast (a) and annealed (b) P3HT/PCBM devices in the region of the P3HT symmetric CC backbone stretching modes (~1450-1470 cm^{-1}) for both pristine and irradiated samples. By resonantly exciting both aggregated and amorphous P3HT forms equally (488 nm), the relative amounts of either form can be estimated by decomposing the C=C symmetric stretch band using a procedure described in detail earlier. Although it is not currently possible to measure the same area before and after exposure to ionizing radiation in our microscope system, comparisons of multiple devices (averaged over all possible morphological forms) can reveal if significant structural changes or deformations occur. Fig. 5c plots the fraction of aggregated P3HT in the blend for up to 10 as-cast and annealed devices before (solid) and after irradiation (open). The fraction of P3HT aggregates in as-cast devices show virtually no change with irradiation whereas a small increase an overall aggregate content is observed for annealed films (~2.5%). Comparisons with shielded devices (i.e., devices on the same substrate but not directly irradiated) produced broader distributions of aggregate content making it difficult to reliably assess whether this increase is the result of radiation-induced cross-linking.

Earlier studies by our group also found that ratios of the C-C (~1380 cm^{-1}) and C=C intensities are correlated with aggregate packing order within these structures (i.e., larger C-C/C=C ratios indicate greater monomer planarity). Fig. 5d shows plots of C-C/C=C intensity ratios from as-cast and annealed devices before and after irradiation. Although average C-C/C=C ratios are similar in both devices probably due to the relatively short annealing times used, small increases are apparent in annealed devices following irradiation. This result is consistent with the slight increase in aggregate content shown in Fig. 5c. If cross-linking occurs, it is expected that pi-stacked P3HT should have greater predisposition for this process owing to the close proximity of the conjugated backbones (3.8 Å).

Resonance Raman spectra indicate that minor structural changes occur with irradiation but extracting the exact identities of degradation products is not possible with on-resonance excitation. It is important to note that strong resonance enhancement effects may obscure minor degradation and small structural changes and deformations occurring in a minority fraction of the material. These changes may be difficult to resolve spectroscopically, despite that even small defect densities can result in large alterations in device performance with accumulated radiation dosages. To determine if resonance effects dominate the responses shown in Fig. 5, we measured Raman spectra off resonance with allowed P3HT optical transitions, which drastically reduces selectivity thus revealing contributions of all other material components within the device. Figure 6 shows Raman spectra of pristine and irradiated (1 MRad) P3HT/PCBM solar cells excited at 785 nm. These 'off resonance' spectra are much more congested and significant broadening of CC stretching modes occurs due to contributions from the PCBM and PEDOT–PSS components. Nonetheless, we do not find evidence for substantial degradation, such as new transitions from degradation products. We conclude that probably only minor alterations of the P3HT component occur, which are most likely to result from proton abstraction or cross-linking in aggregated regions.

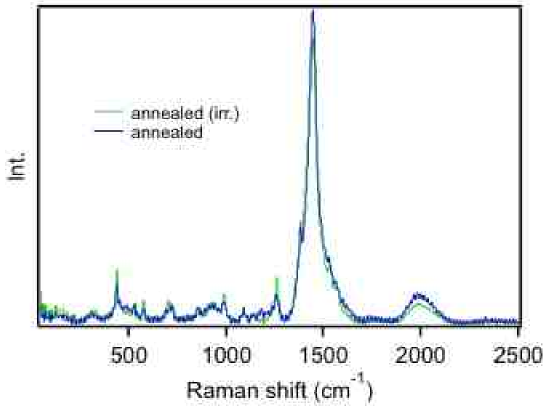

Figure 7.6 Off resonance Raman spectra of device films showing enhancements of several peaks not associated with the donor polymer. These peaks are most likely associated with the PCBM component of the thin film.

We have demonstrated that degradation of P3HT/PCBM device performance with irradiation depends on their morphological attributes (i.e., processing conditions). It is further apparent that increased phase purity leads to greater susceptibility to radiation damage most likely owing to the close-packed nature of polymer chains and fullerenes. The irreversible nature of radiation-induced damage observed in annealed devices supports the view of a greater fraction of polymerized PCBM or, as a minority, cross-linked P3HT chains.

Recent evidence for cross-linking in P3HT aggregates with X-rays has been demonstrated by Vaselabadi et al. that was inferred indirectly from solubility tests following exposure to X-rays (up to 10 J/cm^2) [222]. On the other hand, P3HT is inherently more stable when mixed with PCBM because of its radical scavenging qualities, which are advantageous for bypassing oxygen sensitizing triplet excited states[231,232]. In well-mixed phases device failure usually proceeds due to PCBM oxidation or degradation of the PCBM/metal interface[224,233]. This type of irreversible material degradation is consistent with the permanent damage observed in devices annealed for long times and is consistent with irreversible damage seen by Voroshazi *et al*. in aged devices which they attribute to degradation of PCBM and an insulating interface at the metal/acceptor contact[224]. Post-irradiation annealing treatments should therefore have little impact on performance since the film is essentially frozen in its most stable morphological state.

Although quantitative estimates of defect densities are difficult to determine from resonance Raman spectroscopy, we expect the amounts of defects are small although this may not be reflected in device performance figures of merit.

In our current experiment, direct interrogation of the fullerene component was not possible because of the low Raman cross-sections at the excitation wavelengths used. Similar to X-ray induced degradation of P3HT films, some reports have demonstrated cross-linking type of reactions in fullerene crystallites. Unfortunately, selective resonant excitation of the P3HT component in our devices masks these effects. In order to rule out a similar trapping mechanism at the polymer-anode contact, we fabricated devices with MoO_3 as the hole transport layer which showed virtually no changes compared to those made with PEDOT–PSS (see Supporting Information).

Initial reports on the stability of various polymers to radiation performed in the late 1950's concluded that polymers with aromatic pendant (side) groups or incorporated into the polymer backbone were exceptionally resistant to radiation damage[234] while other unsubstituted paraffin polymers like polyethylene could retain trapped charges for months. Likewise, measurements of conductivity changes in polymers with irradiation showed that polymers with aromatic substituents or components in the main polymer backbone had temporary increases in conductivity which diminished quickly after radiation exposure ceased while paraffin polymers retained their higher conductivity for long periods of time[235].

I-V curves taken on our devices during irradiation show that devices become conductive after an accumulated dose of radiation in a short period of time, but that this effect is remediated naturally in a few minutes after radiation exposure has ceased (see Supporting Information).

7.3 Conclusions

Based upon the experimental work presented here, and reflected in the observations of others, we find that they polymer P3HT appears to be highly resistant to physical damage due to high-energy ionizing radiation in blend films. We observe no significant change in the ratios of single to double bonds which would indicate material degradation or in amorphous to aggregate ratios induced by extensive irradiation. There is no visible damage to devices either; i.e., discoloration, substrate hazing, etc., nor is there any significant increase in aggregation states of the polymer within the film.

In addition, we have found that a significant dose of radiation, 75 krad, in a short period of time can cause the device to short-circuit (see Supporting Information). This effect, which is likely due to massive ionization and trapping of free charges within the active layer, is naturally remediated within a brief time after irradiation has ceased.

We do find a significant difference in performance figures of merit to due irradiation, and we feel that this is most likely due to damage to the PCBM, or the acceptor/metal interface. We also find that the PCBM is most susceptible to this damage when it has been allowed to aggregate. Once aggregated, irradiation induced damage becomes irreversible. Interestingly, any damage incurred to an amorphous film by irradiation, even at high does, *is* reversible by annealing after irradiation. This is most likely due to the separation between individual polymer and acceptor molecules making it difficult for them to cross-link. Once these molecules are located in close physical proximity to one another via phase separation (aggregation), cross-linking effects become more probable.

It appears that a significant potential barrier develops within the electron transport material which accounts for the “s-curve” character of the I-V sweeps and the additional phase shift seen in IMVS spectra. This degradation appears to occur naturally within these devices as a function of their application (extended exposure to sunlight) but is accelerated with excessive radiation.

As far as their actual application for space based uses, polymer solar cells are essentially “radiation hard” and can withstand minor doses of radiation with very little impact on performance. As well, a temporary flux in radiation, (such as a solar flare) could cause the devices to short circuit for a brief period of time but they will recover their initial performance within a few minutes after radiation levels subside.

We intend to continue our investigations into potential space based applications for P3HT/PCBM organic solar cells by focusing on a more thorough investigation of electron acceptor material via selective Raman excitation of the PCBM, as well as a temperature dependent study of the “s-curve” behavior to determine if the charged interface is an injection or extraction barrier.

Chapter VIII

Conclusions

The structure of organic polymers in the solid state controls the electronic interactions which determine the processes by which excited states are deactivated. The understanding of this relationship dictates the necessary architecture for successful OPVs and other electronic devices. The studies in this dissertation highlight many important aspects of this relationship.

A single planar, well-conjugated polymer stem in a J-aggregate lacks electronic interactions with neighboring stems. This means that excitons born on such a stem will remain on that stem for the duration of their lifetime before decaying to the ground state. The excitons on such stems have a low binding energy and are easily split using an external electric field. Although the J-aggregate fibers presented here show large triplet quenching, this occurs because of the CT coupling at interchain CT states due to WFO. If it were possible to build J-aggregates without these defect states these nanofibers would contain hundreds of weakly bound excitons ripe for extraction.

H-aggregates contain thousands of such interchain CT states. While most of these states probably lead to charge production in solar cells, any state unquenched by charge transfer to the electron acceptor will likely decay into a triplet state. Triplet populations in thin films are most likely directly related to the number of unquenched interchain CT states in H-aggregates.

From this information it seems apparent that any mixture of states in a thin films results in poor performance. H-aggregate states coupled to J-aggregate states will result in triplet formation and vice versa. In order to begin to improve device performance the populations of one or the other type of state should be minimized in a thin film. What is most desired is an H-aggregate with complete CT quenching with no J-aggregate states or the exact opposite.

While this is true for P3HT, it is not necessarily true for other polymers. PTVs are strangely non-luminescent. While singlet fission has been proposed as the reason for this, we have shown that there are two polymorphs of the polymer present in thin films of this material. While we showed that the probable cause for low device efficiencies is the inability of the PCBM to gain access to the polymer backbone, it could be equally as true that the mixture of polymorphs leads to interchain CT states which cause triplet formation.

We know that this is true for the PBTTT polymer. The well-mixed co-crystals efficiently generate excitons but power loss for these materials occurs at the interface between co-crystalline and amorphous regions. Unquenched excitons in the amorphous phase can lead to triplet state formation, which can quench excitons at interfacial boundaries.

While radiation damages solar cells irreversibly, the amount of radiation necessary to do this is far beyond what a small satellite will ever encounter in a 3-5 year lifetime in low earth orbit, barring exceptional circumstances. In the meantime, these solar cells can bounce back from short intense bursts of radiation within a few minutes. While we have uncovered the fact that the electron acceptor is most likely to blame for this behavior, this is not at all surprising given the vast amount of information pointing to PCBM as the likely culprit. Even so, P3HT/PCBM solar cells make a promising target for future investigations for space based-applications.

Future work in this field will point towards controlling morphologies of materials to create ideal structures for creating, transporting, and splitting excitons. Equipped with the structure-function relationship understanding we now possess, this is no longer the daunting task it once was.

While the BHJ solar cell structure has served as an excellent test bed for investigating structure-function relationships, it is apparent that the overall efficiencies of OPVs are limited by this structure due to a lack of control over morphology at the molecular level. Future investigations into engineered 2 and 3 dimensional polymer structures where the electronic interaction between chromophores can be carefully controlled are essential. While this is difficult and time-consuming, it is certainly not beyond our current level of understanding and technology. The investment into understanding how to create 2 and 3 dimensional structures where electronic interactions are controlled and predictable will advance organic electronic to a new level of capability and commercial viability.

References

(1) Kippelen, B.; Bredas, J.-L. Organic Photovoltaics. *Energ Env. Sci* **2009**, *2*, 251–261.

(2) Forrest, S. R. The Path to Ubiquitous and Low-Cost Organic Electronic Appliances on Plastic. *Nature* **2004**, *428*, 911–918.

(3) Hachmann, J.; Olivares-Amaya, R.; Atahan-Evrenk, S.; Amador-Bedolla, C.; Sánchez-Carrera, R. S.; Gold-Parker, A.; Vogt, L.; Brockway, A. M.; Aspuru-Guzik, A. The Harvard Clean Energy Project: Large-Scale Computational Screening and Design of Organic Photovoltaics on the World Community Grid. *J. Phys. Chem. Lett.* **2011**, *2*, 2241–2251.

(4) Geffroy, B.; le Roy, P.; Prat, C. Organic Light-Emitting Diode (OLED) Technology: Materials, Devices and Display Technologies. *Polym. Int.* **2006**, *55*, 572–582.

(5) Huebler, A. C.; Doetz, F.; Kempa, H.; Katz, H. E.; Bartzsch, M.; Brandt, N.; Hennig, I.; Fuegmann, U.; Vaidyanathan, S.; Granstrom, J.; *et al.* Ring Oscillator Fabricated Completely by Means of Mass-Printing Technologies. *Org. Electron. physics, Mater. Appl.* **2007**, *8*, 480–486.

(6) Kaltenbrunner, M.; Sekitani, T.; Reeder, J.; Yokota, T.; Kuribara, K.; Tokuhara, T.; Drack, M.; Schwödiauer, R.; Graz, I.; Bauer-Gogonea, S.; *et al.* An Ultra-Lightweight Design for Imperceptible Plastic Electronics. *Nature* **2013**, *499*, 458–463.

(7) Martin A. Green, Keith Emery, Yoshihiro Hishikawa, W. W. and E. D. D. Solar

Cell Efficiency Tables (Version 47). *Prog. Photovolt Res. Appl.* **2007**, *15*, 659–676.

(8) International Energy Agency. Key World Energy Statistics 2015. **2015**, 81.

(9) Duncan, R. C. World Energy Production , Population Growth , and the Road to the Olduvai Gorge. **1988**, *22*, 503–522.

(10) Smalley, R. E. Future Global Energy Prosperity: The Terawatt Challenge. *MRS Bull.* **2005**, *30*, 412–417.

(11) Graetzel, M.; Janssen, R. a J.; Mitzi, D. B.; Sargent, E. H. Materials Interface Engineering for Solution-Processed Photovoltaics. *Nature* **2012**, *488*, 304–312.

(12) Li, G.; Zhu, R.; Yang, Y. Polymer Solar Cells. *Nat. Photonics* **2012**, *6*, 153–161.

(13) Scharber, M. C.; Sariciftci, N. S. Efficiency of Bulk-Heterojunction Organic Solar Cells. *Prog. Polym. Sci.* **2013**, *in press*, .

(14) Po, R.; Maggini, M.; Camaioni, N. Polymer Solar Cells: Recent Approaches and Achievements. *J. Phys. Chem. C* **2010**, *114*, 695–706.

(15) Zhang, S.; Ye, L.; Hou, J. Breaking the 10% Efficiency Barrier in Organic Photovoltaics: Morphology and Device Optimization of Well-Known PBDTTT Polymers. *Adv. Energy Mater.* **2016**.

(16) Burkhard, G. F.; Hoke, E. T.; McGehee, M. D. Accounting for Interference, Scattering, and Electrode Absorption to Make Accurate Internal Quantum Efficiency Measurements in Organic and Other Thin Solar Cells. *Adv. Mater.* **2010**, *22*, 3293–3297.

(17) Ma, W.; Yang, C.; Gong, X.; Lee, K.; Heeger, A. J. Thermally Stable, Efficient Polymer Solar Cells with Nanoscale Control of the Interpenetrating Network Morphology. *Adv. Funct. Mater.* **2005**, *15*, 1617–1622.

(18) Li, G.; Shrotriya, V.; Huang, J.; Yao, Y.; Moriarty, T.; Emery, K.; Yang, Y. High-Efficiency Solution Processable Polymer Photovoltaic Cells by Self-Organization of Polymer Blends. *Nat. Mater.* **2005**, *4*, 864–868.

(19) Camaioni, N.; Garlaschelli, L.; Geri, A.; Maggini, M.; Possamai, G.; Ridolfi, G. Solar Cells Based on poly(3-Alkyl)thiophenes and [60]fullerene: A Comparative Study. *J. Mater. Chem.* **2002**, *12*, 2065–2070.

(20) Dyakonov, V.; Rösler, G.; Schwoerer, M.; Frankevich, E. Evidence for Triplet Interchain Polaron Pairs and Their Transformations in Polyphenylenevinylene. *Phys. Rev. B* **1997**, *56*, 3852–3862.

(21) Yu, G.; Gao, J.; Hummelen, J. C.; Wudl, F.; Heeger, A. J. Device Structure Consisted Polymer Photovoltaic Cells : Enhanced Efficiencies via a (Ca The on a G | | G. *Science (80-.).* **1995**, *270*, 1789–1791.

(22) Halls, J. J. M.; Walsh, C. A.; Greenham, N. C.; Marseglia, E. A.; Friend, R. H.; Moratti, S. C.; Holmes, A. B. Efficient Photodiodes From Interpenetrating Polymer Networks. *Nature*, 1995, *376*, 498–500.

(23) Steim, R.; Kogler, F. R.; Brabec, C. J. Interface Materials for Organic Solar Cells. *J. Mater. Chem.* **2010**, *20*, 2499.

(24) Spanggaard, H.; Krebs, F. C. A Brief History of the Development of Organic and Polymeric Photovoltaics. *Sol. Energy Mater. Sol. Cells* **2004**, *83*, 125–146.

(25) Reese, M. O.; White, M. S.; Rumbles, G.; Ginley, D. S.; Shaheen, S. E. Optimal Negative Electrodes for poly(3-Hexylthiophene): [6,6]-Phenyl C61-Butyric Acid Methyl Ester Bulk Heterojunction Photovoltaic Devices. *Appl. Phys. Lett.* **2008**, *92*, 9–12.

(26) Eo, Y. S.; Rhee, H. W.; Chin, B. D.; Yu, J.-W. Influence of Metal Cathode for Organic Photovoltaic Device Performance. *Synth. Met.* **2009**, *159*, 1910–1913.

(27) Mihailetchi, V. D.; Blom, P. W. M.; Hummelen, J. C.; Rispens, M. T. Cathode Dependence of the Open-Circuit Voltage of Polymer:fullerene Bulk Heterojunction Solar Cells. *J. Appl. Phys.* **2003**, *94*, 6849–6854.

(28) Almenningen, A.; Bastiansen, O.; Hansen, L. Electron Diffraction Studies of Hexaphenylbenzene Vapour. *Acta Chem. Scand.* **1957**, *9*, 1306–1310.

(29) Gierschner, J.; Cornil, J.; Egelhaaf, H. J. Optical Bandgaps of π-Conjugated Organic Materials at the Polymer Limit: Experiment and Theory. *Adv. Mater.* **2007**, *19*, 173–191.

(30) Forster, T. Energiewanderung Und Fluoreszenz. *Naturwissenschaften* **1946**, *33*, 166–175.

(31) Alvarado, S. F.; Seidler, P. F.; Lidzey, D. G.; Bradley, D. D. C. Direct Determination of the Exciton Binding Energy of Conjugated Polymers Using a Scanning Tunneling Microscope. *Phys. Rev. Lett.* **1998**, *81*, 1082–1085.

(32) Deibel, C.; MacK, D.; Gorenflot, J.; Sch??ll, A.; Krause, S.; Reinert, F.; Rauh, D.; Dyakonov, V. Energetics of Excited States in the Conjugated Polymer poly(3-Hexylthiophene). *Phys. Rev. B - Condens. Matter Mater. Phys.* **2010**, *81*, 1–5.

(33) Bredas, J. L.; Cornil, J.; Heeger, A. J.; Briidas, B. J. The Exciton Binding Energy in Luminescent Conjugated Polymers. *Adv. Mater.* **1996**, *8*, 447 – &.

(34) B.R. Weinberger, M. Akhtar, S. C. G. Polyacetylene Photovoltaic Devices. *Synth. Met.* **1982**, *4*, 187–197.

(35) Nelson, J. Organic Photovoltaic Films. *Curr. Opin. Solid State Mater. Sci.* **2002**, *6*, 87–95.

(36) McGehee, M. D.; Topinka, M. a. Solar Cells: Pictures from the Blended Zone. *Nat. Mater.* **2006**, *5*, 675–676.

(37) Jelley, E. E. Spectral Absorption and Fluorescence of Dyes in the Molecular State. *Nature* **1936**, 1009–1010.

(38) Jelley, E. Molecular, Nematic and Crystal States of I: I-Diethyl--Cyanine Chloride. *Nature* **1937**, *139*, 631–631.

(39) West, W.; Carroll, B. H. Energy Transfer in the Photo-Sensitization of Silver Halide Photographic Emulsions: Optical Sensitization, Supersensitization, and Antisensitization. *J. Chem. Phys.* **1951**, *19*, 417.

(40) Franck, J.; Teller, E. Migration and Photochemical Action of Excitation Energy in Crystals. *J. Chem. Phys.* **1938**, *6*, 861.

(41) Kasha, M. Energy Transfer Mechanisms and the Molecular Exciton Model for Molecular Aggregates Author (S): Michael Kasha Stable URL : http://www.jstor.org/stable/3571331 REFERENCES Linked References Are Available on JSTOR for This Article : You May Need to Log in. **2016**, *20*, 55–70.

(42) Barford, W.; Manas, E. S.; Spano, F. C.; Cornil, J.; dos Santos, D. A.; Crispin, X.;

Silbey, R.; Brédas, J. L.; Gierschner, J.; Huang, Y.-S.; *et al.* Absorption and Spontaneous Emission in Aggregates of Conjugated Polymers. *J. Chem. Phys.* **1998**, *126*, 7439.

(43) Siddiqui, S.; Spano, F. C. H- and J-Aggregates of Conjugated Polymers and Oligomers. *Chem. Phys. Lett.* **1999**, *308*, 99–105.

(44) Soos, Z. G.; Hayden, G. W.; McWilliams, P. C. M.; Etemad, S. Excitation Shifts of Parallel Conjugated Polymers due to π-Electron Dispersion Forces. *J. Chem. Phys.* **1990**, *93*, 7439.

(45) Cornil, J. Influence of Interchain Interactions in the Absorption and Luminescence of Conjugated Oligomers and Polymers: A Quantum-Chemical Characterization. *J. Am. Chem. Soc.* **1998**, *120*, 1289–1299.

(46) Manas, E. S.; Spano, F. C. Absorption and Spontaneous Emission in Aggregates of Conjugated Polymers. *J. Chem. Phys.* **1998**, *109*, 8087–8101.

(47) Yamagata, H.; Pochas, C. M.; Spano, F. C. Designing J- and H‐ Aggregates through WavefunctionOverlap Engineering : Applications to Poly (3-Hexylthiophene). **2012**.

(48) Tang, C. W. Two-Layer Organic Photovoltaic Cell. *Appl. Phys. Lett.* **1986**, *48*, 183–185.

(49) Sirringhaus, H.; Kawase, T.; Friend, R. H.; Shimoda, T.; Inbasekaran, M.; Wu, W.; Woo, E. P. High-Resolution Inkjet Printing of All-Polymer Transistor Circuits. *Science (80-.).* **2000**, *290*, 2123–2126.

(50) Niles, E. T.; Roehling, J. D.; Yamagata, H.; Wise, A. J.; Spano, F. C.; Moule, A.

J.; Grey, J. K. J-Aggregate Behavior in Poly-3-Hexylthiophene Nanofibers. *J. Phys. Chem. Lett.* **2012**, 259–263.

(51) Baghgar, M.; Labastide, J. A.; Bokel, F.; Hayward, R. C.; Barnes, M. D. E Ff Ect of Polymer Chain Folding on the Transition from H- to. **2014**.

(52) Gao, J.; Kamps, A.; Park, S.; Grey, J. K. Encapsulation of Poly(3-Hexylthiophene) J‑ Aggregate Nanofibers with an Amphiphilic Block Copolymer. *Langmuir* **2012**, 16401–16407.

(53) Yuan, Y.; Shu, J.; Liu, P.; Zhang, Y.; Duan, Y.; Zhang, J. Study on π − π Interaction in H- and J ‑ Aggregates of Poly (3- Hexylthiophene) Nanowires by Multiple Techniques.

(54) Roehling, J. D.; Arslan, I.; Moulé, A. J. Controlling Microstructure in poly(3-Hexylthiophene) Nanofibers. *J. Mater. Chem.* **2012**, *22*, 2498.

(55) Brinkmann, M.; Rannou, P. Molecular Weight Dependence of Chain Packing and Semicrystalline Structure in Oriented Films of Regioregular poly(3-Hexylthiophene)revealed by High-Resolution Transmission Electron Microscopy. *Macromolecules* **2009**, *42*, 1125–1130.

(56) With, G. De. Three-Dimensional Structure of P3HT Assemblies in Organic Solvents Revealed by Cryo-TEM. **2014**.

(57) Lee, Y.; Oh, J. Y.; Son, S. Y.; Park, T.; Jeong, U. Effects of Regioregularity and Molecular Weight on the Growth of Polythiophene Nanofibrils and Mixes of Short and Long Nanofibrils To Enhance the Hole Transport. *ACS Appl. Mater. Interfaces* **2015**, acsami.5b08432.

(58) Kondakov, D. Y. Characterization of Triplet-Triplet Annihilation in Organic Light-Emitting Diodes Based on Anthracene Derivatives. *J. Appl. Phys.* **2007**, *102*.

(59) Endo, A.; Sato, K.; Yoshimura, K.; Kai, T.; Kawada, A.; Miyazaki, H.; Adachi, C. Efficient up-Conversion of Triplet Excitons into a Singlet State and Its Application for Organic Light Emitting Diodes. *Appl. Phys. Lett.* **2011**, *98*.

(60) Baldo, M.; Thompson, M.; Forrest, S. High-Efficiency Fluorescent Organic Light-Emitting Devices Using a Phosphorescent Sensitizer. *Nature* **2000**, *403*, 750–753.

(61) Burroughes, J. H.; Bradley, D. D. C.; Brown, a. R.; Marks, R. N.; Mackay, K.; Friend, R. H.; Burns, P. L.; Holmes, a. B. Light-Emitting Diodes Based on Conjugated Polymers. *Nature* **1990**, *347*, 539–541.

(62) AlSalhi, M. S.; Alam, J.; Dass, L. A.; Raja, M. Recent Advances in Conjugated Polymers for Light Emitting Devices. *Int. J. Mol. Sci.* **2011**, *12*, 2036–2054.

(63) Tang, C. W.; Vanslyke, S. A. Organic Electroluminescent Diodes. *Appl. Phys. Lett.* **1987**, *51*, 913–915.

(64) Sheats, J. R.; Antoniadis, H.; Hueschen, M.; Leonard, W.; Miller, J.; Moon, R.; Roitman, D.; Stocking, A. Organic Electroluminescent Devices. *Science (80-.).* **1996**, *273*, 884–888.

(65) Koster, L. J. A.; Mihailetchi, V. D.; Blom, P. W. M. Bimolecular Recombination in Polymer/fullerene Bulk Heterojunction Solar Cells. *Appl. Phys. Lett.* **2006**, *88*, 1–3.

(66) Rao, A.; Chow, P. C. Y.; Gélinas, S.; Schlenker, C. W.; Li, C.-Z.; Yip, H.-L.; Jen, A. K.-Y.; Ginger, D. S.; Friend, R. H. The Role of Spin in the Kinetic Control of

Recombination in Organic Photovoltaics. *Nature* **2013**, *500*, 435–439.

(67) Dyakonov, V.; Frankevich, E. On the Role Played by Polaron Pairs in Photophysical Processes in Semiconducting Polymers. *Chem. Phys.* **1998**, *227*, 203–217.

(68) Wohlgenannt, M.; Tandon, K.; Mazumdar, S.; Ramasesha, S.; Vardeny, Z. V. Formation Cross-Sections of Singlet and Triplet Excitons in Pi-Conjugated Polymers. *Nature* **2001**, *409*, 494–497.

(69) Yeldman, D.; Chopin, S. M. A.; Meskers, S. C. J.; Janssen, R. A. J. Enhanced Intersystem Crossing via a High Energy Charge Transfer State in a Perylenediimide-Perylenemonoimide Dyad. *J. Phys. Chem. A* **2008**, *112*, 8617–8632.

(70) Marks, R. N.; Halls, J. J. M.; Bradley, D. D. C.; Friend, R. H.; Holmes, a B. The Photovoltaic Response in Poly(p-Phenylene Vinylene) Thin-Film Devices. *J. Phys. Condens. Matter* **1994**, *6*, 1379.

(71) Sun, S.; Fan, Z.; Wang, Y.; Haliburton, J. Organic Solar Cell Optimizations. *J. Mater. Sci.* **2005**, *40*, 1429–1443.

(72) Jiang, X. M.; Osterbacka, R.; Korovyanko, O.; An, C. P.; Horovitz, B.; Janssen, R. a J.; Vardeny, Z. V. Spectroscopic Studies of Photoexcitations in Regioregular and Regiorandom Polythiophene Films. *Adv. Funct. Mater.* **2002**, *12*, 587.

(73) Smekal, A. Zuschriften Und Vorlaufige Mitteilungen. *Naturwissenschaften* **1923**, *11*, 873–875.

(74) RAMAN, C. V.; KRISHNAN, K. S. A New Type of Secondary Radiation. *Nature*

1928, *121*, 501–502.

(75) Lee, S.-Y.; Heller, E. J. Time-Dependent Theory of Raman Scattering. *J. Chem. Phys.* **1979**, *71*, 4777.

(76) Heller, E. J. The Semiclassical Way to Molecular Spectroscopy. *Acc. Chem. Res.* **1981**, *14*, 368–375.

(77) Schwartz, B. J. C <scp>ONJUGATED</scp> P <scp>OLYMERS AS</scp> M <scp>OLECULAR</scp> M <scp>ATERIALS</scp> : How Chain Conformation and Film Morphology Influence Energy Transfer and Interchain Interactions. *Annu. Rev. Phys. Chem.* **2003**, *54*, 141–172.

(78) Brinkmann, M. Structure and Morphology Control in Thin Films of Regioregular poly(3-Hexylthiophene). *J. Polym. Sci. Part B Polym. Phys.* **2011**, *49*, 1218–1233.

(79) Sirringhaus, H.; Brown, P. J.; Friend, R. H.; Nielsen, M. M.; Bechgaard, K.; Langeveld-Voss, B. M. W.; Spiering, a. J. H.; Janssen, R. a. J.; Meijer, E. W.; Herwig, P.; *et al.* Two-Dimensional Charge Transport in Self-Organized, High-Mobility Conjugated Polymers. *Nature* **1999**, *401*, 685–688.

(80) Ingana, O.; Lundstro, I.; Gadegaard, N. Österbacka - Two-Dimensional Electronic Excitaions in Self-Assembled Conjugated Polymer Nanocrystals. **2000**, *287*, 1–5.

(81) Spano, F. C. The Spectral Signatures of Frenkel Polarons in H- and J-Aggregates. *Acc. Chem. Res.* **2010**, *43*, 429–439.

(82) Yamagata, H.; Spano, F. C. Interplay between Intrachain and Interchain Interactions in Semiconducting Polymer Assemblies: The HJ-Aggregate Model. *J. Chem. Phys.* **2012**, *136*, 0–14.

(83) Clark, J.; Silva, C.; Friend, R. H.; Spano, F. C. Role of Intermolecular Coupling in the Photophysics of Disordered Organic Semiconductors: Aggregate Emission in Regioregular Polythiophene. *Phys. Rev. Lett.* **2007**, *98*, 206406.

(84) Paquin, F.; Latini, G.; Sakowicz, M.; Karsenti, P.-L.; Wang, L.; Beljonne, D.; Stingelin, N.; Silva, C. Charge Separation in Semicrystalline Polymeric Semiconductors by Photoexcitation: Is the Mechanism Intrinsic or Extrinsic? *Phys. Rev. Lett.* **2011**, *106*, 197401.

(85) Reid, O. G.; Pensack, R. D.; Song, Y.; Scholes, G. D.; Rumbles, G. Charge Photogeneration in Neat Conjugated Polymers. *Chem. Mater.* **2014**, *26*, 561–575.

(86) Paquin, F.; Yamagata, H.; Hestand, N. J.; Sakowicz, M.; Bérubé, N.; Côté, M.; Reynolds, L. X.; Haque, S. a.; Stingelin, N.; Spano, F. C.; *et al.* Two-Dimensional Spatial Coherence of Excitons in Semicrystalline Polymeric Semiconductors: Effect of Molecular Weight. *Phys. Rev. B - Condens. Matter Mater. Phys.* **2013**, *88*, 1–38.

(87) Guo, J.; Ohkita, H.; Benten, H.; Ito, S. Near-IR Femtosecond Transient Absorption Spectroscopy of Ultrafast Polaron and Triplet Exciton Formation in Polythiophene Films with Different Regioregularities. *J. Am. Chem. Soc.* **2009**, *131*, 16869–16880.

(88) Tapping, P. C.; Kee, T. W. Optical Pumping of Poly (3-Hexylthiophene) Singlet Excitons Induces Charge Carrier Generation. *J. Phys. Chem. Lett.* **2014**, *5*, 1040–1047.

(89) Hu, D.; Yu, J.; Wong, K.; Bagchi, B.; Rossky, P.; Barbara, P. Collapse of Stiff Conjugated Polymers with Chemical Defects into Ordered, Cylindrical

Conformations. *Nature* **2000**, *405*, 1030–1033.

(90) Yu, J.; Hu, D.; Barbara, P. F. Unmasking Electronic Energy Transfer of Conjugated Polymers by Suppression of O2 Quenching. *Science (80-.).* **2000**, *289*, 1327.

(91) Grey, J. K.; Kim, D. Y.; Norris, B. C.; Miller, W. L.; Barbara, P. F. Size-Dependent Spectroscopic Properties of Conjugated Polymer Nanoparticles. *J. Phys. Chem. B* **2006**, *110*, 25568–25572.

(92) Huser, T.; Yan, M.; Rothberg, L. J. Single Chain Spectroscopy of Conformational Dependence of Conjugated Polymer Photophysics. *Proc. Nat. Acad. Sci.* **2000**, *97*, 11187–11191.

(93) Steiner, F.; Vogelsang, J.; Lupton, J. M. Singlet-Triplet Annihilation Limits Exciton Yield in poly(3-Hexylthiophene). *Phys. Rev. Lett.* **2014**, *112*, 1–5.

(94) Kim, D. Y.; Grey, J. K.; Barbara, P. F. A Detailed Single Molecule Spectroscopy Study of the Vibronic States and Energy Transfer Pathways of the Conjugated Polymer MEH-PPV. *Synth. Met.* **2006**, *156*, 336–345.

(95) Bolinger, J. C.; Traub, M. C.; Brazard, J.; Adachi, T.; Barbara, P. F.; Vanden Bout, D. A. Conformation and Energy Transfer in Single Conjugated Polymers. *Acc. Chem. Res.* **2012**, *45*, 1992–2001.

(96) Gesquiere, A. J.; Park, S. J.; Barbara, P. F. F-V/SMS: A New Technique for Studying the Structure and Dynamics of Single Molecules and Nanoparticles. *J. Phys. Chem. B* **2004**, *108*, 10301–10308.

(97) Barbara, P. F.; Gesquiere, A. J.; Park, S.-J.; Lee, Y. J. Single-Molecule

Spectroscopy of Conjugated Polymers. *Acc. Chem. Res.* **2005**, *38*, 602–610.

(98) Bolinger, J. C.; Traub, M. C.; Adachi, T.; Barbara, P. F. Ultralong-Range Polaron-Induced Quenching of Excitons in Isolated Conjugated Polymers. *Science (80-.).* **2011**, *331*, 565–567.

(99) Vosch, T.; Hofkens, J.; Cotlet, M.; Köhn, F.; Fujiwara, H.; Gronheid, R.; Van Der Biest, K.; Weil, T.; Herrmann, A.; Müllen, K.; *et al.* Influence of Structural and Rotational Isomerism on the Triplet Blinking of Individual Dendrimer Molecules. *Angew. Chemie - Int. Ed.* **2001**, *40*, 4643–4648.

(100) Gesquiere, A. J.; Lee, Y. J.; Barbara, P. F.; Yu, J. Single Molecule Modulation Spectroscopy of Conjugated Polymers. *J. Phys. Chem. B* **2005**, *109*, 12366–12371.

(101) Gesquiere, A. J.; Park, S. J.; Barbara, P. F. Hole-Induced Quenching of Triplet and Singlet Excitons in Conjugated Polymers. *J. Am. Chem. Soc.* **2005**, *127*, 9556–9560.

(102) Wohlgenannt, M.; Vardeny, Z. V; Frolov, S. V; Kloc, C.; Batlogg, B. Long-Lived Photoexcitations in Alpha-Hexathiophene Single Crystals. *Synth. Met.* **2001**, *116*, 181–184.

(103) Barford, W. Exciton Transfer Integrals between Polymer Chains. *J. Chem. Phys.* **2007**, *126*.

(104) Baghgar, M.; Labastide, J.; Bokel, F.; Dujovne, I.; McKenna, A.; Barnes, A. M.; Pentzer, E.; Emrick, T.; Hayward, R.; Barnes, M. D. Probing Inter- and Intrachain Exciton Coupling in Isolated poly(3-Hexylthiophene) Nanofibers: Effect of Solvation and Regioregularity. *J. Phys. Chem. Lett.* **2012**, *3*, 1674–1679.

(105) Martin, T.; Wise, A.; Busby, E.; Gao, J.; Roehling, J. D.; Ford, M. J.; Larsen, D. S.; Moulé, A. J.; Grey, J. K. Packing Dependent Electronic Coupling in Single Poly (3-Hexylthiophene) H-and J-Aggregate Nanofibers. *J. Phys. Chem. B* **2012**, *117*, 4478–4487.

(106) Yu, J.; Lammi, R.; Gesquiere, A. J.; Barbara, P. F. Singlet-Triplet and Triplet-Triplet Interactions in Conjugated Polymer Single Molecules. *J. Phys. Chem. B* **2005**, *109*, 10025–10034.

(107) Köhler, A.; Bässler, H. Triplet States in Organic Semiconductors. *Mater. Sci. Eng. R Reports* **2009**, *66*, 71–109.

(108) Clarke, T.; Durrant, J. Charge Photogeneration in Organic Solar Cells. *Chem. Rev.* **2010**, 6736–6767.

(109) Abdou, M. S. A.; Orfino, F. P.; Son, Y.; Holdcroft, S. Interaction of Oxygen with Conjugated Polymers: Charge Transfer Complex Formation with poly(3-Alkylthiophenes). *J. Am. Chem. Soc.* **1997**, *119*, 4518–4524.

(110) Palacios, R. E.; Barbara, P. F. Single Molecule Spectroscopy of Poly 3-Octyl-Thiophene (P3OT). *J. Fluoresc.* **2007**, *17*, 749–757.

(111) Schindler, F.; Lupton, J. M.; Feldmann, J.; Scherf, U. Controlled Fluorescence Bursts from Conjugated Polymers Induced by Triplet Quenching. *Adv. Mater.* **2004**, *16*, 653.

(112) Sperlich, A.; Kraus, H.; Deibel, C.; Blok, H.; Schmidt, J.; Dyakonov, V. With Oxygen Studied by Spin-Sensitive Methods Reversible and Irreversible Interactions of P3HT with Oxygen Studied by Spin-Sensitive Methods. **2011**,

13513–13518.

(113) Cook, S.; Furube, A.; Katoh, R. Analysis of the Excited States of Regioregular Polythiophene P3HT. *Energy Environ. Sci.* **2008**, *1*, 294.

(114) Hayer, A.; Khan, A. L. T.; Friend, R. H.; Köhler, A. Morphology Dependence of the Triplet Excited State Formation and Absorption in Polyfluorene. *Phys. Rev. B - Condens. Matter Mater. Phys.* **2005**, *71*, 1–4.

(115) Smith, M. B.; Michl, J. Singlet Fission. *Chem. Rev.* **2010**, *110*, 6891–6936.

(116) Monkman, A.; Burrows, H. D. Backbone Planarity Effects on Triplet Energies and Electron-Electron Correlation in Luminescent Conjugated Polymers. *Synth. Met.* **2004**, *141*, 81–86.

(117) Beljonne, D.; Shuai, Z.; Pourtois, G.; Bredas, J. L. Spin−Orbit Coupling and Intersystem Crossing in Conjugated Polymers: A Configuration Interaction Description. *J. Phys. Chem. A* **2001**, *105*, 3899–3907.

(118) Turro, N. J. *Modern Molecular Photochemistry*; University Science Books: Mill Valley, CA, 1978.

(119) Pensack, R. D.; Song, Y.; McCormick, T. M.; Jahnke, A. A.; Hollinger, J.; Seferos, D. S.; Scholes, G. D. Evidence for the Rapid Conversion of Primary Photoexcitations to Triplet States in Seleno- and Telluro- Analogues of poly(3-Hexylthiophene). *J. Phys. Chem. B* **2014**, *118*, 2589–2597.

(120) Ruseckas, A.; Theander, M.; Andersson, M. R.; Svensson, M.; Prato, M.; Inganäs, O.; Sundström, V. Ultrafast Photogeneration of Inter-Chain Charge Pairs in Polythiophene Films. *Chem. Phys. Lett.* **2000**, *322*, 136–142.

(121) Zenz, C.; Cerullo, G.; Lanzani, G.; Graupner, W.; Meghdadi, F.; Leising, G.; De Silvestri, S. Ultrafast Photogeneration Mechanisms of Triplet States in Para-Hexaphenyl. *Phys. Rev. B* **1999**, *59*, 14336–14341.

(122) Wohlgenannt, M.; Jiang, X. M.; Yang, C.; Korovyanko, O. J.; Vardeny, Z. V. Spin-Dependent Polaron Pair Recombination in ??-Conjugated Polymers: Enhanced Singlet Exciton Densities. *Synth. Met.* **2003**, *139*, 921–924.

(123) Wohlgenannt, M.; Jiang, X. M.; Vardeny, Z. V.; Janssen, R. A. J. Conjugation-Length Dependence of Spin-Dependent Exciton Formation Rates in <math Display="inline"> <mi>Π</mi> </math> -Conjugated Oligomers and Polymers. *Phys. Rev. Lett.* **2002**, *88*, 197401.

(124) Monkman, A. P.; Burrows, H. D.; Hartwell, L. J.; Horsburgh, L. E.; Hamblett, I.; Navaratnam, S. Triplet Energies of P-Conjugated Polymers. *Phys. Rev. Lett.* **2001**, *86*, 1358–1361.

(125) Köhler, A.; Bässler, H. Triplet States in Organic Semiconductors. *Mater. Sci. Eng. R Reports* **2009**, *66*, 71–109.

(126) Köhler, A.; Wilson, J. Phosphorescence and Spin-Dependent Exciton Formation in Conjugated Polymers. *Org. Electron. physics, Mater. Appl.* **2003**, *4*, 179–189.

(127) Liedtke, M.; Sperlich, A.; Kraus, H.; Baumann, A.; Deibel, C.; Wirix, M. J. M.; Loos, J.; Cardona, C. M.; Dyakonov, V. Triplet Exciton Generation in Bulk-Heterojunction Solar Cells Based on Endohedral Fullerenes. *J. Am. Chem. Soc.* **2011**, *133*, 9088–9094.

(128) Smith, M.; Michl, J. Singlet Fission. *Chem. Rev.* **2010**, *110*, 6891–6936.

(129) Tamai, Y.; Ohkita, H.; Benten, H.; Ito, S. Singlet Fission in Poly (9,9′-Di-N-Octylfluorene) Films. *J. Phys. Chem. C* **2013**, *117*, 10277–10284.

(130) Kanemoto, K.; Yasui, M.; Higuchi, T.; Kosumi, D.; Akai, I.; Karasawa, T.; Hashimoto, H. Spectroscopic Investigation of Excitons, Photocarriers, and Bias-Induced Carriers in Regioregular poly(3-Alkylthiophene). *Phys. Rev. B - Condens. Matter Mater. Phys.* **2011**, *83*, 1–7.

(131) Österbacka, R.; Wohlgenannt, M.; Chinn, D.; Vardeny, Z. Optical Studies of Triplet Excitations in Poly(p-Phenylene Vinylene). *Phys. Rev. B* **1999**, *60*, R11253–R11256.

(132) Bange, S.; Scherf, U.; Lupton, J. M. Absence of Singlet Fission and Carrier Multiplication in a Model Conjugated Polymer: Tracking the Triplet Population through Phosphorescence. *J. Am. Chem. Soc.* **2012**, *134*, 1946–1949.

(133) Gao, J.; Stein, B. W.; Thomas, A. K.; Garcia, J. A.; Yang, J.; Kirk, M. L.; Grey, J. K. Enhanced Charge Transfer Doping Efficiency in J-Aggregate Poly(3-Hexylthiophene) Nanofibers. *J. Phys. Chem. C* **2015**, *119*, 16396–16402.

(134) Banerji, N. Sub-Picosecond Delocalization in the Excited State of Conjugated Homopolymers and Donor–acceptor Copolymers. *J. Mater. Chem. C* **2013**, *1*, 3052.

(135) Spano, F. C.; Yamagata, H. Vibronic Coupling in J-Aggregates and beyond: A Direct Means of Determining the Exciton Coherence Length from the Photoluminescence Spectrum. *J. Phys. Chem. B* **2011**, *115*, 5133–5143.

(136) Tempelaar, R.; Spano, F. C.; Knoester, J.; Jansen, T. L. C. Mapping the Evolution

of Spatial Exciton Coherence through Time-Resolved Fluorescence. *J. Phys. Chem. Lett.* **2014**, *5*, 1505–1510.

(137) Barford, W. Excitons in Conjugated Polymers: A Tale of Two Particles. *J. Phys. Chem. A* **2013**, *117*, 2665–2671.

(138) Barford, W.; Lidzey, D. G.; Makhov, D. V.; Meijer, A. J. H. Exciton Localization in Disordered poly(3-Hexylthiophene). *J. Chem. Phys.* **2010**, *133*.

(139) Spano, F. C.; Silva, C. H- and J-Aggregate Behavior in Polymeric Semiconductors. *Annu. Rev. Phys. Chem.* **2014**, *65*, 477–500.

(140) Yang, S.-C.; Graupner, W.; Guha, S.; Puschnig, P.; Martin, C.; Chandrasekhar, H.; Chandrasekhar, M.; Leising, G.; Ambrosch-Draxl, C.; Scherf, U. Geometry-Dependent Electronic Properties of Highly Fluorescent Conjugated Molecules. *Phys. Rev. Lett.* **2000**, *85*, 2388–2391.

(141) Chang, W.; Congreve, D. N.; Hontz, E.; Bahlke, M. E.; McMahon, D. P.; Reineke, S.; Wu, T. C.; Bulović, V.; Van Voorhis, T.; Baldo, M. a. Spin-Dependent Charge Transfer State Design Rules in Organic Photovoltaics. *Nat. Commun.* **2015**, *6*, 6415.

(142) Deibe, C.; Strobe, T.; Dyakonov, V. Role of the Charge Transfer State in Organic Donor-Acceptor Solar Cells. *Adv. Mater.* **2010**, *22*, 4097–4111.

(143) Mazzio, K. A.; Rice, A. H.; Durban, M. M.; Luscombe, C. K. Effect of Regioregularity on Charge Transport and Structural and Excitonic Coherence in Poly(3-Hexylthiophene) Nanowires. *J. Phys. Chem. C* **2015**, *119*, 14911–14918.

(144) Alan K. Thomas, Jose´ A. Garcia, Jordan Ulibarri-Sanchez, Jian Gao, J. K. G.

High Intrachain Order Promotes Triplet Formation from Recombination of Long-Lived Polarons in Poly(3-Hexylthiophene) J-Aggregate Nanofibers. *ACS Nano* **2014**, *8*, 10559–10568.

(145) Heiber, M. C.; Dhinojwala, A. Estimating the Magnitude of Exciton Delocalization in Regioregular P3HT. *J. Phys. Chem. C* **2013**, *117*, 21627–21634.

(146) Reid, O. G.; Rumbles, G. Quantitative Transient Absorption Measurements of Polaron Yield. *J. Phys. Chem. Lett.* **2013**, *4*, 2348–2355.

(147) Magnanelli, T. J.; Bragg, A. E. Time-Resolved Raman Spectroscopy of Polaron Pair Formation in poly(3-Hexylthiophene) Aggregates. *J. Phys. Chem. Lett.* **2015**, *6*, 438–445.

(148) Dimitrov, S. D.; Wheeler, S.; Niedzialek, D.; Schroeder, B. C.; Utzat, H.; Frost, J. M.; Yao, J.; Gillett, A.; Tuladhar, P. S.; McCulloch, I.; *et al.* Polaron Pair Mediated Triplet Generation in Polymer/fullerene Blends. *Nat. Commun.* **2015**, *6*, 6501.

(149) Hu, Z.; Willard, A. P.; Ono, R. J.; Bielawski, C. W.; Rossky, P. J.; Vanden Bout, D. A. An Insight into Non-Emissive Excited States in Conjugated Polymers. *Nat. Commun.* **2015**, *6*, 8246.

(150) Beljonne, D.; Yamagata, H.; Br??das, J. L.; Spano, F. C.; Olivier, Y. Charge-Transfer Excitations Steer the Davydov Splitting and Mediate Singlet Exciton Fission in Pentacene. *Phys. Rev. Lett.* **2013**, *110*, 1–5.

(151) Lagoudakis, P. G. Pavlos Savvidis. *Nano Lett.* **2004**, *4*, 2004–2006.

(152) Wachsmann-hogiu, S.; Peteanu, L. A.; Liu, L. A.; Yaron, D. J.; Wildeman, J. The

Effects of Structural and Microenvironmental Disorder on the Electronic Properties of Oligomers. *J. Phys. Chem. B* **2003**, *107*, 5133–5143.

(153) Schindler, F.; Lupton, J. M.; Müller, J.; Feldmann, J.; Scherf, U. How Single Conjugated Polymer Molecules Respond to Electric Fields. *Nat. Mater.* **2006**, *5*, 141–146.

(154) Liess, M.; Jeglinski, S.; Vardeny, Z.; Ozaki, M.; Yoshino, K.; Ding, Y.; Barton, T. Electroabsorption Spectroscopy of Luminescent and Nonluminescent π-Conjugated Polymers. *Phys. Rev. B* **1997**, *56*, 15712–15724.

(155) Parkinson, P.; Müller, C.; Stingelin, N.; Johnston, M. B.; Herz, L. M. The Role of Ultrafast Torsional Relaxation in the Emission from Polythiophene Aggregates. *Conf. Optoelectron. Microelectron. Mater. Devices, Proceedings, COMMAD* **2010**, 117–118.

(156) Theander, M.; Inganäs, O.; Mammo, W.; Olinga, T.; Svensson, M.; Andersson, M. R. Photophysics of Substituted Polythiophenes. *J. Phys. Chem. B* **1999**, *103*, 7771–7780.

(157) Jiang, X. M.; Jiang, X. M.; Vardeny, Z. V; Vardeny, Z. V; Korovyanko, O. J.; Korovyanko, O. J.; Janssen, R. a J.; Janssen, R. a J. Photoexcitation Dynamics in Regioregular and Regiorandom Polythiophene Lms ¨. *Phys. Rev.* **2001**, *64*, 1–6.

(158) Thompson, B. C.; Fr??chet, J. M. J. Polymer-Fullerene Composite Solar Cells. *Angew. Chemie - Int. Ed.* **2008**, *47*, 58–77.

(159) Coakley, K. M.; McGehee, M. D. Conjugated Polymer Photovoltaic Cells. *Chem. Mater.* **2004**, *16*, 4533–4542.

(160) Brédas, J.-L.; Durrant, J. R. Organic Photovoltaics. *Acc. Chem. Res.* **2009**, *42*, 1689–1690.

(161) Grancini, G.; Maiuri, M.; Fazzi, D.; Petrozza, a; Egelhaaf, H.-J.; Brida, D.; Cerullo, G.; Lanzani, G. Hot Exciton Dissociation in Polymer Solar Cells. *Nat. Mater.* **2013**, *12*, 29–33.

(162) M??ller, J. G.; Lupton, J. M.; Feldmann, J.; Lemmer, U.; Scharber, M. C.; Sariciftci, N. S.; Brabec, C. J.; Scherf, U. Ultrafast Dynamics of Charge Carrier Photogeneration and Geminate Recombination in Conjugated Polymer:fullerene Solar Cells. *Phys. Rev. B - Condens. Matter Mater. Phys.* **2005**, *72*, 1–10.

(163) Lanzani, G.; Cerullo, G.; Polli, D.; Gambetta, A.; Zavelani-Rossi, M.; Gadermaier, C. Photophysics of Conjugated Polymers: The Contribution of Ultrafast Spectroscopy. *Phys. Status Solidi Appl. Res.* **2004**, *201*, 1116–1131.

(164) Gélinas, S.; Poll, T. S. Van Der; Bazan, G. C.; Friend, R. H. Ultrafast Long-Range Charge Photovoltaic Diodes. **2014**, *512*, 512–517.

(165) Musser, A. J.; Al-Hashimi, M.; Maiuri, M.; Brida, D.; Heeney, M.; Cerullo, G.; Friend, R. H.; Clark, J. Activated Singlet Exciton Fission in a Semiconducting Polymer. *J. Am. Chem. Soc.* **2013**, *135*, 12747–12754.

(166) Smith, M. B.; Michl, J. Recent Advances in Singlet Fission. *Annu. Rev. Phys. Chem.* **2013**, *64*, 361–386.

(167) Olejnik, E.; Pandit, B.; Basel, T.; Lafalce, E.; Sheng, C. X.; Zhang, C.; Jiang, X.; Vardeny, Z. V. Ultrafast Optical Studies of Ordered poly(3-Thienylene-Vinylene) Films. *Phys. Rev. B - Condens. Matter Mater. Phys.* **2012**, *85*, 2–7.

(168) Gavrilenko, a. V.; Matos, T. D.; Bonner, C. E.; Sun, S.-S.; Zhang, C.; Gavrilenko, V. I. Optical Absorption of Poly(thiophene Vinylene) Conjugated Polymers. Experiment and First Principle Theory. **2008**, 6.

(169) Smith, A. P.; Smith, R. R.; Taylor, B. E.; Durstock, M. F. An Investigation of Poly (Thienylene Vinylene) in Organic Photovoltaic Devices. *Society* **2004**, 4687–4692.

(170) Henckens, A.; Knipper, M.; Polec, I.; Manca, J.; Lutsen, L.; Vanderzande, D. Poly(thienylene Vinylene) Derivatives as Low Band Gap Polymers for Photovoltaic Applications. *Thin Solid Films* **2004**, *451-452*, 572–579.

(171) Girotto, C.; Cheyns, D.; Aernouts, T.; Banishoeib, F.; Lutsen, L.; Cleij, T. J.; Vanderzande, D.; Genoe, J.; Poortmans, J.; Heremans, P. Bulk Heterojunction Organic Solar Cells Based on Soluble Poly(thienylene Vinylene) Derivatives. *Org. Electron. physics, Mater. Appl.* **2008**, *9*, 740–746.

(172) Kim, J. Y.; Qin, Y.; Stevens, D. M.; Ugurlu, O.; Kalihari, V.; Hillmyer, M. a.; Frisbie, C. D. Low Band Gap Poly(thienylene vinylene)/Fullerene Bulk Heterojunction Photovoltaic Cells. *J. Phys. Chem. C* **2009**, *113*, 10790–10797.

(173) Spano, F. C.; Silva, C. H- and J-Aggregate Behavior in Polymeric Semiconductors. *Annu. Rev. Phys. Chem.* **2014**, *65*, 477–500.

(174) Mevellec, J. Y.; Buisson, J. P.; Lefrant, S. Studies of the Vibrational Properties of Poly- { Arylene Vinylenes). *107*, 298–303.

(175) Ozaki, M.; Ehrenfreund, E.; Benner, R.; Barton, T.; Yoshino, K.; Vardeny, Z. Dispersion of Resonant Raman Scattering in π-Conjugated Polymers: Role of the

Even Parity Excitons. *Phys. Rev. Lett.* **1997**, *79*, 1762–1765.

(176) Gao, J.; Thomas, A. K.; Johnson, R.; Guo, H.; Grey, J. K. Spatially Resolving Ordered and Disordered Conformers and Photocurrent Generation in Intercalating Conjugated Polymer / Fullerene Blend Solar Cells. *Chem. Mater.* **2014**, *26*, 4395–4404.

(177) Reber, C.; Zink, J. I. Resonance Raman Deenhancement Caused by Excited-State Potential Surface Crossing. *J. Phys. Chem.* **1992**, *96*, 571–576.

(178) Shin, K.-S. K.; Zink, J. I. Interference Effects on Resonance Raman Excitation Profiles Caused by Two Electronic Excited States. *J. Am. Chem. Soc.* **1990**, *112*, 7148–7157.

(179) Tannor, D. J. Polyatomic Raman Scattering for General Harmonic Potentials. *J. Chem. Phys.* **1982**, *77*, 202.

(180) Erlc J. Heller, Robed L. Sundberg, and D. T. Simple Aspects of Raman Scattering. *J. Phys. Chem.* **1999**, *86*, 1822–1833.

(181) Gao, J.; Grey, J. K. Resonance Raman Overtones Reveal Vibrational Displacements and Dynamics of Crystalline and Amorphous poly(3-Hexylthiophene) Chains in Fullerene Blends. *J. Chem. Phys.* **2013**, *139*.

(182) Rich, C. C.; McHale, J. L. Resonance Raman Spectra of Individual Excitonically Coupled Chromophore Aggregates. *J. Phys. Chem. C* **2013**, *117*, 10856–10865.

(183) Gao, Y.; Martin, T. P.; Niles, E. T.; Wise, A. J.; Thomas, A. K.; Grey, J. K. Understanding Morphology-Dependent Polymer Aggregation Properties and Photocurrent Generation in Polythiophene/Fullerene Solar Cells of Variable

Compositions. *J. Phys. Chem. C* **2010**, *114*, 15121–15128.

(184) Vandewal, K.; Tvingstedt, K.; Gadisa, A.; Inganäs, O.; Manca, J. V. On the Origin of the Open-Circuit Voltage of Polymer–fullerene Solar Cells. *Nat. Mater.* **2009**, *8*, 904–909.

(185) Gao, Y.; Martin, T. P.; Thomas, A. K.; Grey, J. K. Resonance Raman Spectroscopic- and Photocurrent Imaging of Polythiophene/Fullerene Solar Cells. *J. Phys. Chem. Lett.* **2010**, *1*, 178–182.

(186) Treat, N. D.; Varotto, A.; Takacs, C. J.; Batara, N.; Al-Hashimi, M.; Heeney, M. J.; Heeger, A. J.; Wudl, F.; Hawker, C. J.; Chabinyc, M. L. Polymer-Fullerene Miscibility: A Metric for Screening New Materials for High-Performance Organic Solar Cells. *J. Am. Chem. Soc.* **2012**, *134*, 15869–15879.

(187) Collins, B. A.; Gann, E.; Guignard, L.; He, X.; McNeill, C. R.; Ade, H. Molecular Miscibility of Polymer-Fullerene Blends. *J. Phys. Chem. Lett.* **2010**, *1*, 3160–3166.

(188) Miller, N. C.; Gysel, R.; Miller, C. E.; Verploegen, E.; Beiley, Z.; Heeney, M.; McCulloch, I.; Bao, Z.; Toney, M. F.; McGehee, M. D. The Phase Behavior of a Polymer-Fullerene Bulk Heterojunction System That Contains Bimolecular Crystals. *J. Polym. Sci. Part B Polym. Phys.* **2011**, *49*, 499–503.

(189) Miller, N. C.; Sweetnam, S.; Hoke, E. T.; Gysel, R.; Miller, C. E.; Bartelt, J. A.; Xie, X.; Toney, M. F.; McGehee, M. D. Molecular Packing and Solar Cell Performance in Blends of Polymers with a Bisadduct Fullerene. *Nano Lett.* **2012**, *12*, 1566–1570.

(190) Miller, N. C.; Cho, E.; Junk, M. J. N.; Gysel, R.; Risko, C.; Kim, D.; Sweetnam,

S.; Miller, C. E.; Richter, L. J.; Kline, R. J.; *et al.* Use of X-Ray Diffraction, Molecular Simulations, and Spectroscopy to Determine the Molecular Packing in a Polymer-Fullerene Bimolecular Crystal. *Adv. Mater.* **2012**, *24*, 6071–6079.

(191) Chabinyc, M. L.; Toney, M. F.; Kline, R. J.; McCulloch, I.; Heeney, M. X-Ray Scattering Study of Thin Films of poly(2,5-bis(3-Alkylthiophen-2-yl)thieno[3,2-B]thiophene). *J. Am. Chem. Soc.* **2007**, *129*, 3226–3237.

(192) Mayer, A. C.; Toney, M. F.; Scully, S. R.; Rivnay, J.; Brabec, C. J.; Scharber, M.; Koppe, M.; Heeney, M.; McCulloch, I.; McGehee, M. D. Bimolecular Crystals of Fullerenes in Conjugated Polymers and the Implications of Molecular Mixing for Solar Cells. *Adv. Funct. Mater.* **2009**, *19*, 1173–1179.

(193) Cho, E.; Risko, C.; Kim, D.; Gysel, R.; Cates Miller, N.; Breiby, D. W.; McGehee, M. D.; Toney, M. F.; Kline, R. J.; Bredas, J. L. Three-Dimensional Packing Structure and Electronic Properties of Biaxially Oriented poly(2,5-bis(3-Alkylthiophene-2-yl)thieno[3,2- B]Thiophene) Films. *J. Am. Chem. Soc.* **2012**, *134*, 6177–6190.

(194) He, X.; Collins, B. A.; Watts, B.; Ade, H.; McNeill, C. R. Studying Polymer/fullerene Intermixing and Miscibility in Laterally Patterned Films with X-Ray Spectromicroscopy. *Small* **2012**, *8*, 1920–1927.

(195) Cates, N. C.; Gysel, R.; Beiley, Z.; Miller, C. E.; Toney, M. F.; Heeney, M.; McCulloch, L.; McGehee, M. D. Tuning the Properties of Polymer Bulk Heterojunction Solar Cells by Adjusting Fullerene Size to Control Intercalation. *Nano Lett.* **2009**, *9*, 4153–4157.

(196) Parmer, J. E.; Mayer, A. C.; Hardin, B. E.; Scully, S. R.; McGehee, M. D.;

Heeney, M.; McCulloch, I. Organic Bulk Heterojunction Solar Cells Using poly(2,5-bis(3- Tetradecyllthiophen-2-yl)thieno[3,2,- B] Thiophene). *Appl. Phys. Lett.* **2008**, *92*, 2006–2009.

(197) Sun, Q.; Park, K.; Dai, L. Liquid Crystalline Polymers for Efficient Bilayer-Bulk-Heterojunction Solar Cells Liquid Crystalline Polymers for Efficient Bilayer-Bulk-Heterojunction Solar Cells. **2009**, 7892–7897.

(198) He, F.; Yu, L. How Far Can Polymer Solar Cells Go? In Need of a Synergistic Approach. *J. Phys. Chem. Lett.* **2011**, *2*, 3102–3113.

(199) Heeger, A. J. 25th Anniversary Article: Bulk Heterojunction Solar Cells: Understanding the Mechanism of Operation. *Adv. Mater.* **2014**, *26*, 10–28.

(200) Delongchamp, D. M.; Kline, R. J.; Jung, Y.; Germack, D. S.; Lin, E. K.; Moad, A. J.; Richter, L. J.; Toney, M. F.; Heeney, M.; Mcculloch, I. Controlling the Orientation of Terraced Nanoscale “ribbons” of a Poly(thiophene) Semiconductor. *ACS Nano* **2009**, *3*, 780–787.

(201) Li, J.; Sun, Z.; Yan, F. Solution Processable Low-Voltage Organic Thin Film Transistors with High-K Relaxor Ferroelectric Polymer as Gate Insulator. *Adv. Mater*. **2012**, *24*, 88–93.

(202) Poelking, C.; Andrienko, D. E Ff Ect of Polymorphism , Regioregularity and Paracrystallinity on Charge Transport in Poly (3-Hexylthiophene) [P3HT] Nano Fi Bers. *Macromolecules* **2013**.

(203) Poelking, C.; Cho, E.; Malafeev, A.; Ivanov, V.; Kremer, K.; Risko, C.; Brédas, J. L.; Andrienko, D. Characterization of Charge-Carrier Transport in Semicrystalline

Polymers: Electronic Couplings, Site Energies, and Charge-Carrier Dynamics in Poly(bithiophene-Alt-Thienothiophene) [PBTTT]. *J. Phys. Chem. C* **2013**, *117*, 1633–1640.

(204) Liu, T.; Troisi, A. Understanding the Microscopic Origin of the Very High Charge Mobility in PBTTT: Tolerance of Thermal Disorder. *Adv. Funct. Mater.* **2014**, *24*, 925–933.

(205) Hwang, I. W.; Kim, J. Y.; Cho, S.; Yuen, J.; Coates, N.; Lee, K.; Heeney, M.; McCulloch, I.; Moses, D.; Heeger, A. J. Bulk Heterojunction Materials Composed of poly(2,5-bis(3- Tetradecylthiophen-2-yl)thieno[3,2-B;]thiophene): Ultrafast Electron Transfer and Carrier Recombination. *J. Phys. Chem. C* **2008**, *112*, 7853–7857.

(206) Byers, J. C.; Ballantyne, S.; Rodionov, K.; Mann, A.; Semenikhin, O. a. Mechanism of Recombination Losses in Bulk Heterojunction P3HT:PCBM Solar Cells Studied Using Intensity Modulated Photocurrent Spectroscopy. *ACS Appl. Mater. Interfaces* **2011**, *3*, 392–401.

(207) Set, Y. T.; Heinemann, M. D.; Birgersson, E.; Luther, J. On the Origin of the Quadrant I Semicircle in Intensity-Modulated Photocurrent Spectra of P3HT:PCBM Bulk Heterojunction Solar Cells: Evidence of Degradation-Related Trap-Assisted Recombination. *J. Phys. Chem. C* **2013**, *117*, 7993–8000.

(208) Woo, C. H.; Thompson, B. C.; Kim, B. J.; Toney, M. F.; Fréchet, J. M. J. The Influence of Ppoly(3-Hexylthiophene) Regioregularity on Fullerene-Composite Solar Cell Performance. *J. Am. Chem. Soc.* **2008**, *130*, 16324–164329.

(209) Gasperini, A.; Sivula, K. E Ff Ects of Molecular Weight on Microstructure and

Carrier Transport in a Semicrystalline Poly (Thieno) Thiophene. **2013**.

(210) Lee, M. J.; Gupta, D.; Zhao, N.; Heeney, M.; Mcculloch, I.; Sirringhaus, H. Anisotropy of Charge Transport in a Uniaxially Aligned and Chain-Extended, High-Mobility, Conjugated Polymer Semiconductor. *Adv. Funct. Mater.* **2011**, *21*, 932–940.

(211) Faculty, T. A.; Cho, E.; Fulfillment, I. P.; Engineering, S. Determination Via Computational Modeling of the Structure-Properties Relationships in Interclated Polymer : Fullerene Blends Found in Bulk-Heterojunction Solar Cells Determination Via Computational Modeling of the Structure-Properties Relationships in Int. **2012**.

(212) Kaake, L. G.; Moses, D.; Heeger, A. J. Coherence and Uncertainty in Nanostructured Organic Photovoltaics. *J. Phys. Chem. Lett.* **2013**, *4*, 2264–2268.

(213) Kaake, L. G.; Jasieniak, J. J.; Bakus, R. C.; Welch, G. C.; Moses, D.; Bazan, G. C.; Heeger, A. J. Photoinduced Charge Generation in a Molecular Bulk Heterojunction Material. *J. Am. Chem. Soc.* **2012**, *134*, 19828–19838.

(214) Jamieson, F. C.; Domingo, E. B.; McCarthy-Ward, T.; Heeney, M.; Stingelin, N.; Durrant, J. R. Fullerene Crystallisation as a Key Driver of Charge Separation in Polymer/fullerene Bulk Heterojunction Solar Cells. *Chem. Sci.* **2012**, *3*, 485.

(215) Miller, N. C.; Cho, E.; Gysel, R.; Risko, C.; Coropceanu, V.; Miller, C. E.; Sweetnam, S.; Sellinger, A.; Heeney, M.; McCulloch, I.; *et al.* Factors Governing Intercalation of Fullerenes and Other Small Molecules between the Side Chains of Semiconducting Polymers Used in Solar Cells. *Adv. Energy Mater.* **2012**, *2*, 1208–1217.

(216) Milani, A.; Brambilla, L.; Del Zoppo, M.; Zerbi, G. Raman Dispersion and Intermolecular Interactions in Unsubstituted Thiophene Oligomers. *J. Phys. Chem. B* **2007**, *111*, 1271–1276.

(217) V??zquez, H.; Troisi, A. Calculation of Rates of Exciton Dissociation into Hot Charge-Transfer States in Model Organic Photovoltaic Interfaces. *Phys. Rev. B - Condens. Matter Mater. Phys.* **2013**, *88*, 1–5.

(218) Savenije, T. J.; Grzegorczyk, W. J.; Heeney, M.; Tierney, S.; McCulloch, I.; Siebbeles, L. D. A. Photoinduced Charge Carrier Generation in Blends of Poly(thienothiophene) Derivatives and [6,6]-Phenyl-c61-Butyric Acid Methyl Ester: Phase Segregation versus Intercalation. *J. Phys. Chem. C* **2010**, *114*, 15116–15120.

(219) Dante, M.; Dante, M.; Peet, J.; Peet, J.; Nguyen, T.-Q.; Nguyen, T.-Q. Nanoscale Charge Transport and Internal Structure of Bulk Heterojunction Conjugated Polymer/ Fullerene Solar Cells by Scanning Probe Microscopy. *J. Phys. Chem. C* **2008**, *112*, 7241.

(220) Coffey, D. C.; Reid, O. G.; Rodovsky, D. B.; Bartholomew, G. P.; Ginger, D. S. Mapping Local Photocurrents in Polymer/fullerene Solar Cells with Photoconductive Atomic Force Microscopy. *Nano Lett.* **2007**, *7*, 738–744.

(221) Street, R. A.; Northrup, J. E.; Krusor, B. S. Radiation Induced Recombination Centers in Organic Solar Cells. **2012**, *205211*, 1–13.

(222) Vaselabadi, S. A.; Shakarisaz, D.; Ruchhoeft, P.; Strzalka, J.; Stein, G. E. Radiation Damage in Polymer Films from Grazing-Incidence X-Ray Scattering Measurements. **2016**, 1–13.

(223) Murphy, B. F.; Osipov, T.; Jurek, Z.; Fang, L.; Son, S.-K.; Mucke, M.; Eland, J. H. D.; Zhaunerchyk, V.; Feifel, R.; Avaldi, L.; *et al.* Femtosecond X-Ray-Induced Explosion of C60 at Extreme Intensity. *Nat. Commun.* **2014**, *5*, 4281.

(224) Voroshazi, E.; Verreet, B.; Aernouts, T.; Heremans, P. Solar Energy Materials & Solar Cells Long-Term Operational Lifetime and Degradation Analysis of P3HT : PCBM Photovoltaic Cells. *Sol. Energy Mater. Sol. Cells* **2011**, *95*, 1303–1307.

(225) Finck, B. Y.; Schwartz, B. J. Understanding the Origin of the S-Curve in Conjugated Polymer/fullerene Photovoltaics from Drift-Diffusion Simulations. *Appl. Phys. Lett.* **2013**, *103*.

(226) Photocells, O.; Kambour, K.; Rosen, N.; Kouhestani, C.; Nguyen, D.; Mayberry, C.; Devine, R. A. B.; Kumar, A.; Chen, C.; Li, G.; *et al.* Modeling of the X-Irradiation Response of the Carrier Relaxation Time in P3HT : PCBM. **2012**, *59*, 2902–2908.

(227) Kouhestani, C.; Nguyen, D. D.; Kambour, K. E.; Devine, R. A. B.; Chen, J.; Li, G.; Kouhestani, C. Transient Measurements of Carrier Relaxation Time and Density in the P3HT : PCBM Organic Photovoltaic Cell Transient Measurements of Carrier Relaxation Time and Density in the P3HT : PCBM Organic Photovoltaic Cell. **2015**, *032404*.

(228) Tress, W. Organic Solar Cells - Theory, Experiment, and Device Simulation. *Springer* **2014**, *208.*

(229) Photovoltaics, Q.; Ayzner, A. L.; Doan, S. C.; Villers, B. T. De; Schwartz, B. J. Ultrafast Studies of Exciton Migration and Polaron Formation in Sequentially Solution-Processed Conjugated Polymer/Fullerene Quasi-Bilayer Photovoltaics.

2012.

(230) Kouhestani, C.; Nguyen, D. D.; Kambour, K. E.; Devine, R. A. B.; Chen, J.; Li, G.; Kouhestani, C. Ionizing Radiation Induced Parametric Variations in P3HT : PCBM Organic Photovoltaic Cells Ionizing Radiation Induced Parametric Variations in P3HT : PCBM Organic Photovoltaic Cells. **2015**, *032403*.

(231) Chambon, S.; Rivaton, A.; Gardette, J. L.; Firon, M. Photo- and Thermal Degradation of MDMO-PPV:PCBM Blends. *Sol. Energy Mater. Sol. Cells* **2007**, *91*, 394–398.

(232) Manceau, M.; Chambon, S.; Rivaton, A.; Gardette, J. L.; Guillerez, S.; Lematre, N. Effects of Long-Term UVvisible Light Irradiation in the Absence of Oxygen on P3HT and P3HT: PCBM Blend. *Sol. Energy Mater. Sol. Cells* **2010**, *94*, 1572–1577.

(233) Reese, B. M. O.; Nardes, A. M.; Rupert, B. L.; Larsen, R. E.; Olson, D. C.; Lloyd, M. T.; Shaheen, S. E.; Ginley, D. S.; Rumbles, G.; Kopidakis, N. Photoinduced Degradation of Polymer and Polymer – Fullerene Active Layers : Experiment and Theory. **2010**, 3476–3483.

(234) Miller, A. A. EFFECTS OF HIGH-ENERGY RADIATION ON POLYMERS A. A. Miller. 774–781.

(235) Laghari, J. R.; Hammoud, A. N. A BRIEF SURVEY OF RADIATION EFFECTS ON POLYMER DIELECTRICS. *Ieee Trans. Nucl. Sci.* **1990**, *37*, 1076–1083.